University of Southern California

Data Based Modeling and Analysis in Reservoir Waterflooding

by

Amin Rezapour

A Dissertation Presented to the
FACULTY OF THE USC GRADUATE SCHOOL
UNIVERSITY OF SOUTHERN CALIFORNIA
In Partial Fulfillment of the
Requirements for the Degree
DOCTOR OF PHILOSOPHY

Signal and Image Processing Institute
Ming Hsieh Department of Electrical Engineering

January 2016

ABSTRACT

This thesis focuses on the applications of *Filtering & System Identification* in *Reservoir Waterflood Simulation* in two major sections; 1) Investigating the challenges in identification of data-based, low order, linear, and time invariant models that are used for describing injector(s)-producer(s) relationship, and 2) Upscaling irregular reservoir grids that are used for waterflood simulation using graph signal processing.

Data based modeling techniques have been used in reservoir simulation in the past decade. However, most of the attention has been on the mathematical development of the model structures, and less on the information content of the training data. This thesis shows that the reliability of the models in terms of predicting the production rates can be improved if the training data is obtained with predefined injection sequence(s) and under known reservoir condition. Injection rate signals that have more variations can provide more information about the underlying dynamics of the system, but determining these variations is not trivial since large variations can cause severe nonlinearities in the waterflood process. A methodology is proposed on how to design the characteristics of an appropriate injection sequence such as length and amplitude of variations and its frequency, and how to translate the information about the reservoir into those design parameters.

Numerous reservoir upscaling methods have been proposed in the literature, including the applications of the wavelet transform in recent studies. However, the applications are limited to the models that are represented by regular computational grids with equal size blocks or cells. We propose a generalization of the lifting scheme for upscaling by representing the reservoir grid on a graph network that makes it possible to use wavelet transform and spatial and spectral analysis to upscale any irregular grid highly efficiently. A graph bipartition algorithm and a method to calculate the equivalent permeability of the enlarged cells are introduced, along with a complete simulation example.

ACKNOWLEDGMENTS

I would like to thank my supervisor Prof. Ortega for his mentorship. He has been the constant element of my academic life during the past five years, and helped me stay focused and productive during my down times. Unlike me being naive from time to time in our meetings, he has always been patient, positive and motivating.

This project would have never been shaped without the best professor I have ever had; Prof. Ershaghi. He has been the one and only source of vision, motivation and encouragement even before I start my PhD. I thank him for always believing in me. I would also like to Prof. Sahimi for bringing his genius idea and exemplary vision of using wavelet transform for upscaling unstructured grid, who has inspired me with his noble character, academic achievements and his compassion and contributions to his home country.

I am very humble and grateful for my friends and colleagues both in Electrical Engineering and Petroleum Engineering departments. My friend and brother Arash Vafanejad, my friend and colleague Mohammad Korjani, my office mate Hilmi Eğilmez, and friends who helped me learn reservoir simulation using commercial simulator like a pro, Tayeb A. Tafti, Hassan Shojaei, Hassan Dashtian, Mohammad Javaheri and Qianru Qi. A special thanks to Mohammad Karimi-Fard and Prof. Durlofsky and his team at Stanford University for providing me with the opportunity to learn and use reservoir simulator GPRS.

In the end I must thank Prof. Leahy, who humbled me by accepting to be in the committee. Special gratitude to all the people at SIPI and CiSoft, particularly Juli Legat and Mike Hauser. And the whole Trojan Family at University of Southern California for letting me being a part of this tremendous academic environment, college spirit and the great city of Los Angeles.

Last but not least, I'd like to thank my family for their love, caring and financial support.

This thesis is written in LaTeX in a modified template by Steve R. Gunn and Sunil Patel.

Contents

Abstract ii

Acknowledgments iii

Contents v

List of Figures ix

List of Tables xiii

1 Introduction 1
- 1.1 Waterflood Modeling . . . 2
  - 1.1.1 Data Based Modeling . . . 3
  - 1.1.2 Reservoir Upscaling . . . 4
- 1.2 Problem Definition and Proposed Approach . . . 4
- 1.3 Thesis Outline . . . 5

2 Flow Modeling in Porous Media 7
- 2.1 Dynamics and Modeling of Two Phase Flow . . . 7
  - 2.1.1 Simplification For 1D Flow . . . 9
- 2.2 Sources of Nonlinearity . . . 10
- 2.3 Data-Based Modeling of Two Phase Flow . . . 11
  - 2.3.1 Linear Model Structure . . . 12
  - 2.3.2 Capacitance Model . . . 13
  - 2.3.3 FIR Model . . . 13
  - 2.3.4 ARX Model . . . 14
  - 2.3.5 State Space Model . . . 15
- 2.4 Conclusion . . . 16

3 Data Based Modeling of Reservoir Waterflood 19
- 3.1 System Identification: Brief Review . . . 20
  - 3.1.1 Prediction Error Identification (PEI) . . . 20
  - 3.1.2 Subspace Identification (SubID) . . . 21
  - 3.1.3 Conditions on the Training Data . . . 23
- 3.2 Reservoir Model Identification: Simple Example . . . 25
  - 3.2.1 Reservoir Description . . . 25
    - 3.2.1.1 Rock and Fluid Properties . . . 25
    - 3.2.1.2 Well Setting . . . 27

3.2.1.3 Free Run . . . 28
3.2.2 Model Identification . . . 30
3.2.3 Model Analysis and Discussion . . . 35
3.3 Conclusion . . . 37

4 Injection Scheduling Design: Methodology and A Full Simulation Example 41
4.1 Experiment Design . . . 42
4.1.1 Sampling Time . . . 43
4.1.2 Signal Power and Frequency of Variations . . . 43
4.1.3 Experiment Length . . . 44
4.1.4 Amplitude of Variations . . . 45
4.1.5 Signal Type . . . 46
4.1.6 Methodology . . . 47
4.2 Multi Fracture Tight Reservoir Model . . . 47
4.2.1 Well Settings . . . 49
4.3 Preparatory Experiments . . . 50
4.3.1 Transient Test Response . . . 51
4.3.2 Staircase Input Signal . . . 54
4.3.3 Prior Knowledge . . . 55
4.4 Injection Scheduling . . . 56
4.4.1 Uncorrelatedness of Injection Sequence in Multi-Injector . . . 56
4.5 Model Identification and Validation . . . 58
4.6 Conclusion . . . 58

5 Reservoir Model Upscaling Using Graph Wavelet 61
5.1 Reservoir Upscaling Techniques . . . 62
5.2 Gridding Schemes: Regular vs. Unstructured . . . 63
5.3 Upscaling Using Wavelet Transform . . . 64
5.4 Graph Representation of Reservoir . . . 65
5.4.1 Reservoir Graph Spectral Analysis . . . 66
5.5 Graph Signal Analysis . . . 67
5.5.1 Graph Signal Filtering . . . 68
5.6 Lifting Based Wavelet Transform . . . 70
5.6.1 Lifting Scheme . . . 71
5.6.2 Lifting on Graph . . . 72
5.7 Reservoir Upscaling Algorithm for Irregular Grid . . . 73
5.7.1 Bipartition Algorithm . . . 74
5.7.2 Calculating the Equivalent Permeability . . . 75
5.8 Experimental Results . . . 76
5.9 Conclusion . . . 81

6 Conclusion and Future Work 83

A Relative Permeability 87

B Discretization in Time and Space for Fluid Simulation in Porous Media 91

B.1 Spatial Discretization 91
B.2 Time Discretization 92
B.3 Simulation 93

C Capacitance Model for Waterflooding **95**

Symbols **97**

Bibliography **99**

List of Figures

1.1 Process of waterflooding using a horizontal injection and production well, equipped with Internal Control Valve (ICV). The irregular-shaped oil-water front is a result of the reservoir heterogeneities. Image courtesy of [1] . . . 1
1.2 An example of a discretized reservoir model with heterogeneous permeability distribution, with large number of vertical wells. Image courtesy of [1]. . . . 2

3.1 Oil saturation (S_o) 3D view of the homogeneous reservoir HR11 before water break through. Blue areas have more water and red areas more oil. This reservoir has one injector and one producer on the opposite corners. 26
3.2 Oil Compressibility c_o vs. Pressure for HR11. . . . 27
3.3 Oil and Water Relative Permeability vs. Saturation for HR11. . . . 27
3.4 Oil, water and liquid rate (left axis) and gas rate (right axis) of the producer, and water rate of the injector for the lifecycle of HR11. Constant injection rate is applied from the beginning. . . . 28
3.5 Well pressure, well gridblock pressure and average reservoir pressure for the lifecycle of HR11. Constant injection rate is applied from the beginning. 28
3.6 Water saturation S_w for injector (blue) and producer (red) for the lifecycle of HR11. Constant injection rate is applied from the beginning. . . . 29
3.7 Examples of input sequences used for training.TR1 is constant, TR13 with medium variation ±25% of nominal value, TR26 with fast variations ±50% of nominal value. . . . 30
3.8 Examples of frequency content of input sequences used for training. The number of variations increases with the index of the input signal. . . . 31
3.9 Examples of output data for training, before, during and after the water break through. . . . 32
3.10 The lifecycle of the HR11 after applying injection scheduling TR13 for training. . . . 33
3.11 Gridblock pressure changes due to the applied input signals. Producer block (bottom blue), center block (middle green) and injector block (top blue). . . . 33
3.12 Examples of gridblock water saturation S_w changes due to the applied input signals. The gridblock at the center (green) and the producer gridblock (blue). . . . 34
3.13 Examples of cumulative produced oil for the lifecycle of HR11 for different input signals. . . . 35
3.14 Training and validation fit for the identified models of Capacitance Model. 36

3.15 Training and validation fit for the identified models of Distributed Capacitance Model. . . . 37
3.16 Training and validation fit for the identified models of 2nd Order ARX Model. . . . 38
3.17 Training and validation fit for the identified models of 14th Order FIR Model. . . . 39
3.18 Training and validation fit for the identified models of 2nd Order State Space Model. . . . 40

4.1 System identification procedure and experiment design. . . . 42
4.2 Permeability map of the reservoir model FR34. Permeability is the same for i, j and k direction. . . . 49
4.3 Daily liquid rate of each producer for model FR34, during the first year of reservoir lifecycle. . . . 50
4.4 Oil saturation of the RF34 at the end of its lifecycle. . . . 51
4.5 Water saturation S_w of the producers in FR34 during its lifecycle. . . . 51
4.6 Step like increase in the injection rate INJ1 from 100 bbl/day to 500 bbl/day and produced liquid rate response on all producers. . . . 52
4.7 Step like increase in the injection rate INJ2 from 100 bbl/day to 500 bbl/day and produced liquid rate response on all producers. . . . 52
4.8 Step like increase in the injection rate INJ3 from 100 bbl/day to 500 bbl/day and produced liquid rate response on all producers. . . . 53
4.9 Frequency response (Bode plot) of a system with a single pole at 3 days settling time. . . . 54
4.10 Response of PRO1 to staircase increase of injection rate in INJ2, 100 bbl/day increase. . . . 55
4.11 Response of PRO4 to staircase increase of injection rate in INJ3, 100 bbl/day increase. . . . 55
4.12 Designed injection rate schedule for training in reservoir model FR34. . . . 57
4.13 Frequency content of the designed input signals after filtering according to adjusted system pole location. The plot is drawn for three signals of the same characteristics with 50 times longer length to show the asymptotic behavior of the PRBS. . . . 57
4.14 Cross correlation between the three injection schedule for ±5 days lag. . . . 58
4.15 Training simulation fit for producers of the reservoir model FR34, identified with a CM. . . . 59
4.16 Validation simulation fit for producers of the reservoir model FR34, identified with a CM. . . . 60

5.1 Geometrical representation of two adjacent control volume represented by two arbitrary gridblocks. This figure shows the parameters for calculating transmissibility T. . . . 66
5.2 Filtering of permeability graph signal $\mathbf{K}$ based on transimissibility graph G_T of a fractured reservoir model. Filtering operation is given by Equation (5.8), for $N = 1600$. . . . 69
5.3 Low pass filtering in vertex domain using 3-hop neighbor averaging for permeability graph signal of a fractured reservoir model, and the filter is given by Equation (5.9). . . . 70

5.4 Filtering of permeability graph signal **K** based on transimissibility graph G_T of the fractured reservoir model with $N = 1600$ nodes, in spectral domain with a low pass filter given by Equation (5.10). 70
5.5 Block diagram of lifting scheme. 72
5.6 The areas of the cells or grid blocks increase during upscaling, and consist of the area of the cell from the initial graph (or the graph in the last coarsening level) and partial areas from the neighboring cells. Here we show an example of a cell v_0 with area A_0 that has been increased into $A_0 + A_1 + A_2 + A_3$ as a resulting of coarsening and merging of some of the cells. 76
5.7 Snapshots of grid coarsening using graph wavelet transform. 78
5.8 Reducing the number of cells by iterating the upscaling algorithm for two thresholds ϵ_D. 78
5.9 Percentage errors in predicting the water breakthrough time (WBT) by the upscaled models for two thresholds. 79
5.10 Percentage errors in predicting the total produced oil by the upscaled models for two thresholds. 80
5.11 Comparison of the average reservoir pressure in the upscaled model with their corresponding values in the geological model (GM) of the reservoir. 80
5.12 Simulation times (in CPU seconds) of the upscaled models with various iterations (levels) of coarsening. 81

A.1 Relative permeabilities to oil and water during imbibition (i.e. increasing water saturation) 88

List of Tables

3.1 Rock and Fluid Properties of Reservoir Model HR11. 26

4.1 Summary of the design parameters and how to choose them for *Injection Scheduling* in a mature waterflood reservoir. 48
4.2 Rock and Fluid Properties of Reservoir FR34. 49
4.3 Settling time of the step responses from injectors to producers. 53

5.1 Rock and Fluid Properties of Reservoir Model SPE10. 77

Chapter 1

Introduction

The production life cycle of a reservoir is in the order of decades and is commonly divided into three stages; A) The primary stage, in which the reservoir has a naturally high pressure that is enough to push almost 10% of the oil to the surface; B) Secondary stage, where reservoir pressure is regenerated by injecting water or steam (Figure 1.1), depending on the configuration and the number of injectors and producers, and on reservoir type, around 20 – 40% of the oil can be recovered by *waterflooding*; and C) The final or tertiary stage, where techniques that alter the original properties of the oil are used, e.g. improving oil mobility by injecting CO_2 or fire, or by using chemicals. In overall, enhanced oil recovery (EOR) can help extracting up to 60% of the oil in place. Oil production during this life cycle can be improved not only by using modern equipment, but also by production optimization algorithms that are based on mathematical models.

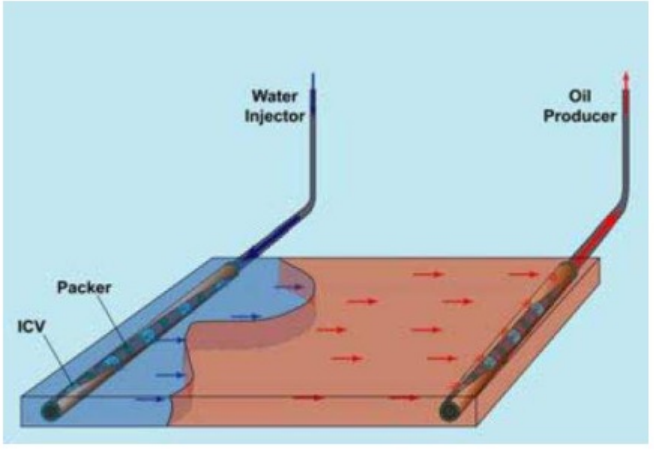

FIGURE 1.1: Process of waterflooding using a horizontal injection and production well, equipped with Internal Control Valve (ICV). The irregular-shaped oil-water front is a result of the reservoir heterogeneities. Image courtesy of [1]

.

1.1 Waterflood Modeling

The dynamics of the fluid flow in a reservoir and in wells can be modeled according to conservation of mass and momentum. The relationship between rock pressure and saturation is based on a set of coupled Partial Differential Equations (PDEs) that are nonlinear and contain high order derivatives. Alternatively, waterflooding can be modeled using empirical relations, such as Darcy's law, which are simpler and have been developed based on lab experiments. It should be noted that in either approach, the models and system boundaries of the wells and facilities can generally be defined reasonably accurate, but reservoir properties are highly heterogeneous and known with large uncertainties. Accordingly, subsurface model parameters are not stationary and accurate and usually multiple models are used to simulate the fluid flow for different geological realizations [2].

PDEs are solved numerically by discretizing the field into small gridblocks. The size of the gridblocks (or equivalently their number) is determined based on the level of heterogeneity, desired solution accuracy and available computational capabilities. An example of a reservoir model with multiple injectors and producers is shown in Figure 1.2. Note that each block has a number of static properties such as permeability, porosity, etc., a number of dynamic properties such as relative permeability, compressability, etc., and two state variables: pressure and saturation. The order of the discretized reservoir model is as large as the number of states. For example for an oil field in order of miles and for gridblocks in order of feet, the model order can rise to tens of millions.

A "large scale" and "nonlinear" model with parameters that are known with uncertainty is not practical for small simulations and analysis. Moreover, there are a number of optimization and control techniques that are only applicable for linear models, see

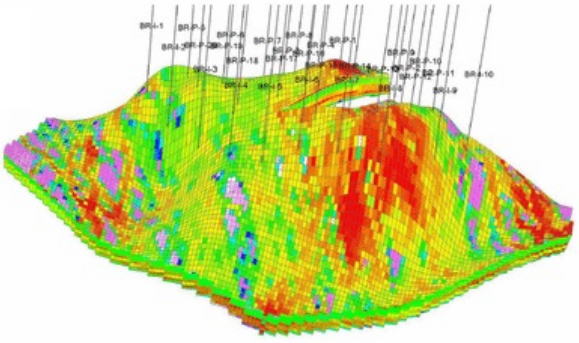

FIGURE 1.2: An example of a discretized reservoir model with heterogeneous permeability distribution, with large number of vertical wells. Image courtesy of [1].

e.g. [3–7]. To overcome this, a number of alternatives have been proposed in reservoir engineering literature such as: upscaling the model by increasing the size of the gridblock [8], smart gridding or dynamic gridding to have flexible grid size and shape [9, 10], model reduction and linearization around a working point [11], and modeling with simplified dynamics and based on empirical relationship such as the capacitance model (CM) [12]. Other types of modeling have also been introduced recently in literature to describe the interwell connectivity such as: Kalman filtering[13, 14], Subspace Identification (SubID) [15], and Prediction Error Identification (PEI) [16].

In this thesis we focus on two main aspects of reservoir waterflood modeling, one is the importance of information content of the data when used for data based modeling, and the other is using graph signal processing tools to upscale a large scale model that is discretized by arbitrary shaped cells.

1.1.1 Data Based Modeling

Approximation of injector-producer dynamical relationships with linear low order models has received a great deal of attention in recent years, because of its simplicity, ease of use and speed of estimation/update of states and parameters. By considering the waterflooding as a process, injection rates as the input signal and production rates as the output signal, a model with a simple and linear structure can be identified that can best describe the input-output relationship. All of the existing techniques are data driven and use measured injection and production rates to directly estimate the parameters of the low order model. Such a model usually lies in a much lower dimension subspace, with fewer states and parameters, as compared to a grid-based simulation model.

The effectiveness of data based modeling methods is indeed limited to the circumstances under which the model parameters are estimated or *trained*, and what is expected from them. For example, we will show in Chapter 2 that nonlinearities are more pronounced and parameters are varying more rapidly during the water break through (WBT)[1], where linear low order models would highly suffer from undermodeling.

Despite such limitations, these models can be reasonably accurate in terms of predictability by making sure that the training data is obtained in controlled and predefined conditions such that all the relevant dynamics are excited. The experiment design for obtaining an informative training data is the subject of Chapters 3 and 4.

[1]Water breakthrough is referred to the phase when water reaches the producers while most of the produced fluid is oil. It will be explained why low saturation of water causes nonlinearity.

1.1.2 Reservoir Upscaling

Reservoir upscaling can be done for either static properties such as absolute permeability, porosity, or dynamic properties like relative permeability and capillary curves. The correctness criterion of an upscaling procedure is often the equality of flow for a given flow potential [17, 18]. Accordingly, the coarse model should be capable of reproducing the main aspects of the fine-scale flow behavior such as flow rates, average pressures, average saturations, and breakthrough times. However, all coarsening procedures introduce a discrepancy and loss of detail in the numerical model. Study of upscaling techniques is not new, but it is still an ongoing research area of significant importance, leading to simulation errors when not done properly [19]. In most practical upscaling approaches, the resulting coarse-scale equations from homogenization and averaging have the same form as the fine-scale equations with the difference that the fine-scale parameters are replaced by upscaled (effective) ones [20, 21]. Different methods of two-phase flow upscaling can be found in [22–25]. Other methods such as multi-scale methods, dual-gridding techniques, upscaling with flow-based gridding and near-well upscaling are also examples of upscaling techniques. The reader is referred to [26] for a review.

Applications of Signal Processing and specifically Wavelet Transform (WT) for upscaling have received attention recently and [27] presented an accurate approach to reduce the number of cells in a structured grid. In their approach, the detail and scale coefficients of WT of permeability distribution are calculated for x and y direction. However, the concept of direction becomes very complex for unstructured/non-uniform grids, which are very useful and efficient for modeling the fractures and flow in fractured media. Therefore, using classical signal processing rules out the application of wavelets in unstructured gridding, such as triangular grids and Voronoi tesselations.

1.2 Problem Definition and Proposed Approach

Injection Scheduling for Improved Model Reliability: The usefulness of the training data has been extensively studied in the system identification literature and is usually referred to as *experiment design* or *input design*. The very basic goal of experiment design is to develop an automated procedure for obtaining appropriate training data, where the challenges are to provide tests that are cost-efficient (preferably short with little disturbance in process operation), that keep the operation within constraints, and that sufficiently excite the process dynamics that are relevant for subsequent design of model-based multivariable controllers.

Despite its importance, experiment design has not received enough attention for waterflood modeling, and it is often assumed that the naturally existing rate fluctuations in the measurements is enough. For example [28] used a set of randomly varying pressure in injector and producer for training low order models without motivating the properties of the variations. In this study, we are proposing a methodology that basically translates the knowledge that we have from the reservoir dynamics into required statistical characteristics of the input signal, and we call it *injection scheduling*.

The proposed injection scheduling methodology is an iterative process that is proposed to first know the reservoir conditions and then design a set of varying injection rates in order to obtain sufficiently informative data for training simple LTI models. We show that this is not trivial as mild and insufficient variations result in unreliable models, and large and unbounded variations cause major nonlinear behavior in the underlying dynamics. The process is carefully designed based on both theory and experiment.

Upscaling of Unstructured Reservoir Simulation Grid: In order to successfully apply signal processing tools such as Wavelet Transform for upscaling unstructured grids, we are proposing the applications of graph signal processing. Graphs are an abstract representation of data, e.g., in social media, sensor network, internet users, economic and molecular network, where the nodes are organized arbitrarily without any order. A massive interest in analyzing and processing of such networks has brought attention to the emerging field of graph signal processing [29, 30].

The freedom of abstract data representation comes with the cost of storage and computation. Data on a graph can be visualized as a finite collection of samples, with one sample at each vertex in the graph [29], which are referred to as"graph signal" collectively. While a vector of length N is required to store the graph signal, each interpretation of the graph network, or as we call it "graph feature", requires a matrix of $N \times N$ that requires matrix operation of order N^2.

We show how a reservoir grid can be represented on a graph regardless of the shape of the cells. Using graph signal processing tools, we utilize lifting scheme to analyze local heterogeneities in the model. A graph bipartition algorithm is proposed and together with our state of the art algorithm for calculating the equivalent permeability, we introduce an upscaling scheme.

1.3 Thesis Outline

We will start this thesis by briefly reviewing the waterflood modeling in porous media in Chapter 2. By investigating the laws of conservation of mass and momentum, we can

see where and when in the reservoir the pressure and saturation dynamics are linear. Knowing the corresponding limitations, a number of linear time invariant (LTI) model structures that are well accepted in the literature are reviewed. For each structure, we have provided physical intuition and, wherever possible the interpretation of their parameters.

The remainder of the thesis is divided into two parts: I) Experiment design for linear low order waterflood modeling (Chapters 3 and 4), II) Reservoir upscaling using graph wavelet transform (Chapter 5).

Knowing that parameter estimation of LTI models greatly depends on the training dataset, in Chapter 3 we investigate the effects of various injection sequences with different statistical properties on modeling of a simple reservoir. We will show that the reliability of the models in terms of predicting the interwell connectivity greatly depends on amount of fluctuations present in the injection rates.

In Chapter 4 we propose a methodology on how to determine an appropriate input signal that has enough variations to excite the relevant dynamics, while avoiding non-linear behavior. Injection scheduling is defined as adding a number of variations on top of the injection rates, which are determined based on prior knowledge of the reservoir or by running preparatory tests.

In Chapter 5, reservoir upscaling techniques are briefly reviewed. We will show how one can represent a reservoir grid by a graph regardless of the shape and structure of the cells. Unlike classic signal processing, operations such as filtering, shifting, modulation or downsampling are not simple to interpret in graph signal processing. Therefore, graph spectral analysis and graph signal filtering concept for the proposed graph are studied. And finally, reservoir upscaling using graph wavelet transform is introduced based on multiresolution analysis of permeability distribution of a reservoir model with unstructured gridblocks. We will discuss the applications of Lifting Based Wavelet Transform on reservoir graph and propose a downsampling algorithm for upscaling.

Chapter 2

Flow Modeling in Porous Media

In this chapter we briefly review the modeling of water and oil flow in the reservoir. It was mentioned in Chapter 1 that there are basically two approaches towards modeling: The first approach is based on physical principles and dynamical relationship of pressure and saturation. By reviewing this, we want to show the nonlinear nature of the underlying dynamics, and the main sources of nonlinearity when they are approximated by linear regime. The second approach is based on the data and can either involve some physical intuition to construct a model structure or none at all. In this approach model parameters are obtained, or in other words identified, based on the data that is gathered during production.

In a typical waterflooding process, oil, water, gas and other forms of chemical components are present that make the analysis more complicated. However, in order to better understand the underlying dynamics and phase interactions, we only review the modeling of two phase flow using physical principles. Moreover, from the available different data based modeling techniques in the literature, we only briefly review the ones that are further investigated in Chapter 3. This brief review shows the limitations of linear system identification methods, and in the end we conclude a set of assumptions that must be considered for a valid data based model identification.

The reader is referred to Appendices A and B for further details of dynamics and simulation of fluid flow in porous media.

2.1 Dynamics and Modeling of Two Phase Flow

The governing dynamical equation for iso-thermal two phase flow consists of two sets of mass and momentum conservation equations for water and oil phase. Since the

flow velocity in the reservoir is slow, the momentum balance is usually replaced by an empirical relationship between flow and pressure called Darcy's law. The reader is referred to [31] for more detail on the multi-phase flow dynamics.

The mass balance equations for a 2D reservoir can be expressed as:

$$\nabla(h\rho_w\vec{v}_w) + h\frac{\partial(\rho_w\phi S_w)}{\partial t} - h\rho_w q_w = 0, \tag{2.1}$$

$$\nabla(h\rho_o\vec{v}_o) + h\frac{\partial(\rho_o\phi S_o)}{\partial t} - h\rho_o q_o = 0, \tag{2.2}$$

where indices w and o represent water and oil phase, ρ is density, $\vec{v}$ is velocity, h is reservoir height which is a function of location (x, y), ϕ is porosity, S is saturation and q represents the source (or sink) term expressed as flow rate per unit volume. Also, the Darcy's law can be represented as

$$\vec{v}_w = -\frac{k_{rw}}{\mu_w}\vec{\mathbf{K}}(\nabla p_w - \rho_w g\nabla z), \tag{2.3}$$

$$\vec{v}_o = -\frac{k_{ro}}{\mu_o}\vec{\mathbf{K}}(\nabla p_o - \rho_o g\nabla z), \tag{2.4}$$

where k_{rw} and k_{ro} are relative permeabilities, μ is viscosity, $\vec{\mathbf{K}}$ is the permeability tensor, p is pressure, g is gravity acceleration and z is the depth of the reservoir (assumed to be constant in 2D).

The above four equations have four states; S_w and S_o where $S_w + S_o = 1$, and p_w and p_o are water and oil pressure that are related by $p_o - p_w = p_c(S_w)$, where p_c is called capillary pressure and is a function of saturation. The presence of oil-water capillary pressure implies that the states are not independent of each other. [32] shows that although p_c is the key factor in hydrocarbon movement in the pores, its effect is negligible compared to dispersive effect of geological heterogeneities. In other words, oil and water pressure can be assumed to be equal if the heterogeneities are large and significant.

Moreover, the parameters $\rho_{o,w}$, ϕ, $\mu_{o,w}$ and $\vec{\mathbf{K}}$ are also function of the states which only makes the dynamical interpretation more complicated.

Meanwhile, given the iso-thermal condition, oil and water compressibility $c_{o,w}$ can be defined as:

$$c_o \triangleq \frac{1}{\rho_o}\frac{\partial\rho_o}{\partial p}, \quad c_w \triangleq \frac{1}{\rho_w}\frac{\partial\rho_w}{\partial p}, \tag{2.5}$$

while rock compressibility c_r can essentially be defined as:

$$c_r \triangleq \frac{1}{\phi}\frac{\partial \phi}{\partial p}. \tag{2.6}$$

2.1.1 Simplification For 1D Flow

In order to better understand the dynamical interactions of the states and the parameters, one can simplify Equations (2.3) and (2.4) for 1D flow, and also neglecting the dependency of μ and $\vec{\mathbf{K}}$ to pressure. Oil and water mobility λ can be defined as:

$$\lambda_o \triangleq \frac{k k_{ro}(S_o)}{\mu_o}, \quad \lambda_w \triangleq \frac{k k_{rw}(S_w)}{\mu_w}, \tag{2.7}$$

noting that the permeability tensor $\vec{\mathbf{K}}$ is now reduced to a scalar k. Combining the 1D simplified Darcy's relation A.3 and mass balance Equations (2.1) and (2.2) yields to two coupled PDE with only two states p and S_w, as follows [1]

$$-\frac{\partial}{\partial x}(\lambda_w \frac{\partial p}{\partial x}) + \phi[S_w(c_w + c_r)\frac{\partial p}{\partial t} + \frac{\partial S_w}{\partial t}] = 0, \tag{2.8}$$

$$-\frac{\partial}{\partial x}(\lambda_o \frac{\partial p}{\partial x}) + \phi[(1 - S_w)(c_o + c_r)\frac{\partial p}{\partial t} - \frac{\partial S_w}{\partial t}] = 0. \tag{2.9}$$

Moreover, we should mention that the above equations are obtained by neglecting the capillary and gravity forces, and assuming that ρ (and consequently $c_{o,w,r}$) is constant and is pressure independent, i.e., low compressibility assumption.

Equations (2.8) and (2.9) can be decoupled by summation, to get a single PDE with only pressure p as in:

$$-\frac{\partial}{\partial x}\lambda_t \frac{\partial p}{\partial x} + \phi c_t \frac{\partial p}{\partial t} = 0, \tag{2.10}$$

where $\lambda_t = \lambda_w + \lambda_o$ and $c_t = S_w c_w + (1 - S_w)c_o + c_r$ are total mobility and total compressibility, respectively. One can see that the parameters of Equation (2.10) are both function of S_w. This equation is a parabolic equation with non-constant coefficient [32] and can be further reduced to an elliptic equation with the assumption of incompressible flow leading to:

$$\frac{\partial}{\partial x}\lambda_t \frac{\partial p}{\partial x} = 0. \tag{2.11}$$

[1] Note that the source term has been dropped considering only the flow between an injector and a producer well, in which the flow in each cell is driven through boundary condition.

Intuitively, the incompressible flow assumption means that pressure changes are instantaneous. This can also be confirmed by noting that the term $\frac{\partial p}{\partial t}$ has been dropped in the above equation.

We are interested in deriving a similar equation with S_w as the primary variable. Neglecting the gravity forces, the Darcy's law that was presented in Equations (2.3) and (2.4) can be rewritten for 1D flow as follows:

$$v_w = -\lambda_w \frac{\partial p}{\partial x}, \tag{2.12}$$

$$v_o = -\lambda_o \frac{\partial p}{\partial x}. \tag{2.13}$$

Fractional flow $f_{o,w}$ is defined as $f_w \triangleq \frac{v_w}{v_w+v_o} \equiv \frac{\lambda_w}{\lambda_w+\lambda_o}$, where $v_t = v_w + v_o$ is total velocity. Note that f_w is a function of S_w and is independent of pressure gradient. Replacing f_w in Equations (2.12) and (2.13) and then into Equations (2.8) and (2.9), and dropping the compressibility dependent terms, results in:

$$v_t \frac{\partial f_w}{\partial S_w} \frac{\partial S_w}{\partial x} + \phi \frac{S_w}{\partial t} = 0. \tag{2.14}$$

The above equation is first order nonlinear hyperbolic equation. Given the incompressible flow assumption (among many others that mentioned before), the only non-constant parameter of Equation (2.14) is v_t. In fact v_t depends on pressure gradient $\frac{\partial p}{\partial x}$ according to Equations (2.12) and (2.13).

The derivation of the above equations is mainly taken from [32], based on in-situ reservoir volume, condition at the bottom of the wells and inside the reservoir. They have shown that in practice however, it is important to take into account the oil and water formation volume factor $B_{o,w}$, because of the dissolved gas in the oil and water. In fact oil and water compressibility should be defined as a function of $\frac{\partial B}{\partial p}$ rather than $\frac{\partial \rho_{o,w}}{\partial p}$. That is why in other similar model derivation $c_{o,w}$ is replaced by $B_{o,w}$.

2.2 Sources of Nonlinearity

Analyzing the quality of the identified linear models, one must take into account the conditions under which the training data is obtained. It is important to know the cause and effect of different aspects that drift the underlying dynamics from linear regime. Knowing the physics behind the sources of nonlinearity leads to proper design of injection rate variations.

In derivation of the above relations, we have shown that the parameters of the coupled PDE's are dependent on the states. In fact some of the major sources of nonlinearity are through mobility $\lambda_{o,w}$ in Equation (2.7), and in the saturation dependency of relative permeability $k_{rw}(S_w)$ and $k_{ro}(S_w)$. Relative permeability is defined as a reduction in absolute permeability $\vec{\mathbf{K}}$ due to the presence of the other phase, which gives rise to capillary pressure. In fact the nonlinearity is not negligible as long as water-oil ratio is significant [2].

Moreover, parameters of mobility are also a function of p because of the upstream weighting of the relative permeability. That is, if the pressure in two adjacent grid blocks changes slightly, but such that the flow through the grid block boundary changes direction, the upstream relative permeability changes strongly[3] [32].

Another source of nonlinearity is due to the source term in Equations (2.1) and (2.2). While it is possible to prescribe the water injection rate in the injector well directly, the total liquid rate q_t in producers depend on fractional flow rates f_w and f_o, i.e. $q_o = \frac{\lambda_o}{\lambda_o+\lambda_w} q_t$ and $q_w = \frac{\lambda_w}{\lambda_o+\lambda_w} q_t$.

2.3 Data-Based Modeling of Two Phase Flow

The development of dynamical equations in the previous section would lead to a large scale model as the number of gridblocks N increases, and it is always a trade-off between accuracy and complexity of calculation. However, the dynamics of the underlying process can be captured in a lower dimensional space as shown by [34]. In recent years, researchers in both the reservoir engineering and system engineering communities have developed techniques to find low order models, both linear and nonlinear. A common approach is to analyze the pressure, production, seismic and other types of data, and describe the reservoir and the waterflooding based on the information present in the data.

Considering the waterflood as a process and injection and production rates as the input and output, data-based techniques are generally divided into two categories; a) fully data-based techniques: identifying a *mathematical* relationship (sometimes physically meaningless) between input and output[4], b) partially data-based techniques:

[2] For reservoir engineering aspects of relative permeability see [33].

[3] In other words it means that if the fluid is flowing in one direction from one gridblock to another, and if the pressure gradient changes (e.g. near injectors when pressure changes happen due to rate change) such that upstream and downstream pressure gridblock swapped and the fluid has to move in the opposite direction, an excessive force due to relative pearmeability is opposing the fluid flow.

[4] This model could be either linear or nonlinear, or even a neural network. This approach is referred to as Black Box modeling, and choosing the right model set or subspace is not trivial [35].

developing a simple and understandable model structure based on physical intuition, parameters of which are estimated based on the data[5].

We will investigate the role of data, or more specifically the requirements of the training data, in Chapter 3. But before that, we briefly review four such modeling techniques in the following section. The following models are linear and require less computational effort than other techniques, and perhaps that is why they are widely being used in research and practice.

2.3.1 Linear Model Structure

We have seen in Section 2.1 that the waterflooding process has a nonlinear nature. Furthermore, the dependency of the system parameters on the states implies that the system is time-varying as well. However, under a series of assumptions that was discussed in the same section (and will be further studied in the Chapter 3), the process can be approximated by a linear time invariant model.

The model structures that are presented in this section take the sequence of injection rates as the input and the sequence of production rates (liquid rate) as the output. Therefore, for a reservoir with M injection wells and N producer wells, the ideal input/output relationship can be represented as a multi-input multi-output transfer function:

$$\begin{bmatrix} Y_1(z) \\ \vdots \\ Y_N(z) \end{bmatrix} = \begin{bmatrix} G_{11}(z) & \cdots & G_{1M}(z) \\ \vdots & \ddots & \vdots \\ G_{N1}(z) & \cdots & G_{NM}(z) \end{bmatrix} \begin{bmatrix} U_1(z) \\ \vdots \\ U_M(z) \end{bmatrix}, \tag{2.15}$$

where $U_i(z)$ and $Y_i(z)$ are the z-transforms of input and output sequences, respectively. $G_{ij}(z) = \frac{B_{ij}(z)}{A_{ij}(z)}$ is a rational transfer function between the corresponding injector and producer, where $B_{ij}(z)$ and $A_{ij}(z)$ are polynomials of z, in z domain. See [34, 36, 37] for a detailed discussion of state space representations.

A widely used and accepted low order linear model structure in the reservoir engineering community is the capacitance model (CM). In the system identification literature, Finite Impulse Response (FIR) and Auto Regressive eXogenous (ARX) are two widely used models for simple and low order dynamical systems. [1] and [37] have also applied them for identifying inter-well connectivity and predicting the production rates. Subspace Identification is another widely used method for modeling Multi-Input Multi-Output (MIMO) systems.

[5]This type of modeling is called Grey Box modeling in system identification community. Advantageously, model validation is easier and straightforward as the parameters have physical meaning and value range [35].

We will only review the single input single output model $G(z)$ here. However, the extension to MIMO should be straight forward using the Equation (2.15).

2.3.2 Capacitance Model

The derivation of CM is reviewed in more detail in Appendix C. The CM for a single injector and single producer reservoir:

$$Y(z) = \frac{\beta}{1 - \alpha z^{-1}} U(z), \tag{2.16}$$

where $\alpha \triangleq e^{-1/\tau}$ and $\beta \triangleq \Delta t/\tau$ [6], and τ is defined as $\tau \triangleq \frac{c_t V_p}{J}$. As one can see, this model has only one pole that determines the shape of the response and therefore is called a single pole transfer function in system identification literature, which is commonly used for representing simple LTI dynamics.

The generalization of CM for MIMO systems is straightforward by introducing a new parameter γ_{ij} called inter-well connectivity [37]. In this case, the transfer function $G_{ij}(z)$ according to Equation (2.15) becomes:

$$G_{ij}(z) = \gamma_{ij} \frac{\beta_{ij}}{1 - \alpha_{ij} z^{-1}}. \tag{2.17}$$

One should specifically note that, for each pair of such system, the parameter τ_{ij} defines the individual response from input i to output j, or in other words the measure of the dissipation of the pressure between injector i and producer j, while another parameter γ_{ij} determines the contribution of injector i to producer j.

2.3.3 FIR Model

After the popularity and successful application of CM with only a few parameters, [38] proposed a similar model but with more parameters to shape the injection rate response. The only assumption for this model is that for a discretized model the output response is finite and confined to be dependent only on the last L input values. In signal processing this operation is referred to as *filtering*, and such a system has a finite response for any given bounded impulse input, hence the name FIR. For each injector-producer pair, the model can be represented by:

[6] For further discussion about Δt see Chapter 3, but for now assume that discretization time-step is normalized to 1.

$$G_{ij} = \alpha_{ij,0} + \alpha_{ij,1}z^{-1} + \cdots + \alpha_{ij,L-1}z^{-L+1}. \tag{2.18}$$

Unlike CM, the FIR model does not provide any physical information about the underlying dynamics, which makes it harder to validate the parameters. However, FIR model has the major advantage of always being stable, which is suitable for the waterflood modeling as this process is always stable. Note that not only the number of parameters for each transfer function has been increased, but also the structure of FIR is different from CM.

Mathematically, an FIR filter can approximate any LTI system for sufficiently high order L [35]. However, from practical point of view, FIR model is obtained by truncating the length L filter coefficients, the values of which are estimated according to the training data. Although higher L can approximate the model dynamics better, it requires more data (or more informative data) for more accurate estimation of the parameters, otherwise the error covariance of the estimated parameters would become large, which yields more uncertainty. See more discussion in Chapter 3).

2.3.4 ARX Model

A main advantage of both CM and FIR is that the predictor operator is *linear in the parameters*. This means that the parameter estimation boils down into a linear minimization problem. This as well guarantees that a global optimum can be obtained for the estimated parameters. Although linear operation is an obvious advantage, it comes with the cost of undermodeling, due to the ultra simplified structure. As will be discussed in the next chapter, although increasing the model order gives more freedom in shaping the training error, one should note that such undermodeling issues, mainly in form of nonlinearities, can affect the validity of the identified linear models if the assumptions regarding the linearity of the underlying process are not met. We summarize these assumptions at the end of this chapter.

ARX models are also linear in the parameters, and provide more flexibility in shaping the dynamics. A general transfer function between input and output can be represented as:

$$G_{ij}(z) = \frac{B_{ij}(z)}{A_{ij}(z)} = z^{-n_d}\frac{b_0 + b_1z^{-1} + \cdots + b_{n_b-1}z^{-(n_b-1)}}{1 + a_1z^{-1} + \cdots + a_{n_a}z^{-n_a}}, \tag{2.19}$$

where n_d represents the delay in response from input i to output j, and n_a and n_b are the order of the polynomials in denominator $A_{ij}(z)$ and numerator B_{ij}. This structure

can be physically interpreted as how much of the current output is determined from n_b samples of the past inputs, that is discounted by n_a samples of the past outputs. Note that CM is a special case of ARX for $n_b = 1$ and $n_a = 1$. Also, the DCM model in [16] is a cascade of two CM transfer function and hence a transfer function in form of ARX, where $n_b = 1$ and $n_a = 2$ [7]. The double-pole model proposed by [13] is also a special case of DCM with both poles at the same location.

Higher orders of n_b and n_a can be used but they will tend to make the physical interpretation of the poles more complicated. For a highly heterogeneous reservoir with high permeability distribution variance, each area can be represented with a pole.

2.3.5 State Space Model

Subspace Identification (SubID) is another linear in the parameter modeling scheme that is based on the *state space* representation of the system [39]. The main advantage of SubID is that it has a straightforward extension to MIMO systems. Based on the building blocks and assumptions for CM and Equations (C.1) and (C.2) in appendix, derivation of the state space representation for a discrete time system is also straightforward. For a reservoir with N producers and M injectors, one can write:

$$\begin{aligned} \mathbf{x}[n+1] &= \mathbf{A}\mathbf{x}[n] + \mathbf{B}u[n] \\ \mathbf{y}[n] &= \mathbf{I}\mathbf{x}[n] \end{aligned} \tag{2.20}$$

where $\mathbf{y} = [y_1 y_2 \cdots y_N]^T$ is the output vector, $\mathbf{u} = [u_1 u_2 \cdots u_M]^T$ is the input vector, $\mathbf{A}_{N\times N}$ is the state matrix, $\mathbf{B}_{N\times M}$ is the input matrix and $\mathbf{I}_{N\times N}$ is identity matrix of size N. Note that, in this model, the states are in fact the outputs of the system. This representation is introduced by [37] and is called Multivariate ARX, which should not be confused with the ARX model structure that was presented before. The elements of matrix $\mathbf{A}$ and $\mathbf{B}$ are defined as:

$$a_{ij} = -\frac{\delta_{ij}}{\tau_i}, \quad b_{ij} = \frac{\gamma_{ij}}{\tau_i}, \tag{2.21}$$

where τ_i and γ_{ij} have the same definition as in the last section and δ_{ij} determines the contribution of producer j on production rate of producer i. This modeling structure has two main advantages: 1) The effect of producers on each other is taken into account. This is very important especially when the production wells are close and are subject to

[7] Note that the advantage of DCM is that the estimated parameters can be validated versus their physical interpretation, e.g. existence of a fracture. That is why it is not preferred to change DCM into ARX structure.

frequent shut-ins[8]. 2) The parameters of this model have physical interpretation, which makes their validation easier.

2.4 Conclusion

This chapter was aimed at fluid flow modeling in porous media. First, we briefly reviewed the physics of the waterflooding phenomena and derived the PDE's that describe the relationship between pressure and saturation. We showed that these equations are inherently "nonlinear" and their parameters are "varying in time" and state dependent. However, by reviewing the simplification process, we showed that it is possible to approximate the underlying dynamics with linear time invariant models if a number of assumptions are taken into account. These assumptions are limiting in the sense that identifying the parameters of a reliable LTI model, requires training data that contains sufficient variations and length.

Considering the parameters of pressure dynamics in Equation (2.10), one can see that total mobility λ_t depends on saturation S_w, and porosity ϕ and compressibility c_t are dependent on pressure change both in time or space (note that λ is also a function of pressure p). Therefore, if pressure and saturation changes are sufficiently bounded, or for incompressible or low compressible assumption, the pressure equations can be replaced by a linear model.

In Equation (2.14) governing saturation is shown, and it can be seen that total velocity v_t is dependent on pressure gradient and on $\lambda_{o,w}$, and therefore on saturation. Therefore, having sufficiently bounded pressure and saturation changes throughout the field, the saturation can also be approximated by a linear model.

The places in reservoir that have large pressure gradient are near wells and in high permeability channels such as in fractures, and for the rest of the reservoir $\nabla p \approx 0$, (see Chapter 5). Because of low compressibility, pressure changes are also assumed to be almost instantaneous and thus $\frac{\partial p}{\partial t}$ is also almost zero. Generally speaking, the saturation changes in time happen much more slowly than pressure changes and it is not negligible. This in fact implies that saturation related nonlinearity is stronger than pressure related nonlinearity, and pressure related nonlinearity can only be neglected under incompressible flow assumption. In other words wherever in the reservoir that the water oil ratio is significant, saturation nonlinearity is also significant. Note also that areas near wells, the nonlinearity is stronger due to the presence of source term, see Section 2.2.

[8]Shut-in can happen for multiple reasons and might be planned or unforseen.

In contrast to the large scale discretized model with fine grids, we presented a number of techniques to describe the waterflood process with a simple linear model. These models are low order, i.e., only have a few parameters, and have shown promising results in predicting the production rates from injection rates. We have shown that all CM, DCM, FIR, ARX and SubID have a similar MIMO model structure but with different number of parameters to shape the response. In terms of the computational efficiency or the number of parameters per input or output, SubID and ARX method are similar and have more parameters than the others. We discussed that the parameters of such models in terms of existence of a physical interpretation, which can be their major disadvantage. Approximation of a large scale nonlinear process with simple linear time invariant models naturally involves undermodeling, but we will show in Chapter 4 how to improve the reliability of these models using our proposed experiment design.

From what we observed in this chapter, we see that linear low order models are limited and are only valid as long as waterflood dynamics are assumed to be linear and slowly varying. The following assumptions need to be considered in order to guarantee operation in a leaner regime:

- Two phase flow
- Negligible gravity and capillary forces compared to pressure
- Negligible dependency of $\mu_{o,w}$ and $\vec{\mathbf{K}}$ on pressure
- Weak dependency of $\rho_{o,w}$ and ϕ on pressure, thus low compressible flow
- Sufficiently bounded ∇P around injectors
- Low level of heterogeneities

Chapter 3

Data Based Modeling of Reservoir Waterflood

It was motivated in Chapter 1 that linear low order modeling has found many applications in reservoir engineering. In Chapter 2 we reviewed a number of common methods that have recently been widely used in research community. We have shown that these simplified models have similar structure with a number of unknown parameters that need to be estimated according to a training dataset. This process is referred to as Filtering and System Identification in the system identification literature. If the model parameterization is based on some physical principles (greybox modeling) then the identified parameters have physical interpretation that can be used for validation. However, approximation of the waterflooding process with a linear time invariant model (LTI) is mainly based on mathematical intuition (blackbox modeling), where the model parameters are not necessarily meaningful. Now the question is how one can be certain about the range of the estimated parameters and their validity without having the option of using measurement for verification? And if there is no true LTI model, what is the best approximation of the waterflooding with an LTI?

In this chapter, we will demonstrate a set of experiments that show the connection between the conditions on the training data and the reliability of the predictions of the identified mathematical models. The idea is to excite the dynamical modes of the fluid flow by adding predefined variations on injection rates. A series of simulations is done on a simple homogeneous reservoir for 26 predefined production scenarios with different injection sequences. These sequences are different in the amount of variations, their amplitude, and the stage of production in the lifecycle of the reservoir. Seeing the individual effects of each of these aspects on the validity of models, we will conclude the limiting factors of injection scheduling design process. What we learn here will be

applied in Chapter 4 to properly design an experiment that generates an informative training data. The discussions in this chapter contributes as a compliment to section 2.2, where the sources of nonlinearity were reviewed from theoretical point of view.

3.1 System Identification: Brief Review

We have shown in Section 2.3.1 that the injector-producer model can be described in two forms: a) A rational transfer function $G(z)$, b) A set of matrices in state space. In the following, mathematics and statistics of Prediction Error Identification (PEI) and Subspace Identification (SubID) are formally introduced in order to explain how to estimate the parameters of each of these two models.

3.1.1 Prediction Error Identification (PEI)

Representing a nonlinear physical phenomenon such as waterflooding in terms of a linear transfer function is an approximation. In PEI, the output is represented as a relation between the input and a system model $G(Z)$ and a noise model $H(z)$, to account for undesired effects of undermodeling such as system linearization, non-measurable input signals, measurement noise and disturbances:

$$\hat{y}[n] = G(z)u[n] + H(z)e[n], \tag{3.1}$$

where $H(z)$ is a proper rational transfer function and is stable, $e[n]$ a sequence of zero mean, identically distributed, independent (iid) random variable [1] and $u[n]$ is the injection rate and $\hat{y}[n]$ is the "predicted" production rate simply because $e[n]$ is random and the measured output $y[n]$ cannot be regenerated [39].

Let us denote the parameters of a given model by $\theta = [\theta_1 \ \theta_2 \ \cdots \ \theta_{N_\Theta}]^T$, and the true model $G_0(z)$ and $H_0(z)$ by $\mathcal{S} = G_0(z), H_0(z)$. If $\mathcal{M}$ represents all the corresponding models with same parameterization, i.e. $\mathcal{M} := \left\{G(z,\theta), H(z,\theta) \forall \theta \in \mathbb{R}^{N_\Theta}\right\}$, and by assuming $\mathcal{S} \in \mathcal{M}$, then the goal is to find θ_0 (or some estimate of it, $\hat{\theta}$) according to a training dataset $\{\mathbf{u}[n], \mathbf{y}[n]\}$ of length N. Equivalently,

$$\hat{\theta}_N = arg\min_{\theta} \frac{1}{N}\sum_{n=1}^{N} \epsilon^2(n,\theta), \quad \epsilon^2(n,\theta) \triangleq (y[n] - \hat{y}[n])^2. \tag{3.2}$$

[1] Since $e[n]$ is iid, it is enough to know its mean and variance.

One can clearly see that $\hat{\theta}_N$ depends on the training dataset. Thus, the estimated parameters for two different datasets are not necessarily the same. However, $\hat{\theta}_N$ has normal distribution asymptotically, i.e. $\hat{\theta}_N \sim \mathcal{N}(\theta_0, \mathbf{P}_\theta)$, and if $N \to \infty$ then $\mathbf{P}_\theta \to 0$.

The optimization problem in Equation (3.2) has an analytical solution, if one chooses to parameterize $H(z)$ as $H(z) = \frac{1}{A(z)}$, where $A(z)$ is the polynomial in the denominator of $G(z)$ according to Equation (2.19). [39] shows that the least square estimator in Equation (3.2) is linear in parameter θ and it can be written in matrix notation as:

$$\hat{y}[n] = z^{-n_d} B(z) u[n] + [1 - A(z)] y[n] = \phi[n]^T \theta, \tag{3.3}$$

where $\theta = [a_1 \; a_2 \; \cdots \; a_{n_a} \; b_0 \; b_1 \; \cdots \; b_{n_b-1}]^T$ and $\phi[n] = [-y[n-1] \; \cdots \; -y[n-n_a] \; u[n-n_d] \; \cdots \; u[n-n_d-n_b+1]]^T$. Therefore $\hat{\theta}_N$ can be obtained as:

$$\hat{\theta}_N = \left(\underbrace{\frac{1}{N} \sum_{n=1}^{N} \phi[n] \phi^T[n]}_{R(N)} \right)^{-1} \cdot \frac{1}{N} \sum_{n=1}^{N} \phi[n] y[n]. \tag{3.4}$$

As one can see in this equation, $\mathbf{R}(N)$ contains the samples from the training set and in fact is a function of sample covariance. The dependency of the estimated parameters to the input data will be explored further in the next section, where we show how the number of variations in the input data affects the statistical properties of $\hat{\theta}_N$.

3.1.2 Subspace Identification (SubID)

A discretized reservoir model that is presented in Appendix B can be formulated in the state space form as [34]:

$$\begin{aligned} \mathbf{x}[n+1] &= \mathbf{A}\mathbf{x}[n] + \mathbf{B}u[n] + w[n] \\ \mathbf{y}[n] &= \mathbf{C}\mathbf{x}[n] + \mathbf{D}u[n] + v[n], \end{aligned} \tag{3.5}$$

where the state vector $\mathbf{x}[n]$ in general contains the pressure and saturation of each gridblock, input vector $\mathbf{u}[n]$ contains all the source terms as in injection and producer that can be measured, $\mathbf{y}[n]$ represents the output values or the values that we are interested to predict, $v[n]$ and $w[n]$ are Gaussian white noise, and $\mathbf{A}$, $\mathbf{B}$, $\mathbf{C}$ and $\mathbf{D}$ are system matrices. Depending on the parameterization of the system, there might be some variations to this notation. We have shown a simplified version of it in Equation

(2.20), which is derived from Darcy's relation for M injectors and N producers. For this parameterization the states are all observable and can be measured, and in fact are equal to the outputs. The objective of the problem can be defined as: given N measured input/output data points (i.e. training data), find the best estimate of the system matrices. Here, we only revisit the deterministic case where $v[n] = w[n] = 0$. The reader is referred to [40] for more detail on more general cases.

For the system in Equation (2.20) and for an arbitrary integer s, where $N < s << N^2$[2], one can write:

$$\mathbf{Y}_{0,s,N} = \mathcal{O}_s \mathbf{X}_{0,N} + \mathcal{T}_s \mathbf{U}_{0,s,N}, \tag{3.6}$$

where $\mathbf{U}_{0,s,N}$ and $\mathbf{Y}_{0,s,N}$ are block Hankel matrices corresponding to input and output, respectively:

$$\mathbf{U}_{0,s,N} = \begin{bmatrix} u(0) & u(1) & \dots & u(N-1) \\ u(1) & u(2) & \dots & u(N) \\ \vdots & \vdots & \ddots & \vdots \\ u(s-1) & u(s) & \dots & u(N+s-2) \end{bmatrix}, \quad \mathbf{Y}_{0,s,N} = \begin{bmatrix} y(0) & y(1) & \dots & y(N-1) \\ y(1) & y(2) & \dots & y(N) \\ \vdots & \vdots & \ddots & \vdots \\ y(s-1) & y(s) & \dots & y(N+s-2) \end{bmatrix}, \tag{3.7}$$

and $\mathcal{O}_s = [I \ \mathbf{A} \ \mathbf{A}^2 \ \cdots \ \mathbf{A}^{s-1}]^T$, $\mathbf{X}_{0,N} = [x(0) \ x(1) \ x(2) \ \cdots \ x(N-1)]$ and $\mathcal{T}_s$ is defined as:

$$\mathcal{T}_s = \begin{bmatrix} 0 & 0 & 0 & \cdots & 0 \\ \mathbf{B} & 0 & 0 & \cdots & 0 \\ \mathbf{AB} & \mathbf{B} & 0 & \cdots & 0 \\ \vdots & \vdots & \vdots & \ddots & \vdots \\ \mathbf{A}^{s-2}\mathbf{B} & \mathbf{A}^{s-3}\mathbf{B} & \dots & \mathbf{B} & 0 \end{bmatrix}. \tag{3.8}$$

Equation (3.6) relates matrices constructed from dataset to the system matrices. By multiplying both sides to $\mathbf{\Pi}$, the orthogonal projection onto the column space of $U_{0,s,N}$, we have:

$$\mathbf{Y}_{0,s,N}\mathbf{\Pi} = \mathcal{O}_s \mathbf{X}_{0,N}\mathbf{\Pi}, \tag{3.9}$$

because it has the property that $U_{0,s,N}\Pi^{\perp}_{U_{0,s,N}} = 0$. According to [40], the system order and $\mathcal{O}_s$ can be extracted from a singular value decomposition (SVD) of Equation (3.9). Its rank is equal to N and its column space coincides with that of $\mathcal{O}_s$. It is shown by [40]

[2]Larger than number of inputs and less than the length of the training data.

that if O_s is known, the system matrices can be calculated accordingly. They showed that $O_s = \mathbf{U}_{0,s,N}\mathbf{S}_1^{1/2}$, where $\mathbf{S}_M^{1/2}$ is the block of size M of the $\mathbf{S}$ matrix in SVD of $\mathbf{Y}_{0,s,N}\mathbf{\Pi}$.

Before we end this section, it is worth noting that the reader should not be confused by the depth of mathematical derivation of SubID. The main purpose of the above equations are to show the dependency of parameter estimation on training data. The following section shows how the variation in input data can affect the estimation.

3.1.3 Conditions on the Training Data

We have shown in the previous section how the estimated parameter vector $\hat{\theta}_N$ is mathematically dependent on the training data. Clearly, the estimated parameters for two sets of training data are not necessarily the same, and cannot be expected to have similar variance. This section describes the conditions on the training data that affect the statistical properties of the estimated parameters such as their mean, variance, uncertainty bound etc. These requirements can be investigated from two points of view; a) requirements on the reservoir condition from which the training data set is gathered, b) the statistical requirements of the input signal to ensure the data has sufficient information about the dynamics. These two concepts are extremely important and need to be further discussed in details.

A: Reservoir Condition for Data Generation

We have described in Chapter 2 that not only the waterflooding process is nonlinear, but also the reservoir parameters are state dependent and time varying, sometimes with nonlinear variations over time. But under certain assumptions and conditions, the nonlinearities can be assumed to be milder and changes happen more linearly.

In the previous section, we have introduced the concept of "true model" $\mathcal{S}$, and we further made the assumption that $\mathcal{S} \in \mathcal{M}$, where $\mathcal{M}$ represents the set of all the models of the same parameterization. Model structure $\mathcal{S}$ is linear and its parameters are not varying over time, thus it is only able to describe a linear physical relationship.

Therefore, one must ensure that the training data is gathered under predefined conditions in accordance to waterflooding dynamics to guarantee $\mathcal{S} \in \mathcal{M}$. Otherwise, data-based modeling becomes unreliable with inaccurate predictions. Prior knowledge about the reservoir and analysis of the information in the training data can reveal how close the dynamics remained in linear regime.

For the case where the real system $\mathcal{S}$ is not identifiable, or in other words the model structure and the data generating system do not match, the estimated parameters are biased. In this case, although the identified model might be misleading, it is the best approximation of the process asymptotically.

B: Persistently Exciting Data

Data-based model identification is the extraction of the process dynamics information that exists in the data. Therefore, it is obvious that the training data must contain enough information about the process in the first place. It is straightforward to understand that the input signal characteristics determines the amount of information about the system. For example a constant input signal can only provide an insight over the static behavior (steady state) of the process, and there is no information about the dynamical modes of the system, simply because they have not been excited.

Definition 1. Let $u[n]$ be a quasi stationary signal[3], and let the $N \times N$ matrix $\bar{\mathbf{R}}_N$ be defined as the covariance matrix of the signal (a symmetric Toeplitz matrix):

$$\bar{\mathbf{R}}_N = \begin{bmatrix} R_u(0) & R_u(N-1) & \dots & R_u(N-1) \\ R_u(1) & R_u(0) & \dots & R_u(N-2) \\ \vdots & \vdots & \ddots & \vdots \\ R_u(N-1) & \dots & R_u(1) & R_u(0) \end{bmatrix}, \tag{3.10}$$

with $R_u(i) \triangleq \bar{E}[u[n]u[n-i]]$ then $u[n]$ is persistently exciting of order N if $\bar{\mathbf{R}}_N$ is nonsingular, or has full rank.

Persistence of excitation of order n is a property concerning the"variation" that is present in the signal $u[n]$. Note that a sequence of zero mean independent random variables (white noise) is persistently exciting of any finite order, since $\bar{\mathbf{R}}_n = \mathbf{I}_n$ for all $n \in \mathbb{N}$.

We have shown in the previous sections that the least square estimators of PEI and SubID in Equations (3.4) and (3.9) can"uniquely" identify the system parameters, if $\mathbf{R}_N$ and $Y_{0,s,N}\Pi$ have full rank. In fact the minimum order of persistency of excitation required to identify θ_N parameters uniquely is $2\theta_N$ according to [39].

An alternative formulation for the Definition 1 can be proposed in frequency domain, and based on the power spectral density $\Phi_u(\omega)$ of the signal. [39] shows that, signal $u[n]$ is persistently exciting of order N if $\Phi_u(\omega)$ is unequal to zero in at least N points in

[3] An stationary signal has constant statistical properties over time, e.g. mean and variance. These parameters are not constant but bounded for a quasi-stationary signal.

the interval $-\pi < \omega < \pi$. The interpretation of this result is that there exists no moving average filter of order N that is able to reduce the signal to zero.

Injection rates are usually kept constant by production engineers are are usually determined based on pumping capacity and interwell connectivity. Therefore, increasing the level of excitation in training data by adding variations on injection rates must be motivated, as will be discussed in Section 3.2.3.

3.2 Reservoir Model Identification: Simple Example

We run a series of experiments on a homogeneous reservoir, with each experiment using different but known predefined injection rates. We wish to investigate the data requirements reviewed in Section 3.1.3, and see the effect of different input data on the reliability of the identified models. Moreover, we wish to identify any practical and numerical issues that may arise for data collection in real life and using a simulator.

The identified models based on each training dataset are then validated with another dataset, called validation set, which has similar statistical properties as the training set. It will be shown that the reliability of the identified models is the lowest when there is either very low or very hihg variation.

3.2.1 Reservoir Description

A 3D view of disctretized reservoir model HR11 is shown in Figure 3.1, and the corresponding rock and fluid properties are listed in Table 3.1. HR11 has one injector and one producer in the opposite corners of the field. The dimension of this reservoir is $200 \times 200 ft$ and has been discretized into gridblocks of size $5 \times 5 ft$. Waterflooding starts at the beginning of the lifecycle of the reservoir.

3.2.1.1 Rock and Fluid Properties

The parameters of this model are chosen so that only a two phase flow is simulated using the black oil model, i.e., the BHP of the producer is always above the bubble point pressure and below the reservoir pressure. This model guarantees two phase flow in two dimensions, with gravitational force being neglected for the proposed thickness. Water and rock compressibility are constant and independent of pressure, but oil compressibility varies with pressure according to Figure 3.2. Oil and water viscosity are assumed to be constant for the working pressure during the waterflooding.

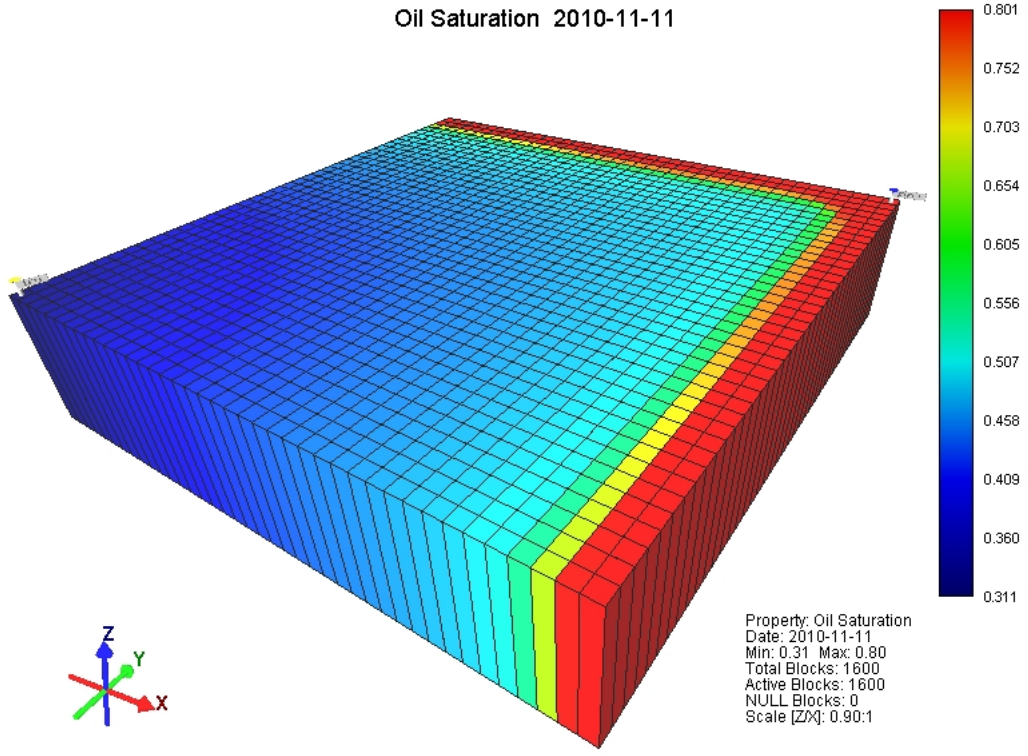

FIGURE 3.1: Oil saturation (S_o) 3D view of the homogeneous reservoir HR11 before water break through. Blue areas have more water and red areas more oil. This reservoir has one injector and one producer on the opposite corners.

Reservoir Dimension (ft)	$200 \times 200 \times 50$
Block Size Dimension (ft)	$5 \times 5 \times 50$
Depth (ft)	2000
Initial Oil Saturation (%)	80
Permeability in X,Y,Z direction (mD)	10
Porosity (%)	30
Rock Compressibility (1/psi)	$1e-6$
Temperature (°F)	100
Oil Density (STD) (lb/ft^3)	56.388
Gas Density (lb/ft^3)	0.0648312
Water Density (lb/ft^3)	62.178
Water Compressibility (1/psi)	3.15633e-6
Water Viscosity (cp)	0.62582
Reference Pressure (psi)	14.69
Bubble Point Pressure (psi)	2080
Initial Reservoir Pressure (psi)	3000
Solution Gas Oil Ratio (ft^3/bbl)	597
Oil Formation Volume Factor	1.29

TABLE 3.1: Rock and Fluid Properties of Reservoir Model HR11.

Figure 3.3 shows the relative permeability k_{rw} and k_{row} versus water saturation S_w. This plot is important since relative permeability is a major source of nonlinearity (for further discussion on relative permeability see Appendix A).

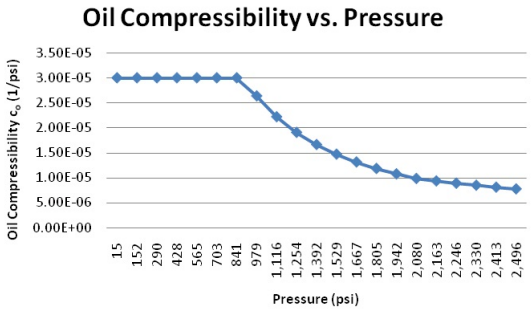

FIGURE 3.2: Oil Compressibility c_o vs. Pressure for HR11.

3.2.1.2 Well Setting

The linear low order model that we are seeking to identify is expected to predict the relationship between the amount of water that is injected and the amount of liquid that is produced. In the primary production scenario for HR11, the injector operates with prescribed rate, chosen to be 100 (bbl/day) and remains constant during the life cycle of the reservoir. The producer well operates under constant bottom hole pressure of 2500 (psi), which is almost 500 (psi) below the reservoir pressure, and 500 (psi) above the bubble point pressure[4] (to avoid any gas production). However, one should note that the user defined conditions does not mean the pressure and saturation in the gridblocks in which the injector and the producer is located are fixed and predefined.

[4]The prescribed rate and constant BHP is chosen because the simulation of the PDE requires boundary condition, here source terms, for both pressure and saturation.

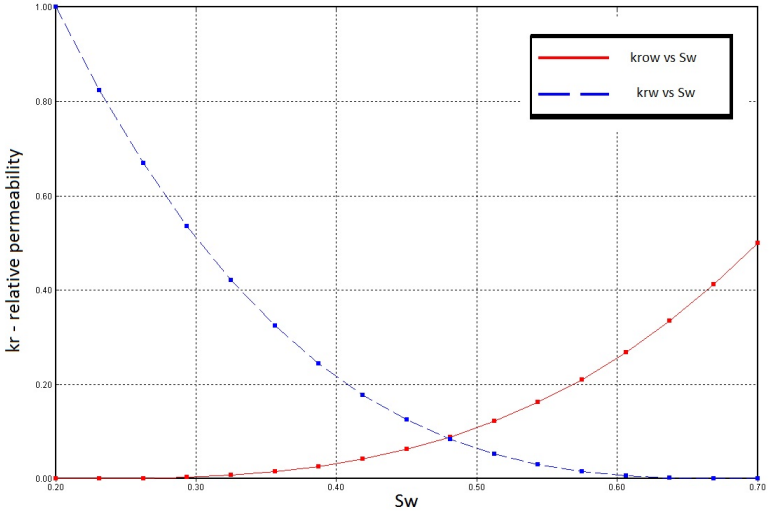

FIGURE 3.3: Oil and Water Relative Permeability vs. Saturation for HR11.

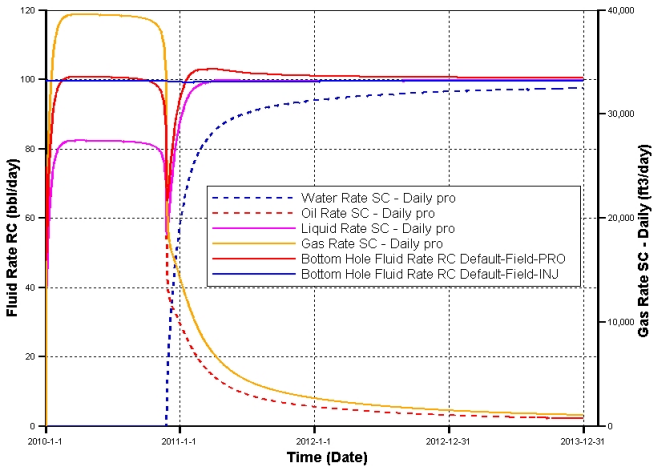

FIGURE 3.4: Oil, water and liquid rate (left axis) and gas rate (right axis) of the producer, and water rate of the injector for the lifecycle of HR11. Constant injection rate is applied from the beginning.

3.2.1.3 Free Run

For the lifecycle of 4 years that the waterflooding is simulated, fractional fluid rate, pressure and saturation of the blocks that contain the wells are represented in Figure 3.4, 3.5 and 3.6 respectively.

Saturation: At the injector, we only have water phase both at the top and the bottom of the well. However, according to Figure 3.4 there are some discrepancies in the saturation of the producer block and the amount of produced oil at the top of the well. The reason is due to the difference between bottom hole and the surface conditions. As the fluid travels to the surface the dissolved gas in the oil is separated and as a result the total of oil and water does not match the total liquid that is produced at the bottom of the well. It can be seen that the increase water cut aggravates this discrepancy. One should note

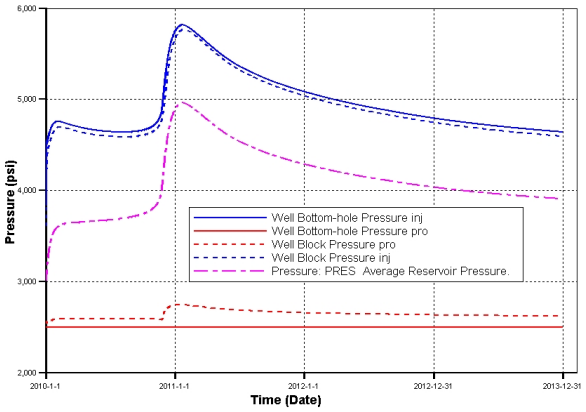

FIGURE 3.5: Well pressure, well gridblock pressure and average reservoir pressure for the lifecycle of HR11. Constant injection rate is applied from the beginning.

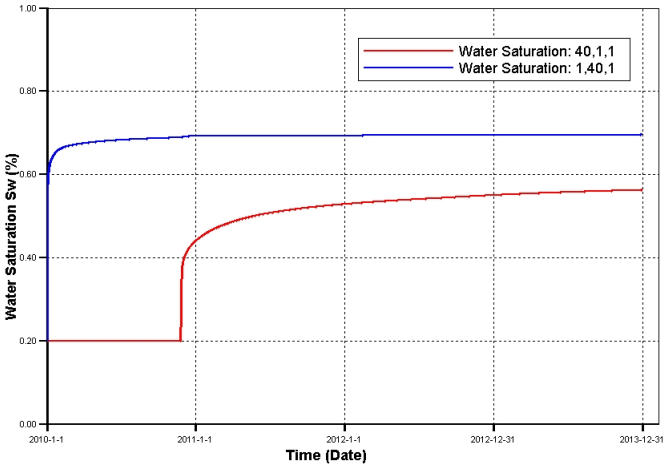

FIGURE 3.6: Water saturation S_w for injector (blue) and producer (red) for the lifecycle of HR11. Constant injection rate is applied from the beginning.

that, especially for the realistic cases where the producer pressure drops below bubble point pressure, this difference must be taken into account, either by calculation or by implementing bottom hole measurement devices.

Pressure: As was discussed before, the BHP of the producer is constant and equal to 2500*psi* as can be seen in Figure 3.5. But the pressure in the same gridblock is slightly above this value and changing. This figure also shows the variation of pressure in injector and the injector gridblock, as well as the reservoir pressure. One assumption here is that the maximum pressure stays below the limits of well equipment such as pumps.

Water Break Through (WBT): During WBT, underlying dynamics show more nonlinear behavior, since changes in saturation are more rapid and reservoir characteristics are changing with relative permeability. Therefore, it is important to know when the water front reaches the producer. Figure 3.6 shows the producer block saturation and it can be seen that WBT happens around 325 days. At about the same time that a major change happens both in pressure and amount of produced liquid, as can be seen in Figures 3.4 and 3.5. In fact the two overshoots in the pressure (in Figure 3.4) happens in the beginning and at the time of the WBT. The rapid change of saturation in the producer, causes a major setback for the mobility of the oil and water phase. As a result, the reservoir pressure builds up (since the same amount of fluid is being injected) and reaches the injector, where it is affected most significantly, as can be seen in Figure 3.5. A sudden decline of liquid production also happens as can be seen in Figure 3.4.

While such nonlinear and transient behavior is significant even for such a simplified model, the process goes back to approximately linear when the water saturation changes

in the producer become insignificant. For example in this reservoir and under such condition, we can say after almost 2 years, S_w changes very slowly.

3.2.2 Model Identification

After introducing the HR11 model and its waterflooding characteristics, we are going to investigate the potential of linear low order model identification. To this end, we study the effect of various training datasets on the validity of the identified models.

A set of input data as a time sequence of injection rate with different characteristics in time and frequency domain is applied to HR11. Each injection rate sequence is applied three times in the lifecycle of the reservoir: before, during and after water break through. The effects of applying varying injection rate on spectral properties of the input/output (or liquid injection/production rate), and on cumulative oil rate, as well as monitoring well and reservoir pressure are investigated.

Injection Rate Sequence: Input

A set of 26 sequences of length 60 days is generated. Each of these sequences is different in the amount and amplitude of variations during its length, while their mean value is the same and is equal to the nominal injection rate of the injector, which is 100 bbl/day. For example the first set,"TR1.IN" is a constant signal of 100, and"TR26.IN" switches more than 30 times randomly between two values 50 and 150 as shown in Figure 3.7. Depending on the number of variations, the frequency content of the input signals is also different. To show this, a series of similar input signals are generated but with longer length. Figure 3.8 shows the frequency representation of a selected number

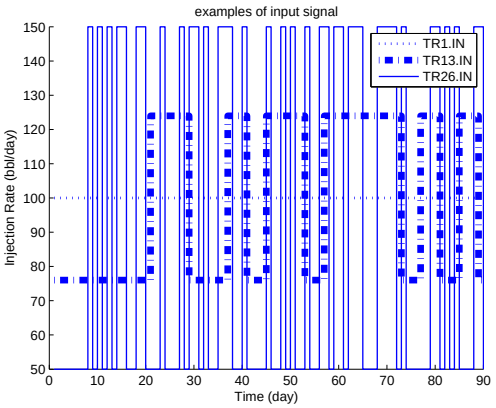

FIGURE 3.7: Examples of input sequences used for training.TR1 is constant, TR13 with medium variation ±25% of nominal value, TR26 with fast variations ±50% of nominal value.

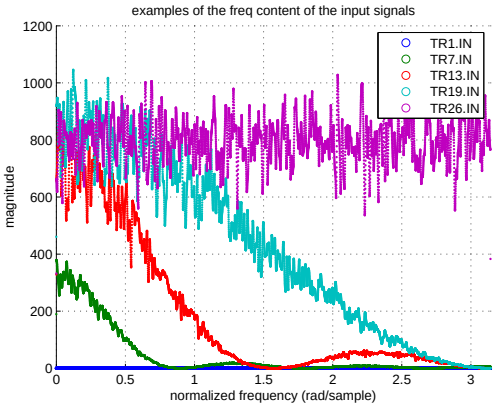

FIGURE 3.8: Examples of frequency content of input sequences used for training. The number of variations increases with the index of the input signal.

of signals. It can be seen that for example input TR7.IN has less frequency content compared to TR26.IN, as well as less energy as a result of different amplitude.

Produced Liquid Rate Sequence: Output

The measured output signal is the rate of produced liquid at the producer. Similar to the input, an example of output signal for three stages of production is presented in Figure 3.9. As expected, when injection rates exhibit less variations, less variations are also observed in the production rates. Similarly, the responses to the inputs with more variation are more high pass fluctuations.

In order to illustrate the scope of the experiments, the injection and production rate for TR13 is represented in Figure 3.10 for the whole lifecycle of the reservoir.

Pressure and Saturation: States

To illustrate the effect of input sequence on the states of the process, i.e., pressure and saturation, we have plotted the states of the grids that contain the wells. Figure 3.11 shows the pressure of the injector and producer gridblocks and the block that is located in the center of the reservoir. Figure 3.12 only shows the saturation of the producer block and the block in the center. Note that the injector block saturation immediately reaches its maximum 0.8 and stays there.

The pressure changes in the gridblocks closer to the injector have more fluctuations. Since the reservoir and fluid have nonzero compressibility, fluctuations damp out spatially towards the producer. Therefore, for a certain radius around the injector $\frac{\partial p}{\partial t}$ is

not negligible and becomes stronger when changes in injection rate are larger, and thus causes nonlinearity in pressure dynamics (see Chapter 2).

In terms of saturation, the only time that $\frac{\partial S_w}{\partial t}$ is negligible is after water break through. Before and during water break through and in the vicinity of the water front, one must expect significant changes of saturation in time. However, the rate is still very slow such that effects of input variations on saturation is relatively small. It is only after WBT that the dominant dynamics of the field is governed only by smooth (and thus approximately LTI) saturation distribution. It must be noted that, the significant variations of S_w during the WBT pushes the system dynamics toward nonlinear regime.

Cumulative Oil

While adding variations on injection rate excites the dynamic modes of the system, it is not desired to affect the amount of produced oil adversely. Figure 3.13 shows

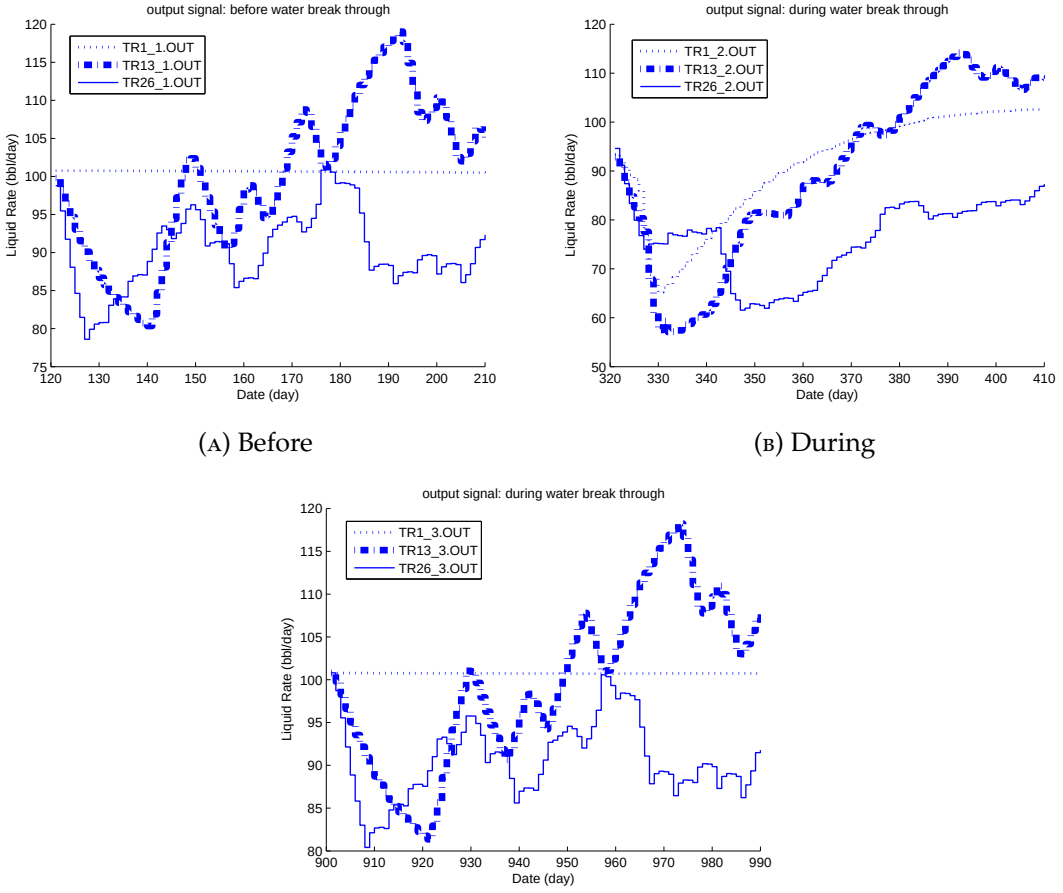

(A) Before

(B) During

(C) After

FIGURE 3.9: Examples of output data for training, before, during and after the water break through.

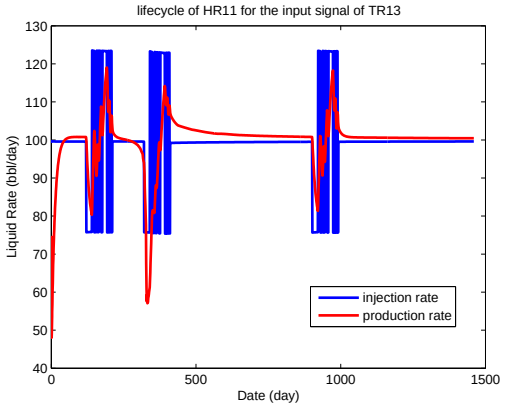

FIGURE 3.10: The lifecycle of the HR11 after applying injection scheduling TR13 for training.

the cumulative produced oil for the lifecycle of the reservoir for a number of injection scenarios. The difference in the amount of produced oil is very low, around 1*bbl*. The reason is that the binary signal that is used as injection rate has similar mean value equal

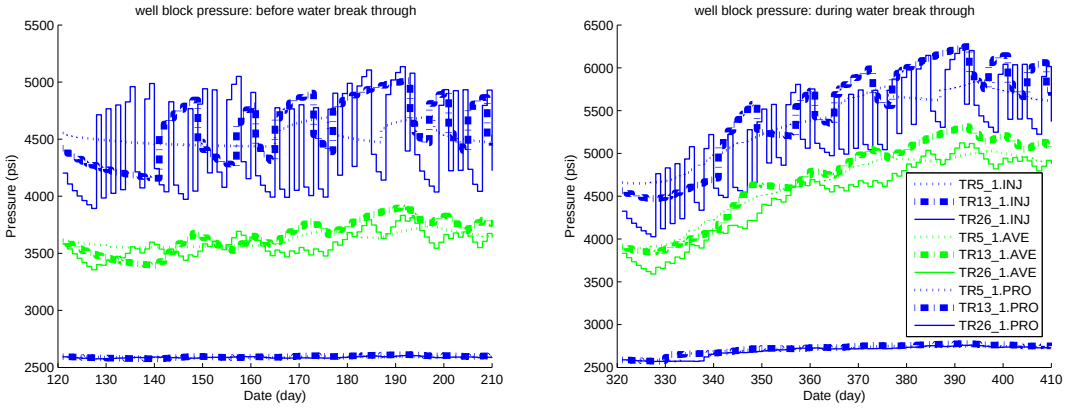

(A) Before (B) During

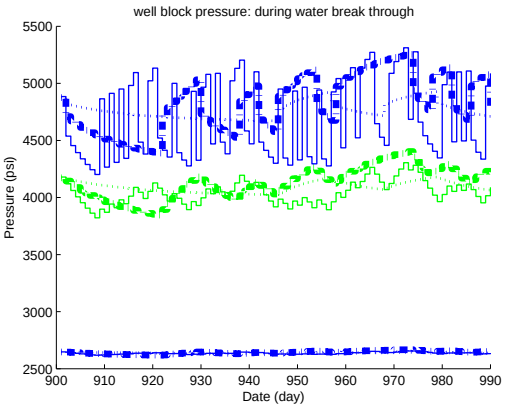

(C) After

FIGURE 3.11: Gridblock pressure changes due to the applied input signals. Producer block (bottom blue), center block (middle green) and injector block (top blue).

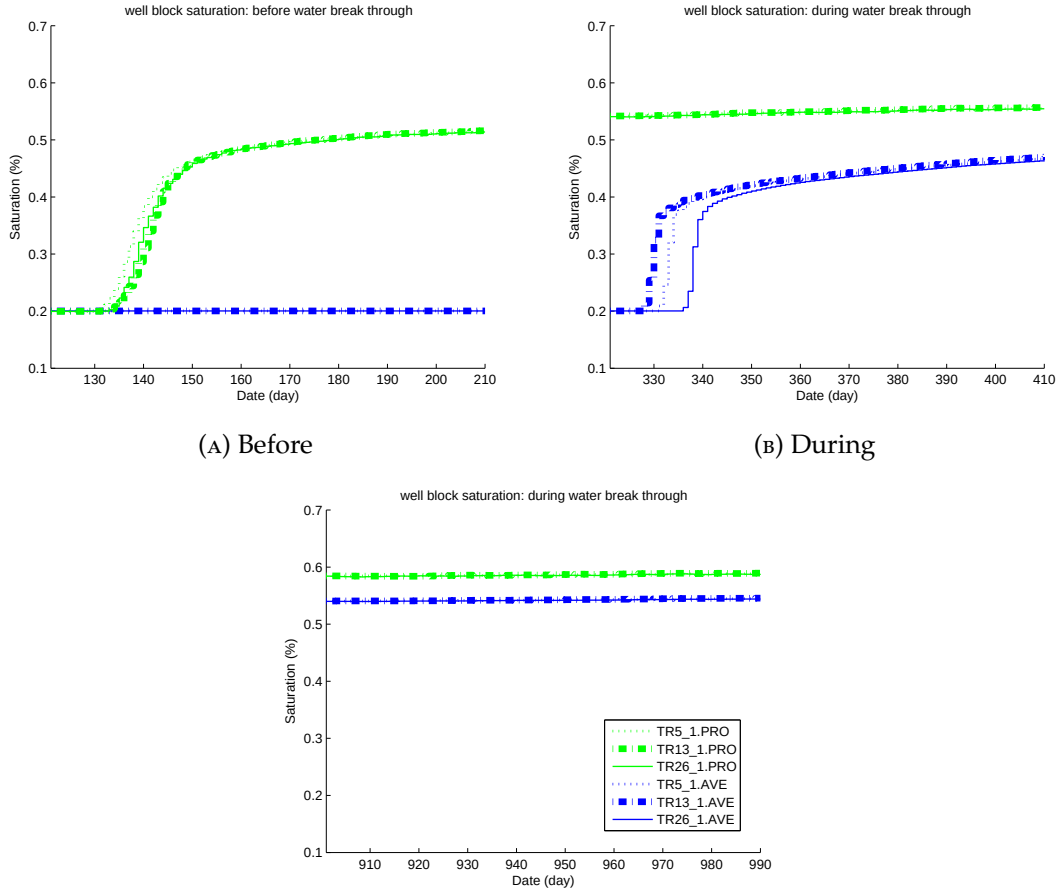

(A) Before

(B) During

(C) After

FIGURE 3.12: Examples of gridblock water saturation S_w changes due to the applied input signals. The gridblock at the center (green) and the producer gridblock (blue).

to the constant rate of TR1, that means that on average the same amount of water has been injected into the reservoir. This result is very important and verifies the minimal effect of the added variations on the achievable profit.

Training and Validation

For each of the experiments in this section, we have also generated a set of validation input sequences, with similar time and frequency domain properties. A model with a given structure (i.e., fixed number of parameters) is trained with each training data set, and simply validated with its corresponding validation data set. Moreover, all the models are also validated against a dataset that is obtained under conditions different than those used for training, to evaluate the model reliability.

We investigated 5 types of models here:

- 1^{st} order ARX, or Capacitance Model (Figure 3.14).

- Distributed Capacitance Model (Figure 3.15).
- 2^{nd} order ARX (Figure 3.16).
- FIR model of order 14 (Figure 3.17).
- SubID of order 2 (Figure 3.18).

The fit are calculated based on:

$$\text{fit } \% = 100\left(1 - \frac{\| y - \hat{y} \|}{\| y - \text{mean}(\hat{y}) \|}\right) \tag{3.11}$$

where y is the measured output, and $\hat{y}$ is the simulated output from the identified model.

3.2.3 Model Analysis and Discussion

The first consistent observation in all the experiments is the poor performance of all the models during WBT. This is mainly due to the significant nonlinear dynamics that governs the process during the change of saturation. Moreover, it can be seen that before and after WBT, the validation fit of all the identified models for various training sets is very similar. While there is no single injection schedule that outperforms others for all model structures, there is one training set for each model parameterization that yields the highest validation fit.

For CM, the overall best fit for training and validation is the best for TR5-TR10, which means small variations and low amplitude suffices for good identification. For a slightly more complicated model structure, such as DCM and 2^{nd} order ARX, TR5-TR10 are

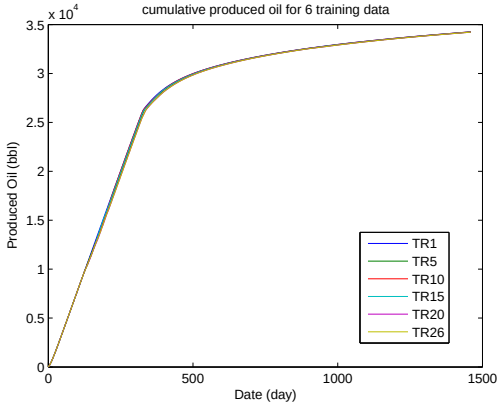

FIGURE 3.13: Examples of cumulative produced oil for the lifecycle of HR11 for different input signals.

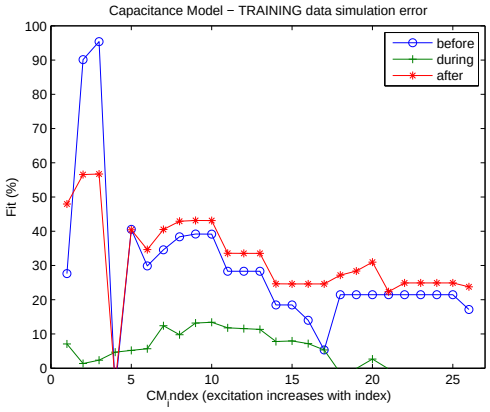

(A) Capacitance Models training fit.

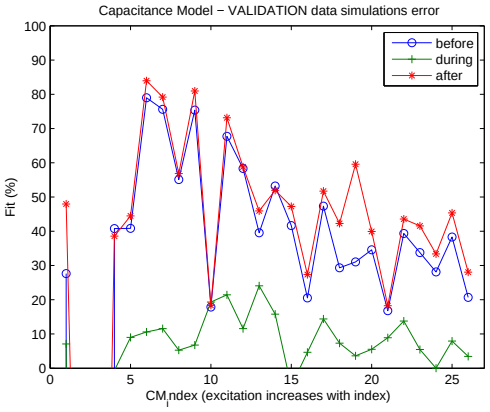

(B) Capacitance Models validation fit.

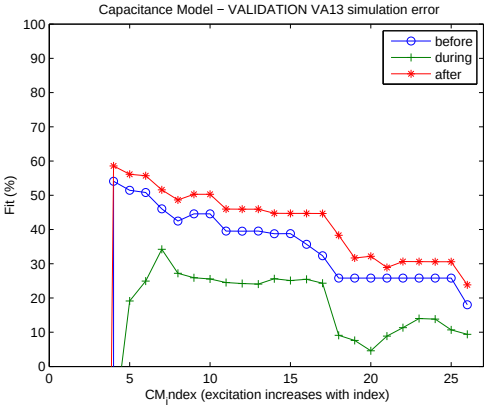

(C) Capacitance Models validated against VA13.

FIGURE 3.14: Training and validation fit for the identified models of Capacitance Model.

still outperforming others. FIR of order 14^{th} has 3 times as many parameters and requires more persistently exciting data, which is why TR10-TR14 are more appropriate. However, the validation fit is almost 10% lower compared to CM, DCM and ARX. The reason is the short length of the experiment relative to the number of unknown parameters. As a result, the training fit is high and validation fit is low.

Similar to FIR, State Space models have many parameters, and clearly show better fit in training. The results in Figure 3.18 shows that TR16-TR26 have excited the reservoir substantially and variations in injection rate cause a drift towards nonlinearity, and thus worse performance in terms of identification.

Another characteristic of the signal that can be investigated is the length of the training data or the experiment. Since the dynamics of the waterflood are constantly changing and the condition of the reservoir is not repeatable, the choice of the length of the experiment is not trivial as it determines the "working point" of the process. Waterflood is similar to batch process in chemical engineering plants, where a batch is produced in a single run. While more data is naturally more advantageous in terms of the amount

of information it carries, care must be taken as to keep the process around that working point. During WBT the experiment must be short since the change in dynamics and thus working point happens more rapidly. But before or after that, a longer experiment is preferable (more on this in the next chapter).

Similarly, the model order can directly affect the validity of the models. While models are suffering from underfitting during the water break through, e.g. see Figure 3.14a and 3.14c, overfitting also becomes an issue for high orders of FIR models, as seen in Figure 3.17a and 3.17c.

3.3 Conclusion

In this chapter we have studied the challenges of linear low order model identification of reservoir waterflooding. These challenges are mainly due to the fact that the identified

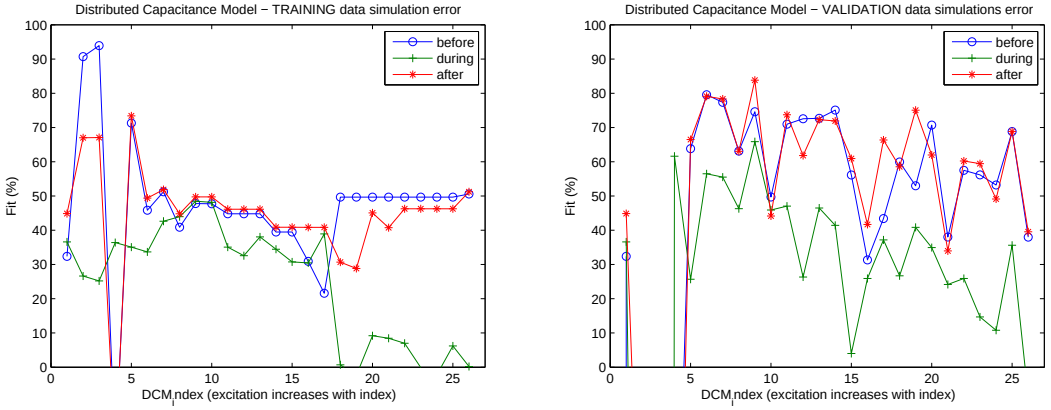

(A) Distributed Capacitance Models training fit. (B) Distributed Capacitance Models validation fit.

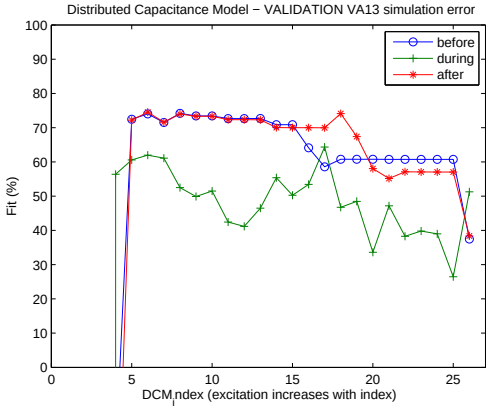

(C) Distributed Capacitance Models validated against VA13.

FIGURE 3.15: Training and validation fit for the identified models of Distributed Capacitance Model.

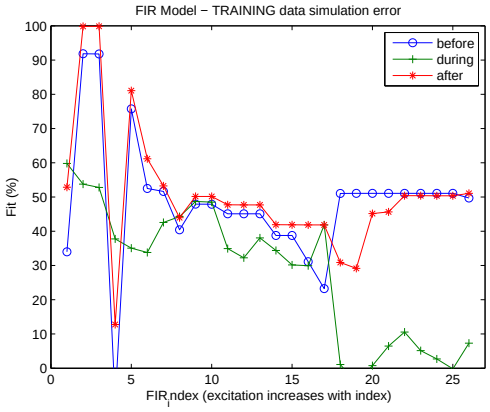

(A) 2nd Order ARX Models training fit.

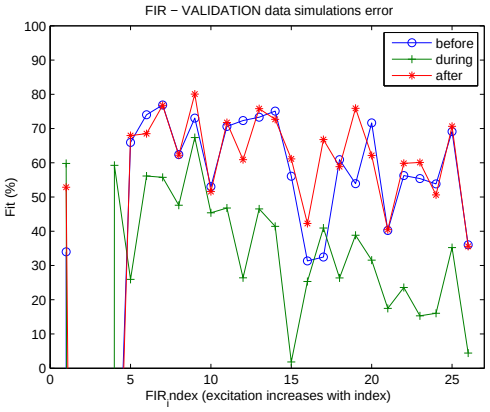

(B) 2nd Order ARX Models validation fit.

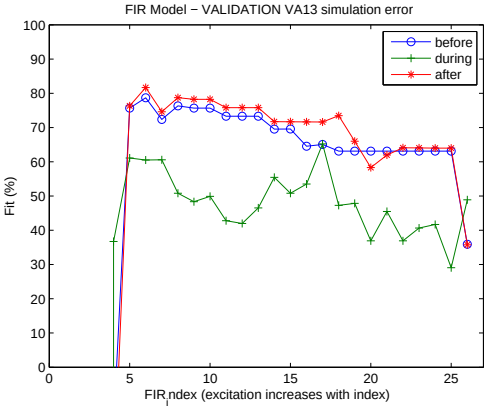

(C) 2nd Order ARX Models validated against VA13.

FIGURE 3.16: Training and validation fit for the identified models of 2nd Order ARX Model.

models do not have clear physical interpretation even if they are capable of reasonably accurate predictions. Since the underlying dynamics are nonlinear, these models are usually viewed with significant skepticism and doubt. In this study we have shown that some of the blame must be directed towards the training data and the condition of the experiment. A number of experiments are simulated for a simple reservoir, each designed such that they take the reservoir into various working points and regimes, e.g. fast changing vs. slow changing, or small vs. large fluctuations. We see that linear low order identification cannot be entirely discarded, since we can achieve high training fit as well as high validation fit for some of the experiments. More importantly, since the total amount of injected water on average is the same, we have shown that adding predetermined variations in any of the 26 experiments does affect the total amount of produced oil.

Based on the results, it can be said that variations in injection rates determine the validity of the identified models. A model with 70% validation fit is a very good candidate for any feedback control system. With abundance of sensors and actuators, a well designed

one-step-ahead predictor can provide highly accurate predictions. For example, one can define a study to design a feedback controller to force the produced oil to follow a certain trajectory by manipulating the amount of injected water. The identified LTI models can also be used for production optimization, for example by field engineers to obtain a better overall field sweep and minimize the amount of dead oil. However, an LTI model for such purpose must have a higher accuracy, which we suggest an iterative experiment design for data acquisition.

The length of the experiment (or the number of data in the signal) can be investigated to see its effect on the validation fit. Since the dynamics of the waterflood are constantly changing and the condition of the reservoir is not repeatable, the choice of the length of the experiment is not trivial as it determines the working point of the process.

The observations in this chapter imply that the statistical properties such as amplitude and variations of the injection rates signal can affect the reservoir condition and its working point, and consequently the validity of the LTI models. Since the models are

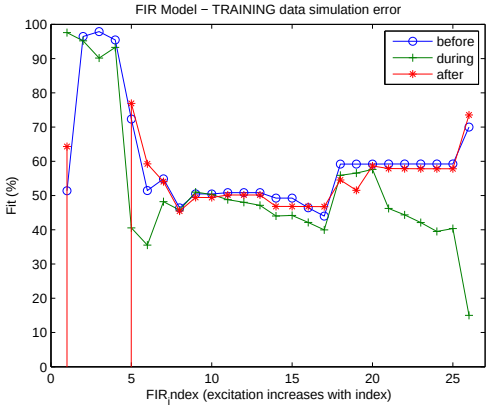

(A) 14th Order FIR Models training fit.

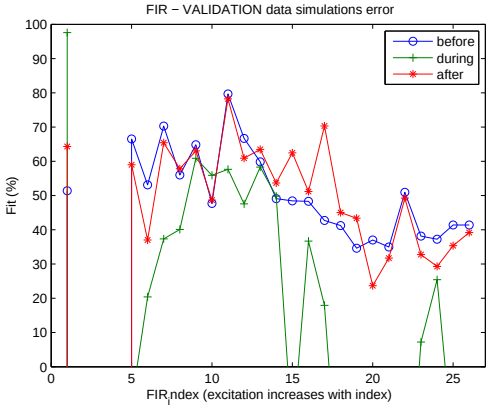

(B) 14th Order FIR Models validation fit.

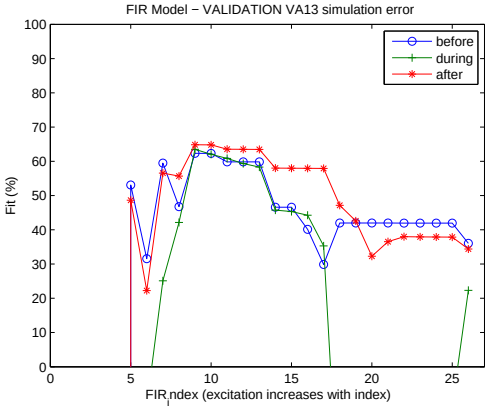

(C) 14th Order FIR Models validated against VA13.

FIGURE 3.17: Training and validation fit for the identified models of 14th Order FIR Model.

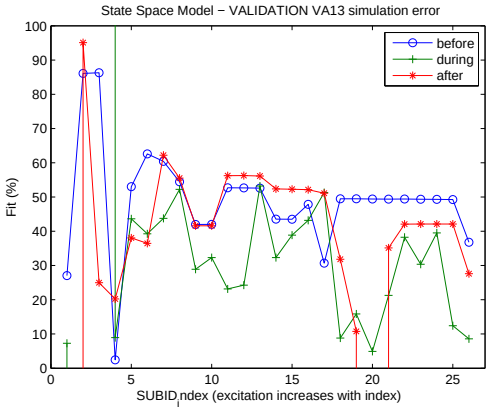

(A) 2nd Order State Space Models training fit.

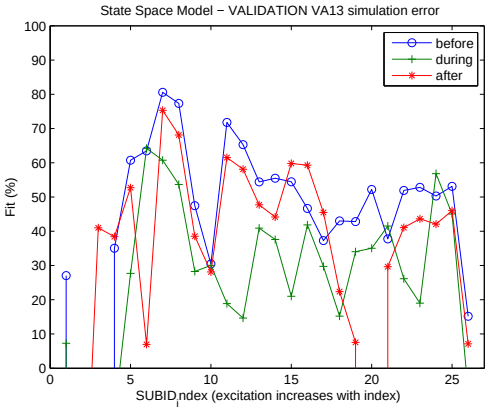

(B) 2nd Order State Space Models validation fit.

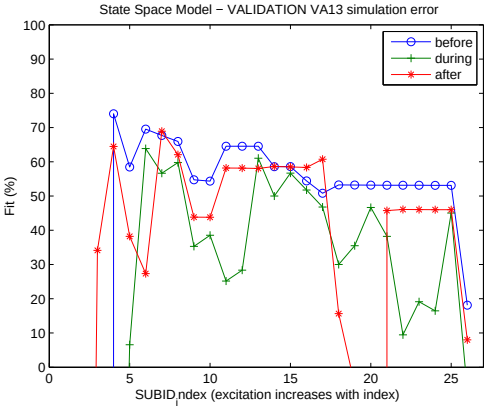

(C) 2nd Order State Space Models validated against VA13.

FIGURE 3.18: Training and validation fit for the identified models of 2nd Order State Space Model.

linear and time invariant, reservoir dynamics should also remain in linear (or close to linear) regime, or otherwise the model identification becomes meaningless. How large of an amplitude in injection rate can shock the dynamics into its nonlinear mode? And how fast are they required to be for the model to be reliable models? The answer to these questions can be found in the next chapter, where we have introduced a framework to design an appropriate and informative training data.

Chapter 4

Injection Scheduling Design: Methodology and A Full Simulation Example

The linear low order models that were discussed in the previous chapter, require an informative training data set for parameter estimation. In fact not only just one training dataset, but many, since the dynamics of waterflooding change over time, the parameters must be updated with the most recent measurements. So how do we know a training dataset is sufficiently informative? And how do we design injection rates to achieve informative training?

Informative data does not necessarily mean more data or less noisy measurements [41]. Informative data is the one that is obtained under controlled and known conditions. Note that the model parameters which are the unknowns, basically determine the dynamical behavior of the system, and can only be estimated if their corresponding dynamics are excited. An input signal with certain variations must be designed based on prior knowledge of the system. If there is none available, a number of preparatory step response should be applied. Depending on how accurate our knowledge of the system is, the identified models may require another training set, or an update due to changing dynamics.

Figure 4.1 shows a schematic representation of model identification as an iterative process [35]. Some of the elements of experiment design can be minor and only require post processing, but some need major changes in the experiment and require a new set of dataset.

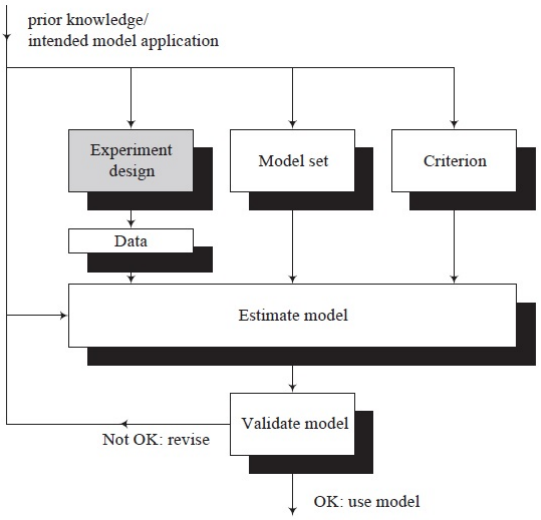

FIGURE 4.1: System identification procedure and experiment design.

In this chapter we are investigating how production data can be used to learn about the waterflood process so that a better experiment can be designed. First we review the characteristics of input signal, such as frequency content, amplitude of variations and etc. To show how these characteristics must be chosen, we have simulated a full example that illustrates how to gain knowledge about the system by preparatory experiments. As a result, an injection sequence is scheduled and a Capacitance Model (CM) model is identified.

4.1 Experiment Design

An input signal (i.e., a set of injections sequences in our case) must have certain properties before it can be used for parameter estimation of data based modeling. On the one hand it must have large enough variations to excite the relevant dynamics, and on the other hand the reservoir cannot be over excited or otherwise nonlinearities of the variable states becomes so strong that they cannot be approximated by linear low order models. The training data set must have sufficient data points, but waterflooding is a very slow process and measurement requires weeks or even months of observations. Moreover, despite being very slow, as the process evolves the underlying dynamics are constantly changing due to the state dependency of the parameters. Since we know that the identified models are Linear and Time Invariant (LTI), what is the optimal length of an experiment?

The answer to this question depends on the underlying process, i.e. the *production* setting of the waterflood and the *reservoir* type and its properties. In what follows,

we review the design parameters of the experiment from production and reservoir engineering point of view. We then summerize our findings and propose a methodology in the Section 4.1.6.

4.1.1 Sampling Time

Approximation of a continuous system with a discrete model requires a choice of sampling time Δt. Smart oil fields are expected to be equipped with several measuring devices on each well, and often the injection and production rates are reported daily. [13], [12], [15], [1] and [42] have all used daily sampled measurements. Smart oil fields are expected to be equipped with several measuring devices on each well these days, and often the injection and production rates are reported daily. If the frequency of the measurement is not an issue, it is preferred to have small Δt. However, the sampling interval cannot be arbitrarily short if we wish to capture the fast dynamics of the process and avoid aliasing. Considering Nyquist-Shannon sampling theorem [35], the upper bound of sampling interval should be:

$$\Delta t < \frac{\pi}{2\omega_b}, \tag{4.1}$$

where ω_b is the bandwidth (or the band of interest for control purposes) of the process. An estimate of ω_b can be obtained by a well-test, or using a step response analysis that shows the slowness/fastness of the producer in response to changes in the injectors. Note that determining an upper bound of Δt is very important, especially when daily rate measurements are not possible. After measurement, it is typically assumed that the production rate p(t) of the producer is such that,

$$p(t) = \text{constant}, \quad \text{for} \quad k\Delta t < t < (k+1)\Delta t, \tag{4.2}$$

which might not be necessarily true specially when production rate $p(t)$ changes rapidly during the early stage of waterflooding. Therefore, depending on how fast the reservoir dynamics are changing, Δt cannot be very long, otherwise the desirable fluctuations in the output will be masked.

4.1.2 Signal Power and Frequency of Variations

In the classic system identification literature, it is desirable for the frequency content of the input signal to have more energy around the bandwidth of interest of the system. Bandwidth of interest is defined as the frequency range in which the fastest pole of the

system is located. [37] has done an extensive analysis for MIMO system and showed that the required signal property in frequency domain can be summarized as

$$P_\theta \propto \frac{1}{N}\frac{\Phi_e}{\Phi_u}, \tag{4.3}$$

where P_θ is the covariance matrix of the parameter estimation, Φ_u and Φ_e are the power spectral densities of input and noise respectively and N is the number of measurement. Equation (4.3) intuitively means that the energy of the input signal should be large and preferably concentrated on the frequencies that are most sensitive to the target parameters. Consider the Capacitance Model (CM) structure, where an estimate of the location of the pole of this transfer function is available (i.e., the time constant τ_m). Then the input signal is required to have more energy around that frequency in order to be estimated more accurately. Therefore, it is only required to know roughly where the fastest pole of the MIMO system is located to determine the upper bound of the input signal frequency content. Such an estimate can be obtained by a pressure or rate transient well test or by using an experimental equation.

The dynamics of the waterflooding are of slow nature and therefore the injection schedule does not require having fast changing daily injection rates. In fact excessive frequency in the injection rates may cause nonlinear behavior in the system. Alternatively, if one has a reasonable estimate of the $t_{set,95\%}$ (the time it takes for the system to settle within 95% of its steady state), the frequency band of interest can be easily determined by looking at the Bode plot of a first order LTI system with similar settling time. A white noise signal has equal frequency content for all frequencies and can be filtered (low pass) by this system to filter all of its unnecessary high frequency content.

4.1.3 Experiment Length

As can be seen in Equation (4.3), using more data points N is desirable in the sense that it reduces the variance of θ. Moreover, the length of the experiment T_N is related to N by $T_N = N\Delta t$. A general rule-of-thumb for the lower bound on the total experimentation time T_N is 5-10 times the largest relevant time-constant in the process [35]. Because the time constant is directly related to the settling time of the step response, we will see in in the next section that a meaningful estimate of Δt can be obtained by a well test.

It is also important to note that to be able to detect the individual effect of multiple injectors on a single producer, the variations in the scheduled injection rates must be uncorrelated between producers [42]. Generating uncorrelated short signals with slow

variations is not practically possible. Therefore, the lower bound is also constrained for fields where each producer is potentially being affected by multiple injectors.

Furthermore, note that it was initially assumed that the system is operating around a steady state working point, or at least the flooding process stays in the same regime during the acquisition of the training data for identification. Therefore, on the one hand slow dynamics of saturation requires longer T_N, while on the other hand T_N must be short since the reservoir properties and flooding dynamics are changing over time, and thus the reservoir is likely to drift from one working point to another, even without any field development. We will see in the following section that a mature reservoir can stay around a certain operational point for a long time, so that the rate of change in system parameters is very slow and linear.

From the above discussion, the maximum length of the experiment is constrained by the normalized average saturation change of the reservoir during the time T_N. This is in accordance with the fact that nonlinearities are more severe during the early stages of the waterflooding and especially in the early stages of water break-through where saturation changes more rapidly.

4.1.4 Amplitude of Variations

Variations in the injection rates cannot be arbitrarily large due to two reasons: 1) Pumping equipment has a limited capacity, 2) For certain reservoir types and under some condition, large and rapid changes may drift the process out of linear regime. It is a very common situation in system identification that large variations in input can cause unwanted nonlinear behavior. Increasing or decreasing the injection rate too frequently changes the pressure pattern around the well, which eventually affect the amount of produced fluid at the producer.

Pressure constraints directly influence the allowable range of the variations in injection rates. In finite difference method (FDM) simulation, the pressure difference between the two sides of each grid block causes the fluid to flow. The pressure in the gridblocks closer to an injector is not only higher compared to the rest of the reservoir, but is also more sensitive to the variations of the injection rate. The resulting pressure gradient damps through the reservoir until it meets a production well. In other words, the pressure gradient caused by injection rate variation is steeper in the grid blocks closer to the injectors. This means that if the pressure variation remains within a certain range in the vicinity of the injector, average reservoir pressure variation is guaranteed to remain in that range in areas far from the injectors too.

One way to determine the maximum allowable amplitude that does not disrupt the linearity regime of the system is by conducting a *stairway experiment* [35]. In this experiment, the amplitude of the input is increased incrementally and the output is measured carefully. If the output increases according to the law of superposition, it implies that the system is in the linear regime.

One can look at the pressure distribution around the injector and determine the maximum range for the amplitude based on analytical or heuristic relationships. This is in fact true because the pressure gradient caused by injection rate variation is steeper around the injectors. This means that if the pressure variation remains within a certain range in the vicinity of the injector, average reservoir pressure variation is guaranteed to remain in the same range in areas far from the injectors too. For example, near well pressure P_{wf} for steady-state single phase flow (water or oil above bubble point pressure) can be described as [43]:

$$P_R - P_{wf} = -\frac{\mu B q}{2\pi k h} \ln \frac{r_e}{r_w}, \tag{4.4}$$

where P_R is average reservoir pressure, B is oil/water formation volume factor, q is the flow rate with negative sign for production and positive for injection well, h is the depth of the well, r_e is reservoir effective radius and r_w is the distance from the well.

Assume that for a given reservoir pressure P_R, we would like to see a maximum of $80\%P_R$ within $20\%r_e$ around the well. The maximum rate q_{max} can be determined from Equation (4.4), and can be used as an upper bound for maximum injection rate. Then the amplitude can be chosen between $\frac{1}{2}q_{max} \leq q \leq q_{max}$, or $\pm 25\% q_{nominal}$ whichever is tighter[1].

Note that beside linearity issues, BHP is primarily limited by field constraints (such as pumping capacity, etc.) and most injectors are usually working at their maximum limit. In this case, variations can only be in form of decreases in the injection rate, which naturally cause pressure decline and less produced oil.

4.1.5 Signal Type

The type of the predetermined variation is important because it is desirable to avoid unnecessary production decline due to injection rate variation. Random Binary Signals (RBS) or Pseudo-Random Binary Signals (PRBS) are a type of white noise-like signals with values that alternate between two predefined amplitudes. [37] has shown that if PRBS injection rate is applied, the overall trend of the pressure decline and saturation is

[1] Motivation for this trade off is heuristic and based on the observations in Chapter 3.

similar to the case where the injection rates are kept constant, which is in accordance with our qualitative results shown in the previous chapter, e.g. see Figure 3.13. Generating an RBS signal is very straightforward if its length, amplitude and frequency content are known (see [35]).

4.1.6 Methodology

To better understand the design parameters of the input signal and how to determine them, we summarized the above discussions in Table 4.1, which shows the design parameters, their statistical requirements, physical constraints and how to design them.

4.2 Multi Fracture Tight Reservoir Model

Tight diatomite reservoirs are among the most common in California. In this type of reservoir oil is trapped in a very low permeability rock and it is extremely hard to push it after the primary production stage. Usually there is a number of naturally or artificially made fractures in the field that help increase the mobility of the oil and water. As a result, some injector-producer pairs have higher connectivity depending on the direction of the fracture. Detecting the fracture direction, not only helps improve the oil recovery factor of the reservoir, but also gives insight over possible further field development, e.g., new well locations or well repairs.

The example reservoir FR34 that is used in this section has similar properties to the reservoir model HR11 that was used in Chapter 3. The two dimensional FR34 has 3 injectors in the bottom and 4 producers in the top, and has only one layer. The permeability map with fracture directions is shown in Figure 4.2. The permeability of the fractures is 500 times larger than that in other areas of the reservoir. From this figure, one should expect a higher connectivity between $INJ2$ and $PRO1$, and between $INJ3$ and $PRO4$.

The reservoir dimension is $600 \times 200 ft$ and is regularly discretized with block size of $4 \times 4 ft$. Oil, water and rock properties are presented in Table 4.2 and are similar to those of HR11. Fluid flow is simulated in the simulator using Black Oil model, and producers Bottom Hole Pressure (BHP) is fixed to be above the bubble point pressure to guarantee two phase flow simulation.

	Signal Requirements	***Physical Constraints***	**Design Factor**
Sampling Time	$t_s/15 < \Delta t < t_s/5$, t_s *is the step response settling time,* $\Delta t < \frac{\pi}{2\omega_b}$, ω_b *is bandwidth of system*	*Available measuring devices/techniques on the field*	Fastest settling time of all well pairs in a well test step experiment
Frequency	*Freq. content of* $2-4\times$ *system bandwidth or fastest pole*	*No constraints, modern injection pumps can be programmed for fast variations*	Bandwidth of the existing models or fastest settling time of the well-test
Amplitude	*Large enough to mask noise effect on output (of any type)*	*Pressure changes near injector stay bounded to remain in linear regime. Large enough to cause visible effect on the production rate*	Field knowledge, empirical relationships, noise of the measuring devices. $\frac{1}{2}q_{max} \leq q \leq q_{max}$, or $q_{nominal} \pm 50\%q_{nominal}$
Length	$5-10\times$ *largest (slowest) time constant of the system*	*Varying dynamics of the reservoir, field development, change of working point*	Slowest settling time of the well-test
Type	*RBS or PRBS white noise like signal*	*Field pressure drop and total production drop*	Low pass filtering for the desired frequency content
Uncorrelated Sequences	*Necessary for MIMO systems*	*Long and slow varying changes for multiple injectors*	Verified before applying

TABLE 4.1: Summary of the design parameters and how to choose them for *Injection Scheduling* in a mature waterflood reservoir.

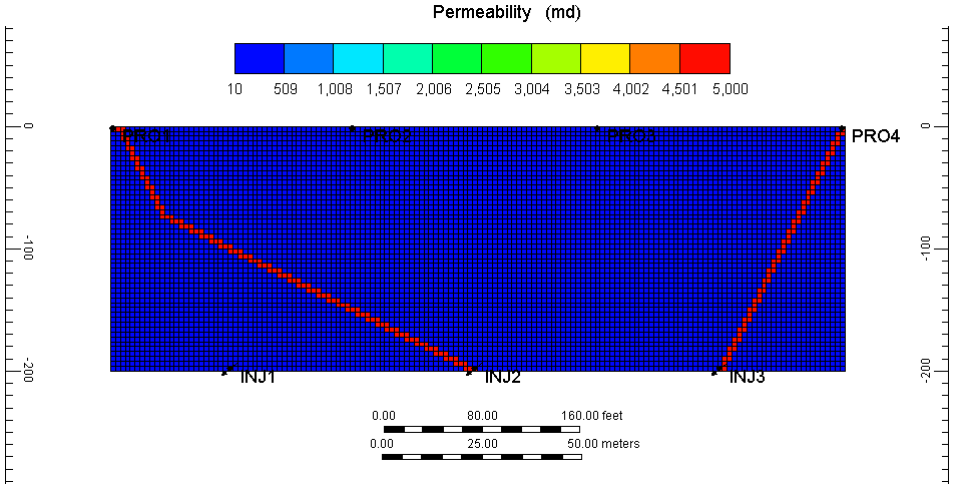

FIGURE 4.2: Permeability map of the reservoir model FR34. Permeability is the same for i, j and k direction.

4.2.1 Well Settings

The lifecycle of this reservoir is chosen to be 5 years. We have run the initial simulation for this lifecycle with constant injection rates. Production rates of individual producers are shown in Figure 4.3. The BHP of the producers are all constant to be 2500 *psi* and water is injected at the rate of 100 bbl/day. While the water front reaches at PRO4 only after 14 days and PRO1 after 23 days, it will take 1149 days for it to reach PRO2 and will never reach PRO3 during the 5 years, see Figure 4.5. The oil saturation distribution

Reservoir Dimension (ft)	$600 \times 200 \times 50$
Block Size Dimension (ft)	$4 \times 4 \times 50$
Depth (ft)	2000
Initial Oil Saturation (%)	80
Matrix Permeability in X,Y,Z direction (mD)	10
Fracture Permeability in X,Y,Z direction (mD)	5000
Porosity (%)	30
Rock Compressibility (1/psi)	$1e-6$
Temperature (°F)	100
Oil Density (STD) (lb/ft^3)	56.388
Gas Density (lb/ft^3)	0.0648312
Water Density (lb/ft^3)	62.178
Water Compressibility (1/psi)	3.15633e-6
Water Viscosity (cp)	0.62582
Reference Pressure (psi)	14.69
Bubble Point Pressure (psi)	2080
Initial Reservoir Pressure (psi)	3000
Solution Gas Oil Ratio (ft^3/bbl)	597
Oil Formation Volume Factor	1.29

TABLE 4.2: Rock and Fluid Properties of Reservoir FR34.

after 5 years is shown in Figure 4.4, and it can be seen that oil has not been swept evenly and the reservoir still has a lot of unproduced oil.

4.3 Preparatory Experiments

The methodology introduced in Section 4.1.6 requires some basic knowledge about the system, even before the first experiment is applied. There are two aspects of the injection scheduling that needs to be determined before it can be properly designed:

- The frequency range that captures the most important reservoir dynamics,
- An estimate of the level of injection rate, like nominal rate and extreme amplitude q_{max}.

Preparatory experiments are not specifically aimed at estimating the parameters of the process at hand, their goal is to obtain just enough information about the process in order to enables the proper design of an identification experiment.

The free-run test that was performed on FR34 (and similarly for HR11) is very important in the sense that the existing noise and other sources of disturbances can be detected. Moreover, for a time varying system such as waterflooding, it is indicative of how much of the output behavior is in fact a result of changes in injection rate.

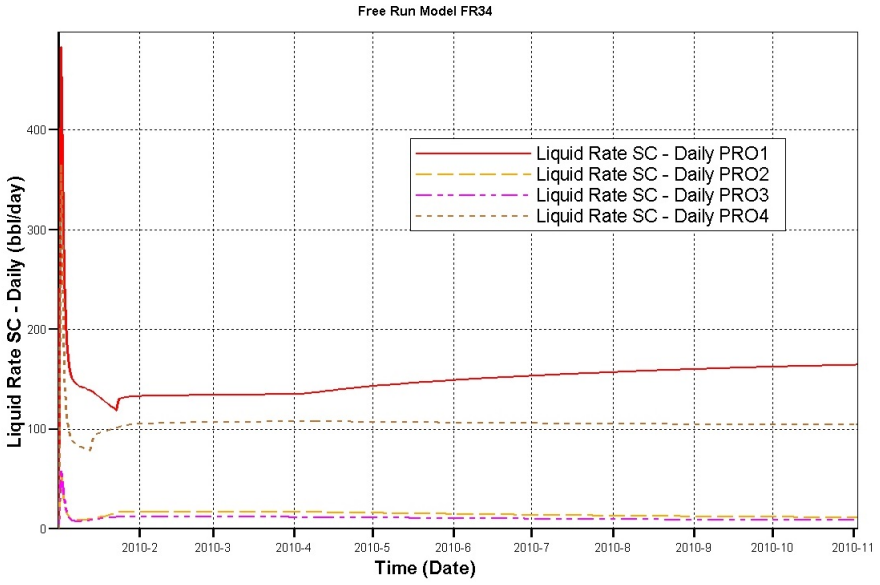

FIGURE 4.3: Daily liquid rate of each producer for model FR34, during the first year of reservoir lifecycle.

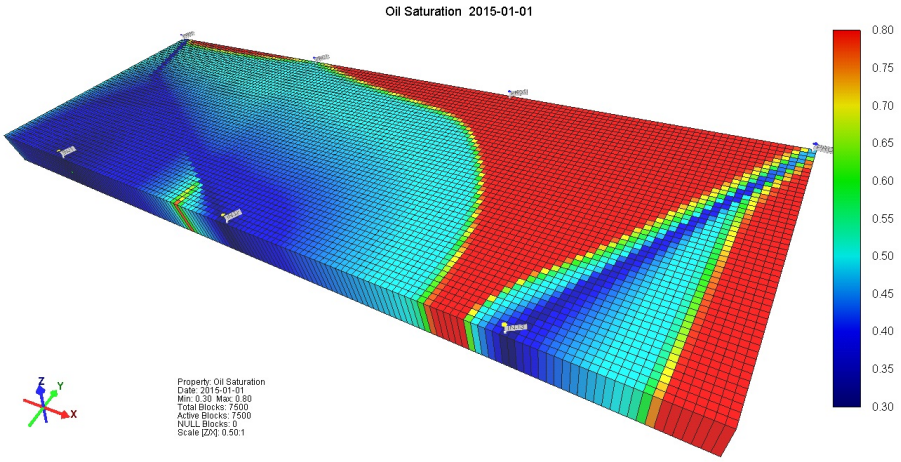

FIGURE 4.4: Oil saturation of the RF34 at the end of its lifecycle.

Note that although the simulations of step responses that are shown in these figures are very long, well test and step responses can be reasonably short in practice.

4.3.1 Transient Test Response

As mentioned in Table 4.1, most of the parameters of a persistently exciting and informative injection sequence can be determined with and aid of a well test. Figures 4.6, 4.7 and 4.8 show the response of the producers to the increase of the individual injection rate from 100 bbl/day to 500 bbl/day.

Shape: The step responses are very similar to each other with larger or smaller DC gain depending whether the producer is located in the fracture or matrix, and also the distance to the injector. The very simple shape of the response implies that the

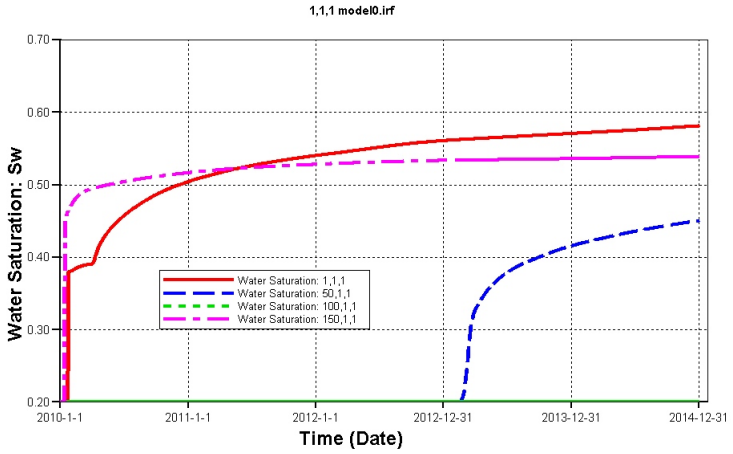

FIGURE 4.5: Water saturation S_w of the producers in FR34 during its lifecycle.

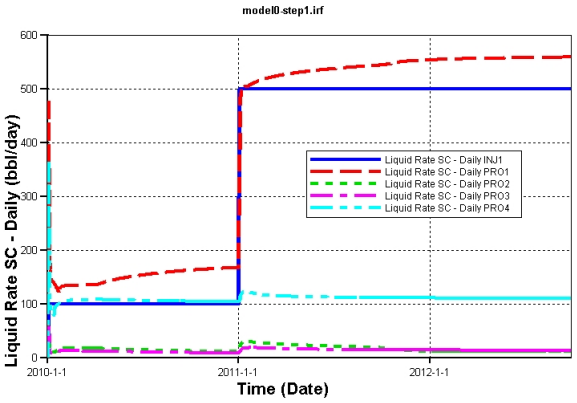

FIGURE 4.6: Step like increase in the injection rate INJ1 from 100 *bbl/day* to 500 *bbl/day* and produced liquid rate response on all producers.

underlying dynamics are simple. Since this test is done after the water break through of PRO1 and PRO4, saturation changes in the reservoir with time are very slow.

Fastness/Slowness: The declines in productivity are different for each producer, and thus their "settling shape" may look different; the responses of the producers in low permeability areas are constantly decreasing and have a pulse-like increase temporarily, while the producers in high permeability areas are non decreasing. In fact with less complex heterogenities, the pressure changes are the dominant source of change in production at this stage of the production. One should note that the presence of heterogenities can cause more complex shape and variation in settling time in the step responses. The fastest responses are settling to 95% of their steady state value between 3 to 12 days [2].

Response times that are greater than 10 days are insignificant as compared to others as the change they cause in production rate is about 2 – 3% of the step increase.

[2]Frequency is normalized t units of days for the whole experiment.

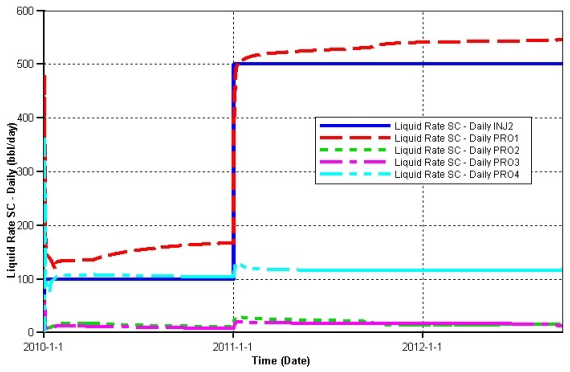

FIGURE 4.7: Step like increase in the injection rate INJ2 from 100 *bbl/day* to 500 *bbl/day* and produced liquid rate response on all producers.

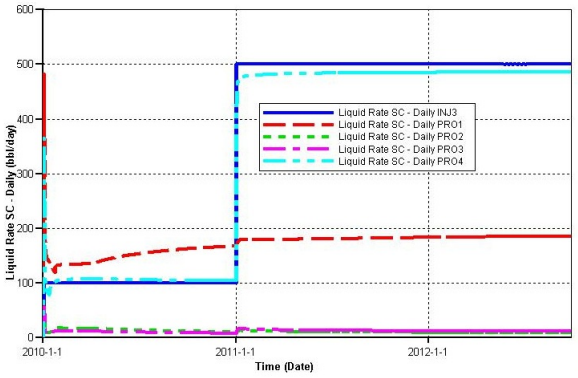

FIGURE 4.8: Step like increase in the injection rate INJ3 from 100 bbl/day to 500 bbl/day and produced liquid rate response on all producers.

Consequently one should expect a smaller interwell connectivity.

Sampling time: The lower bound of sampling time is determined based on the slowest time constant of the system, 14 days in this example. In PEI, numerically the smaller sampling time cause more fit for high frequency dynamics [39], and a fast sampled model is non-minphase with many nonmeaningful delays. With the rule of thumb $\Delta t \geq t_{set}/15$, and having the settling times of $3, 6, 12$, the determination of the lower band is a trade-off as a function of which well pair is more important, and thus requires a higher accuracy. According to Figures 4.6-4.8, the step response of PRO4 due to INJ3 is the most significant (as the production increases above 90% due increase in the injection) and thus these two wells are more closely related. The interwell connectivities of INJ1-PRO1 and INJ2-PRO1 are also very large but less than INJ3-PRO4. Therefore, the lower band can be determined as $\Delta t \geq 3/15 = 0.2\ day$.

In order to avoid aliasing or masking of the dynamics, the sampling time must be short enough as well. The upper bound is determined based on the fast dynamics of the system, which is again determined based on the most important input-output pair. Therefore, it can be easily chosen as $\Delta t \leq t_{set}/5 = 3/5 = 0.6$. Note that for the cases where the intersection of the two bounds is empty, the sampling time must be chosen based on the trade-off between the important wells, similar to what it has been done above.

(days)	INJ1	INJ2	INJ3
PRO1	**12**	**6**	+20
PRO2	+20	+20	+20
PRO3	+20	+20	+20
PRO4	+20	+15	**3**

TABLE 4.3: Settling time of the step responses from injectors to producers.

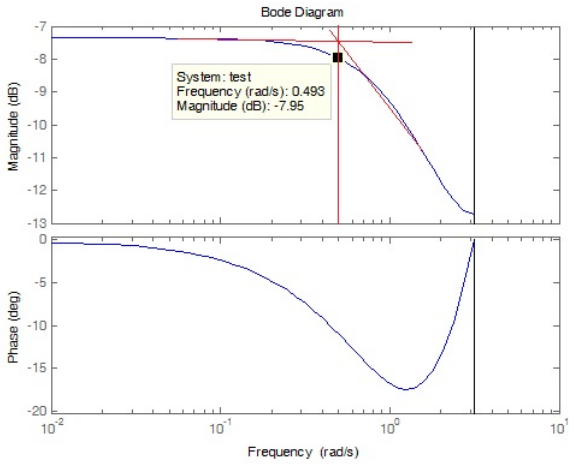

FIGURE 4.9: Frequency response (Bode plot) of a system with a single pole at 3 days settling time.

Length of the experiment: A length of $45-60$ is enough to reach 4 times of the settling time between INJ2-PRO4, the fourth most important pair in the table.

Frequency content: Figure 4.9 shows the frequency content of a first order LTI system with a single pole, that has a step response of 3 days settling time. This system has a sampling time of 1 day, and as it can be seen the pole is located around 15% of maximum normalized frequency. Assuming that the fastest pole of the reservoir is located around this frequency range, then the frequency content of the input signal should be more concentrated before the frequency of 20% of the sampling frequency.

4.3.2 Staircase Input Signal

A possible method that can indicate the level of nonlinearity includes the analysis of the system response to a staircase increasing or decreasing input signal. We have applied a staircase injection rate input increasing from 100 bbl/day to 1200 bbl/day. The responses after each increase are very similar, and an overall decline in production rate can be seen.

The amplitude of the injection sequence should also be high enough to avoid being masked by measurement/simulation noise. The two major pairs show strong connectivity, and are very sensitive to injection rates, see Figure 4.10 and 4.11. For example an increase/decrease of 25 bbl/day in injection rate of INJ2 is expected to increase/decrease the production rate of 22, 1, 0.5 and 0.5 bbl/day in producers respectively.

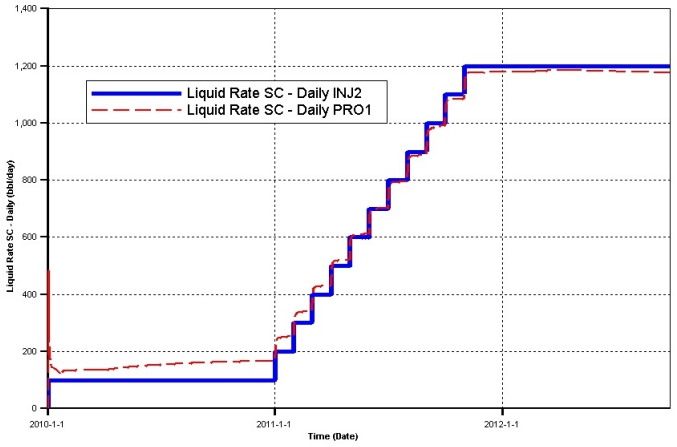

FIGURE 4.10: Response of PRO1 to staircase increase of injection rate in INJ2, 100 bbl/day increase.

Assuming the injectors have the capacity, and in order to see the effect of all injectors on all producers, we choose to design a sequence that goes from 100 bbl/day up to 200 bbl/day.

4.3.3 Prior Knowledge

The conclusions we had in previous two sub-sections are based on prior knowledge and preparatory experiments. Let us also look into this by considering a CM structure where the system pole is located at $\tau = \frac{c_t V}{J}$.

For the average saturation $S_w = 0.5$, $c_w = 3.1 \times 10^{-6}$, $c_o = 7 \times 10^{-6}$ at pressure above 2500 psi and $c_r = 10^{-6}$, then $c_t = 6 \times 10^{-6}$. The effective pore volume from an injector to its closest producer can be estimated roughly as $V = 100 \times 200 \times 50$, and is almost double

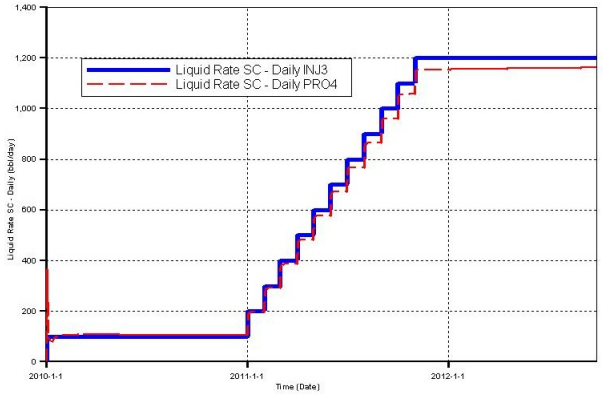

FIGURE 4.11: Response of PRO4 to staircase increase of injection rate in INJ3, 100 bbl/day increase.

this size for farther producers. Well productivity index J for injectors vary significantly depending on the presence of fracture or not and can be calculated by:

$$J = \frac{k_o h}{141.2 \mu_o B_o (\ln \frac{r_e}{r_w} - \frac{3}{4})} \tag{4.5}$$

For INJ3-PRO4 and INJ2-PRO1 which have faster dynamics $J \approx 20$ and for other pairs with slower dynamics it is 3 orders of magnitude smaller $J \approx 0.02$. Therefore, the τ would be $\tau \approx 0.415$ or $\tau \approx 415$ respectively, and the pole location of the CM will be at $e^{-1/\tau} \approx 0.09$ for fast dynamics, and $e^{-1/\tau} \approx 0.95$ for slow dynamics. Note that these values are only an estimate and not necessarily accurate for the whole reservoir.

4.4 Injection Scheduling

Given the required characteristics of the input signal, 3 sequences of RBS are generated as shown in Figure 4.12. All inputs have sampling frequency of $\Delta t = 0.5$ *day*, but the variations are designed so that no more than one change per day is allowed. The length of the experiment is 60 days.

Note that although there is a daily change in injection rate of all injectors, the frequency content of input signals do not necessarily contain such high frequency changes. Most of the energy of the signal is below $0.2 rad/sample$ where the dominant poles of the model are expected to be. This has been achieved by low pass filtering of the RBS signal as shown in Figure 4.13 for a similar signal but with 50 times longer length.

4.4.1 Uncorrelatedness of Injection Sequence in Multi-Injector

A necessary identifiability condition is that neither of the input signals are linearly dependent (100% correlated). Since all four producers are more or less affected by all the three injectors, in order to be able to distinguish the individual responses, the designed inputs must be uncorrelated. The smaller the length of the experiment, and the larger the number of injector, the harder the generation of uncorrelated signals. Figure 4.14 shows the cross correlation of the three injection schedule for ±10 samples lag or equivalently ±5 days.

The correlation for zero lag is very small for all three combinations. However, ideally all the correlations must be zero for any given lag.

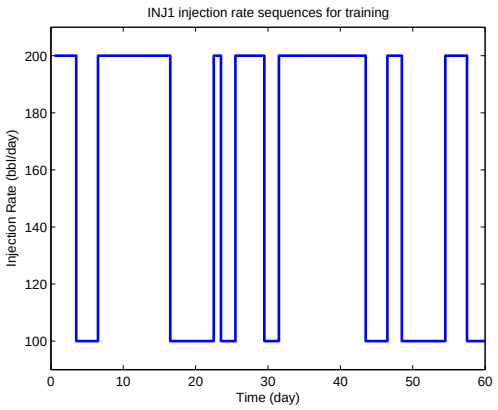

(A) INJ1

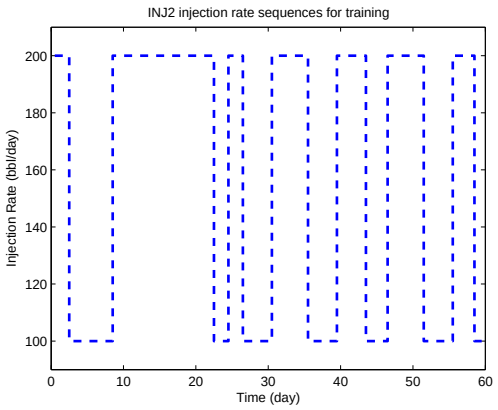

(B) INJ2

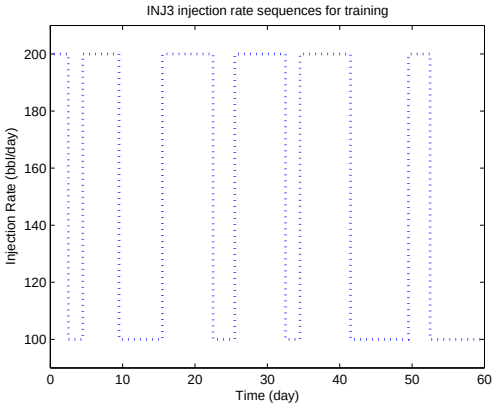

(C) INJ3

FIGURE 4.12: Designed injection rate schedule for training in reservoir model FR34.

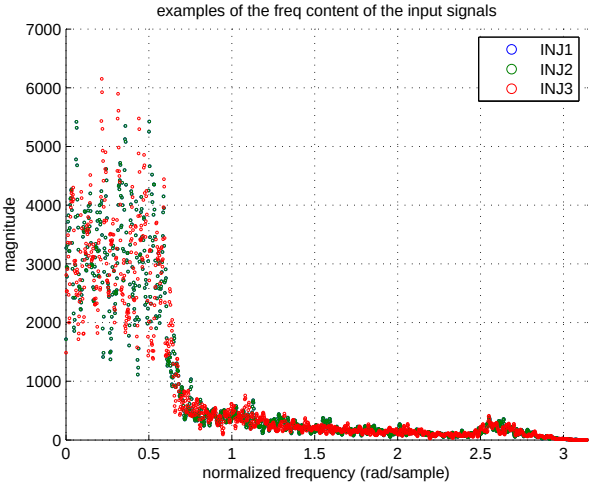

FIGURE 4.13: Frequency content of the designed input signals after filtering according to adjusted system pole location. The plot is drawn for three signals of the same characteristics with 50 times longer length to show the asymptotic behavior of the PRBS.

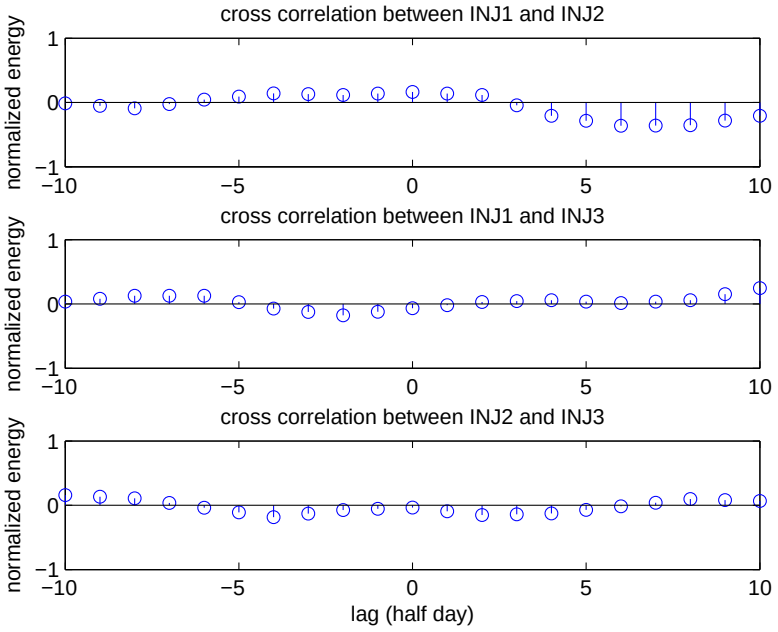

FIGURE 4.14: Cross correlation between the three injection schedule for ±5 days lag.

4.5 Model Identification and Validation

A single pole CM between each producer and injector is identified and the training and validation results that are calculated in Equation (3.11) are presented in Figure 4.15 and 4.16. Note that both input and output signals are detrended before identification.

One can see that training and validation fits are both high and similar, which implies a successful identification.

4.6 Conclusion

In this chapter, we have discussed the characteristics of an informative input signal and proposed a methodology to design an informative experiment using injection scheduling. Informative data is the one that excites all the relevant dynamical modes of the system within the range of the desired injection/production rate. We reviewed the parameter estimation from a mathematical point of view, and showed that the variance of the estimated parameters is reduced only if the input signal is persistently exciting. We suggested that a persistently exciting injection rate can be obtained by adding a sequence of predefined Random Binary Signals (RBS) to the reservoir's nominal injection rate. The overall produced oil is similar, while we have a training data that contains more information about the process.

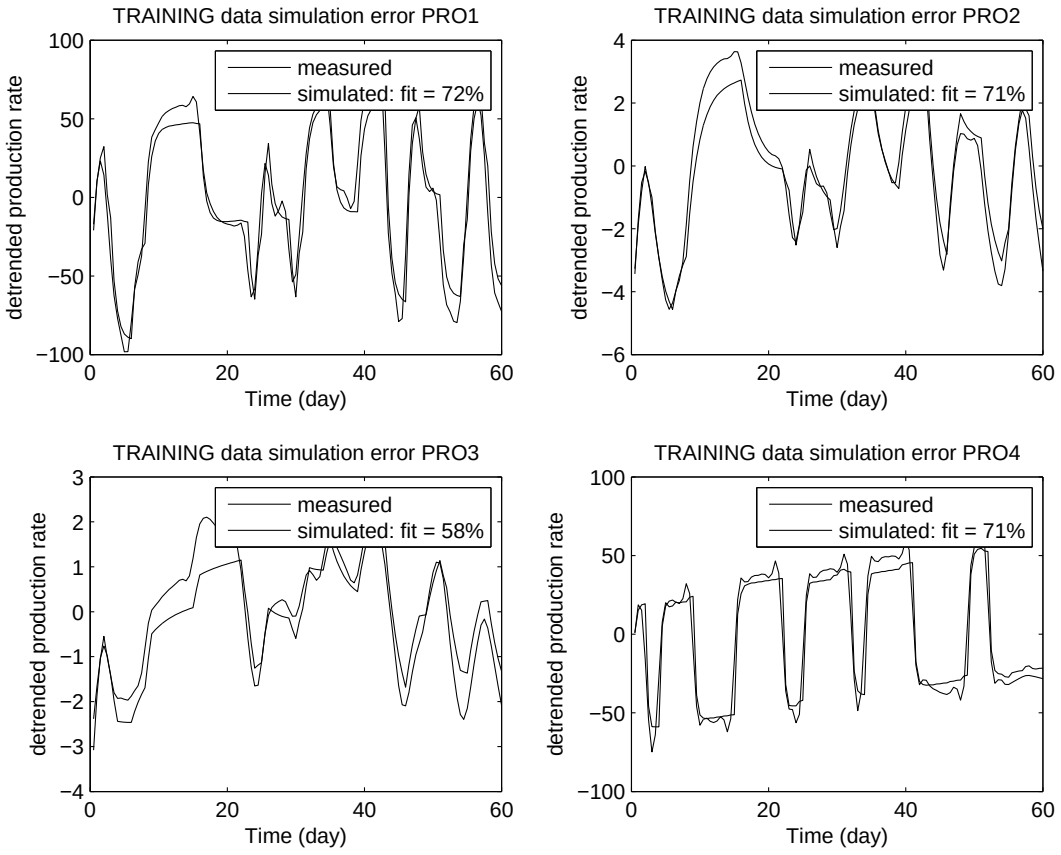

FIGURE 4.15: Training simulation fit for producers of the reservoir model FR34, identified with a CM.

Meanwhile, because a non-linear process is approximated by a linear low order model, care must be taken not to over-excite the system, which could make it drift from linear regime. The idea is to realize where the governing dynamics of the waterflood process lies and to identify the conditions under which the states are varying linearly, while the change in parameters is negligible. Naturally, pressure and saturation do not vary in a mature reservoir as much as they do in early life of the reservoir. That is the main reason why linear models can perform a lot better for later stages of production.

The methodology proposed here is basically about determining a number of characteristics (design parameters) of the injection scheduling: 1) Sampling Time, 2) Frequency of Variations, 3) Amplitude of Injection and 4) Experiment Length. Our methodology shows how to determine the design parameters step by step, based on the reservoir type and the production stage. We know that waterflooding is a constantly changing process, therefore prior information about the field can be used and most of the times a simple well test can also provide valuable information.

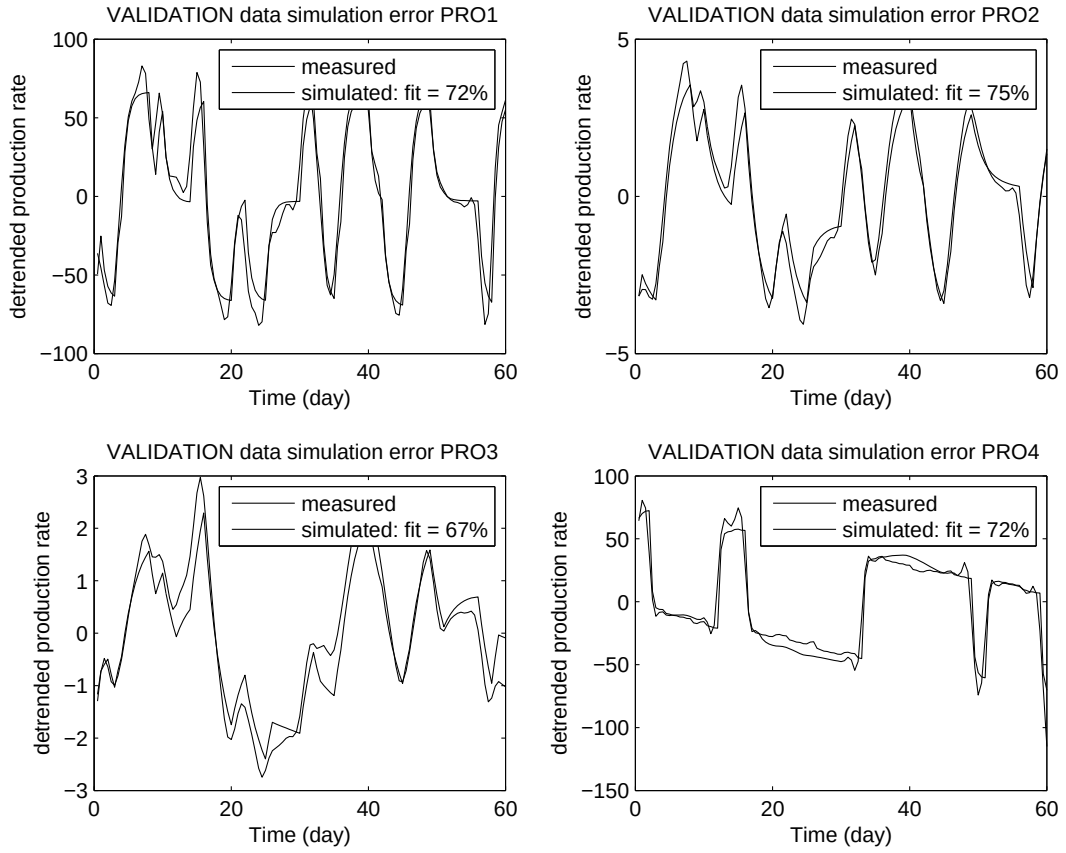

FIGURE 4.16: Validation simulation fit for producers of the reservoir model FR34, identified with a CM.

Chapter 5

Reservoir Model Upscaling Using Graph Wavelet

Over the past several decades considerable progress has been made in developing accurate techniques for measuring the properties of oil reservoirs. These properties include those obtained from field operations, such as pressure transients, well tests and well logs, and seismic studies. Such data, when combined with modern geostatistical techniques [44], have made it possible to generate highly-resolved computational grids for simulation of fluid flow and transport in oil reservoirs in which the porosity, permeability and other relevant properties are spatially distributed. The resolution of such computational grids depends on the amount of data that are available for various relevant length scales but, generally speaking, the grids typically contain a few hundreds of thousands of blocks or cells to a few millions of them, that represent the reservoir's Geological Model (GM). Numerical simulation of multiphase flows in the GM entails highly intensive computations, given that the governing equations are highly nonlinear and the simulations are usually run over a few years of actual lifetime of the reservoir [31, 45–47]. Since the main properties of a reservoir are usually known with some level of uncertainty, one must also generate at least a few realizations of the model of a reservoir, in order to obtain an estimate of the uncertainties in the computed properties. Such computations are not, however, feasible. It is, therefore, necessary to upscale the properties of the grid blocks of the GM in order to develop a coarsened grid that can be used in reservoir simulation with an affordable amount of computation time, while preserving the accuracy of the results.

Wavelet Transforms (WT) constitute a powerful tool for spectral and local analysis of data, such as time series and well logs, and have been used in the past for various problems in reservoir modeling. In particular, the WT has been used to upscale the

geological models of oil reservoirs. The application has, however, been limited to the models that are represented by regular computational grids with equal-size blocks or cells.

In this chapter we propose a generalization of the WT approach to upscaling by presenting a new model of a reservoir based on graph networks that makes it possible to use WT for constructing unstructured grids and upscaling them highly efficiently. We first define a computational grid representing a reservoir as a graph and its adjacency matrix, and then introduce the WT construction using the concept of lifting, utilized in classical signal processing and its extension to graph signal processing. The lifting-based graph WT is then described and its application to upscaling is developed. The result is an algorithm that can be applied to upscaling of any unstructured geological model represented by a computational grid in which the multiresolution WT is applied directly to the spatial distribution of the permeabilities. Examples in which the geological models are represented by the Voronoi teseellations are described, and simulation of waterflooding with such graph networks is carried out in order to demonstrate the efficiency of the new method.

5.1 Reservoir Upscaling Techniques

While upscaling methods for the single-phase (absolute) permeabilities of the grid blocks are now well-established, the same is not true about multiphase flows that involve, in addition to computing the equivalent absolute permeabilities of the upscaled blocks, adjustments to the flow of the fluid phases through the connected blocks of the upscaled grid. Many methods have been developed to accomplish this task, a review of which was given elsewhere [48] and, therefore, is not repeated here. In particular, [49] introduced a method whereby finer resolution is used in the regions of high fluid velocities, and upscaled homogenized description is utilized for the rest of the domain. No upscaling scheme was used for the relative permeabilities, as the original rock curves were used for the upscaled grid blocks, hence making the technique process-independent. Since the pressure field in the near-well regions usually changes rapidly in the radial direction, the early upscaling approaches were not suitable. Instead, well pseudo-functions were proposed [50, 51] to account for the pressure changes. [52] further developed their original method for calculating the transmissibility and well index for singlephase flow based on the solution to the local well-driven flow. Others developed upscaling methods that rely on either the spatial distribution of the permeability [53–55], or on the dynamic responses obtained by streamline simulation (see, for example, [49, 56–59].

We propose a new upscaling technique that can be applied to irregular grids using Graph Wavelet Transform (GWT), which represent an extension to irregular grids of the application of WT for upscaling. [27] proposed a triangulation method that is applicable to re-griding a coarse-scale model based on the location of the centroids of the upscaled blocks. Although the method results in an unstructured upscaled grid, the initial GM was still based on a computational grid with square blocks. The proposed approach lifts the restriction, and is applicable to any irregular grid. It will be described how to represent a computational grid and rock properties on a graph, and how to analyze graph "signals" such as the permeability, pressure, or saturation.

5.2 Gridding Schemes: Regular vs. Unstructured

Ideally, for evolutionary phenomena such as fluid flow in oil reservoirs, the computational grid should be dynamic so as to readjust itself as steep flow gradients propagate across the field [60]. If the computational grid is fixed in time, as is typical in almost all current simulators, then the best strategy for gridding is less obvious. One possibility is to adjust the grid block density according to the variations in the fine-scale permeability. Another strategy is based on the structure of the computational grid in the original GM. The grids that are in current use may be broadly classified into regular with equal-size blocks in the GM, and irregular and unstructured grids with unequal grid blocks. Due to the ease of implementation and their topological equivalence to the Cartesian coordinates, regular grids with square or cubic blocks are the most common. Critical reservoir features, such as faults, fractures, pinchouts, deviated and complex wells and highly correlated channels have, however, a high degree of geometric complexity, giving rise to highly-curved sectors. As a result, rigid and regular grid structure makes it difficult to simulate complex reservoir boundaries and heterogeneities, unless an impractically large number of grid blocks is used.

In this respect, nonuniform grids offer significant general applicability. Although identifying the optimal gridding scheme for a reservoir is simpler for regular grid blocks, unstructured grids represent an elegant and flexible description of the computational model. With irregular grids the ability to identify cells by a simple set of indices is lost, however, and the system of linearized equations generated by the unstructured grids is also somewhat more difficult to solve, due to the irregular structure of the matrix of the coefficients that arises in the iterative scheme for solving the equations. Flexible grids, such as those with triangular blocks, or unstructured tetrahedral grids to directly discretize 3D reservoirs, have been used in the past. [61] and [62] pioneered the use of the Voronoi grids for reservoir simulation. The Voronoi-type grids are very flexible

and may be used for generating hybrid structures, grids aligned with a reservoir's boundaries, and locally-refined blocks. However, the problem of upscaling such grids has remained unsolved.

5.3 Upscaling Using Wavelet Transform

The permeability distribution function $\mathbf{K}(x)$, which represents the permeability of each cell in space, can be expanded into wavelet functions of different dilations and positions to analyze the level of existing heterogeneities. Unlike Fourier Transform, WT can conveniently distinguish the location of the heterogeneities, which makes it a powerful tool for non-uniform upscaling of the blocks. Note that WT can be applied to other parameters of the dynamical equations such as relative permeability, porosity or even pressure and saturation, but here we review the method that is based on the permeability function.

Projection of $\mathbf{K}(x)$ onto wavelet functions gives "detail" and "scale" coefficient [1] for a given dilation and translation parameters a and b:

$$\mathcal{D}_{a,b} = \frac{1}{\sqrt{2^a}} \int_{-\infty}^{\infty} K(x)\psi(\frac{x}{2^a} - b)dx, \tag{5.1}$$

$$\mathcal{S}_{a,b} = \int_{-\infty}^{\infty} K(x)\phi_{a,b}(x)dx, \tag{5.2}$$

where $\phi(x)$ and $\psi(x)$ are quadrature mirror filters (QMF) also known as wavelet function, see [63]. Essentially, the "scale" and "detail" coefficients determine the low pass and high pass content of the function $\mathbf{K}(x)$. Based on the low-pass high-pass analysis, upscaling is done by keeping the fine grid in areas with large scale- and large detail-coefficients, and coarsening it for small detail-coefficient as follows; by defining a certain threshold for $\mathcal{S}$ and $\mathcal{D}$ in x, y and diagonal direction, every gridblock with corresponding coefficient below the threshold is combined with its neighbor in that direction. More levels of upscaling can be achieved by reapplying the same transform for the scale coefficients of the preserved cells/nodes. However, the permeability of the combined block is not known and an effective permeability must be calculated. To this end, one can use inverse wavelet transform while replacing the detail coefficient below threshold with zero as suggested by [27], or use a renormalization technique as in [64, 65].

[1] In Signal Processing community, scale coefficient is referred to as "approximation".

5.4 Graph Representation of Reservoir

Graphs provide a flexible and generic representation for any dataset, where data points may be interrelated in complex ways. Consider a 2D or 3D computational grid for a reservoir of any scale, where the grid blocks form a network of nodes that communicate with their neighbors, similar to the variables in numerical solution of partial differential equations. Every block has static properties, such as permeability and porosity, or geometry (which could be unique or similar to others), and dynamic properties, such as pressure and fluid saturation. Such a model of a reservoir may be viewed as a graph in which each block is represented by a node that is connected to its neighboring blocks with common edges. With such definition, any computational grid for a reservoir, whether it is regular or irregular, can be represented by a graph, which we refer to as the grid graph.

Every graph is defined by two sets of elements, $G = (\mathcal{V}, \mathcal{E})$, where $\mathcal{V}$ is the set of $\|\mathcal{V}\| = N$ number of vertices, and $\mathcal{E}$ is the set of edges e_{ij}. Every vertex v can be assigned a value, such as the permeability of the cell, and edges between two vertices v_i and v_j can be weighted by, for example, a characteristic of a certain feature, also known as the "connectivity". Examples of such weights include geometrical distance or some measure of similarity between the values of the two vertices. The initial fine-scale computational grid, or the GM, is then easily represented with the grid graph as follows: The centers of the blocks are the vertices, and each pair of neighboring blocks are connected with an edge e_{ij}. While the choice of the nodes and edges seems to be quite well defined, one has, in fact, considerable freedom on how to weight the edges. The weight can be very simple and trivial, such as an edge between neighboring nodes that is inversely weighted by the geometrical distance between the nodes. Alternatively, it may be more informative about the fluid flow, such as the "transmissibility" between the two cells. Note that each cell is considered to be homogeneous with a single set of parameters and states that are attributed to the cell's center.

Let us denote the grid graph that is weighted with the transmissibility by G_T, where $e_{ij} = T_{ij}$ and T_{ij} is defined as [66]:

$$T_{i,j} \triangleq \frac{\alpha_i \alpha_j}{\alpha_i + \alpha_j}, \quad \alpha_i = \frac{A k_i}{D_i} \vec{\mathbf{n}}_i . \vec{\mathbf{f}}_i, \tag{5.3}$$

with α_j defined in a manner similar to α_i. Here, A is the area of the interface between two adjacent blocks, k is the permeability of the cell, and D is the distance from the center of the block to the center of the interface, $\mathbf{n}$ is the normal vector of the interface, and $\mathbf{f}$ is the unit vector of the line that connects the center of the block to the center of

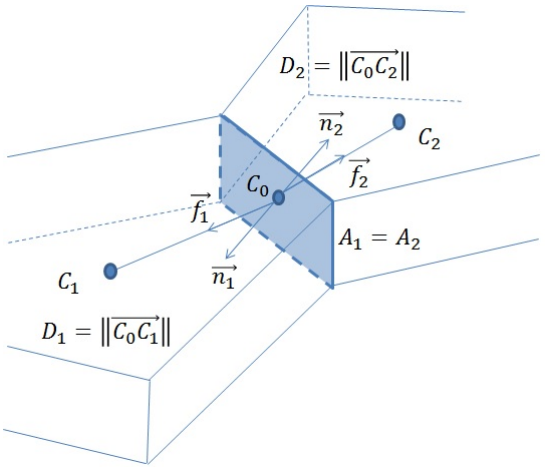

FIGURE 5.1: Geometrical representation of two adjacent control volume represented by two arbitrary gridblocks. This figure shows the parameters for calculating transmissibility T.

the interface; see Figure 5.1. Note that T_{ij} is calculated based on the fluid flow in the direction perpendicular to the interface and is a scalar.

Each graph can be uniquely defined with its adjacency matrix defined as $\mathbf{A}_{N\times N} = \{ a_{ij} \mid a_{ij} = 0 \text{ or } a_{ij} = e_{ij}, 1 \leq i, j \leq N\}$. Therefore, $e_{ij} = 0$ implies that the two vertices (or cells) v_i and v_j do not share an edge, i.e. the two cells are not neighbors; otherwise, they share an interface. If e_{ij} is calculated based on nonlinear time varying parameters or states of a reservoir, then the adjacency matrix can also be varying over time. Specifically, the dynamics of the three stages of production might be different substantially and therefore require separate graphs. Matrix $\mathbf{A}$ can be invariant if it is solely based on geometry or time invariant parameters such as permeability or transmissibility (which is only practically true for single phase flow).

5.4.1 Reservoir Graph Spectral Analysis

Spectral graph theory has historically focused on constructing, analyzing, and manipulating graphs, as opposed to signals on graphs [29]. In order to analyze the frequency content of a graph signal, notions such as frequency, shift, downsampling, etc. that are common in Fourier analysis of classic signal processing must be defined for graph spectral domain.

The Fourier transform on graphs is given by the eigenbasis of the graph Laplacian which is defined as $\mathcal{L} = \mathbf{D} - \mathbf{A}$, where degree matrix $\mathbf{D}$ is a diagonal matrix whose i^{th} diagonal element d_i is equal to the sum of the weights of all the edges incident to vertex i. The expansion of a graph signal $\mathbf{f}$ on eigenvectors of Laplacian $\mathbf{u}_l$ shows the "frequency" content of that signal, and smaller eigenvalues of Laplacian λ are associated with

smoother and slowly oscillating "frequencies", which larger eignevalues are associated with rapidly oscillating eigenvectors.

The notion of oscillation and frequency for transmissibility reservoir graph G_T can be explained as follows; for a group of local cells/nodes that are connected with larger weight, their permeability values are more similar if permeability is low frequency, and are less similar if permeability is high frequency signal.

Related to the notion of frequency, for any given graph signal $\mathbf{f}$, one can define "zero crossing" that is the number of "edges" that have opposite signs on their corresponding vertices. This quantity shows roughly an estimate of the frequency content of the signal that is represented on the graph. For example the zero crossing of a Laplacian eigenvector can be defined as a set of edges [29]:

$$\mathcal{Z}_G(\mathbf{u}_l) = \{e = (i, j) \in \mathcal{E} | \mathbf{u}_l(i)\mathbf{u}_l(j) < 0\}. \tag{5.4}$$

Total variation is another parameter that is related to number of zero crossings and is calculated as follows:

$$TV(\mathbf{u}_l) = \frac{||\mathbf{u}_l - \frac{1}{\lambda_{max}}\mathbf{A}\mathbf{u}_l||^2}{||\mathbf{u}_l||^2}, \tag{5.5}$$

where $\mathbf{A}\mathbf{u}_l$ is equivalent to one hop shift of the eigenvector on the graph. $TV(\mathbf{u}_l)$ increases with the frequency of $\mathbf{u}_l$.

5.5 Graph Signal Analysis

Graph signal $\mathbf{f} \in \mathbb{R}^N$ is defined as a value of each node, which can be represented as a vector of length N. It must be reminded that the definition of weighted adjacency matrix makes the location of nodes a conceptual notion and therefore, the index of the elements of graph vector is a mere label and does not imply any sequence. The choice of the graph signal depends on what needs to be analyzed and what kind of information needs to be inferred. For example if one wishes to use the information for upscaling based on permeability, then the value of each node is the permeability (assuming K is the same for all directions for isotropic rock). Pressure and saturation can also be used as graph signal.

5.5.1 Graph Signal Filtering

For a fixed graph structure with graph Fourier transform $\mathcal{L}$, graph signal filtering is defined as (re)shaping the signal in graph Fourier domain according to a given frequency response. Suppose a graph filter is denoted by $\mathbf{h} \in \mathbb{R}^N$, which has graph Fourier transform of $\hat{\mathbf{h}} \in \mathbb{R}^N$. For a given graph signal $\mathbf{f}_{in}$, the filtering operation in the frequency domain is defined as:

$$\hat{\mathbf{f}}_{out} = \hat{\mathbf{f}}_{in} .* \hat{\mathbf{h}} \tag{5.6}$$

where $\hat{\mathbf{f}}$ is the graph Fourier transform of $\mathbf{f}$ and $.*$ represents element by element multiplication, and $\hat{\mathbf{h}}$ is defined as

$$\hat{\mathbf{h}}(l) = \langle \mathbf{h}, \mathbf{u}_l \rangle = \sum_{i=1}^{N} \mathbf{h}(i)\mathbf{u}_l^*(i), \text{ for } l = 1, 2, \ldots, N \tag{5.7}$$

where $\mathbf{u}_l$ is the eigenvector in the basis of the graph Fourier transform. It should be noted that this filtering is applied in the frequency domain and therefore, $\hat{\mathbf{f}}_{out}$ must be transformed back into vertex domain.

Intuitively, the filtering operation is a modulation in frequency domain and as a result, depending on the shape of the filter $\hat{\mathbf{h}}$, certain frequencies of $\mathbf{f}$ are amplified or attenuated.

Let us look at an example; Assume a 2D permeability distribution of a reservoir with three fractures as presented in Figure 5.2(A). Figures 5.2(B)-(F) show the filtered permeability signal $\mathbf{K}$ based on graph G_T. A low pass filtering operation to preserve $\frac{n}{N}$ of the graph frequencies for permeability signal is given by:

$$\mathbf{K}_{out} = \mathbf{U} \begin{bmatrix} I_{n\times n} & 0 \\ 0 & 0 \end{bmatrix}_{N\times N} \mathbf{U}^T \mathbf{K}_{in}. \tag{5.8}$$

This filter only keeps the signal content that is a linear combination of first n eigenvectors corresponding to the n lowest frequencies and the rest is discarded. A similar high pass filtering can be defined by swapping the diagonal blocks is Equation (5.8). It can be seen in Figure 5.2 (B), (C) and (D) that the permeability has been smoothed out around fractures. In fact the permeabilities of the nodes that are connected with larger transmissibility become more alike. The high pass filter in (E) and (F) has the opposite effect and shows the sharp edges of the fractures.

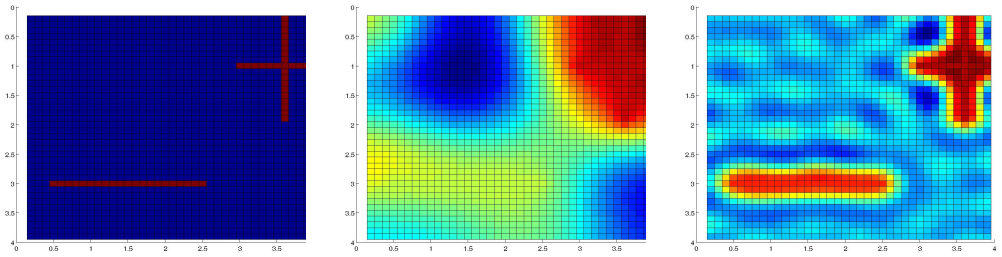

(A) Unfiltered permeability distribution. (B) LP Filtered with $n = \frac{1}{160}1600$ (C) LP Filtered with $n = \frac{1}{16}1600$

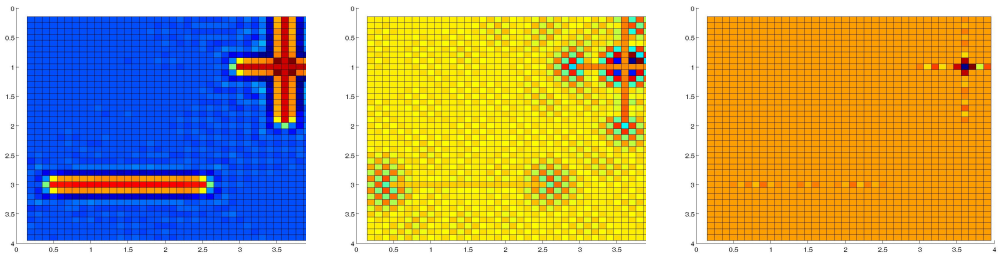

(D) LP Filtered with $n = \frac{1}{2}1600$ (E) HP Filtered with $n = \frac{1}{2}1600$ (F) HP Filtered with $n = \frac{1}{160}1600$

FIGURE 5.2: Filtering of permeability graph signal $\mathbf{K}$ based on transimissibility graph G_T of a fractured reservoir model. Filtering operation is given by Equation (5.8), for $N = 1600$.

Filtering can also be done in the vertex domain, where node values are filtered/updated as a linear combination of their K-hop neighbors, i.e., a localized linear transform. [29] shows that filtering in the vertex domain is related to filtering in the spectral domain as follows; when the frequency filter is an order K polynomial as $\hat{\mathbf{h}}(\lambda_l) = \sum_{k=0}^{K} a_k \lambda_l^k$ with constant coefficients a_k for all λ_l, the frequency filter signal at vertex i, $\mathbf{f}_{out}(i)$, is a linear combination of the components of the input signal at vertices within K-hop local neighborhood of vertex i. This is in fact analogous to filtering in classic signal processing using the shift operator z^{-1}.

The operation on permeability signal $\mathbf{K}$ in Equation (5.8) requires an order N (as many as the eigenvalues/nodes) polynomial and thus an N-hop linear transformation, i.e. a global smoothing of the permeability.

Figure 5.3 shows the vertex domain filtering based on the smoothing on 3-hop neighbors, using normalized Laplacian $\bar{\mathcal{L}}$, for low pass filter $\hat{\mathbf{h}}$ given by:

$$\hat{\mathbf{h}}(\lambda_l) = \sum_{k=0}^{3} \lambda_l^k. \tag{5.9}$$

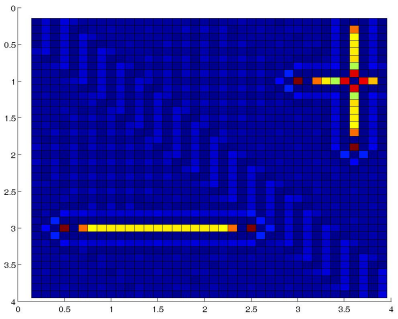

FIGURE 5.3: Low pass filtering in vertex domain using 3-hop neighbor averaging for permeability graph signal of a fractured reservoir model, and the filter is given by Equation (5.9).

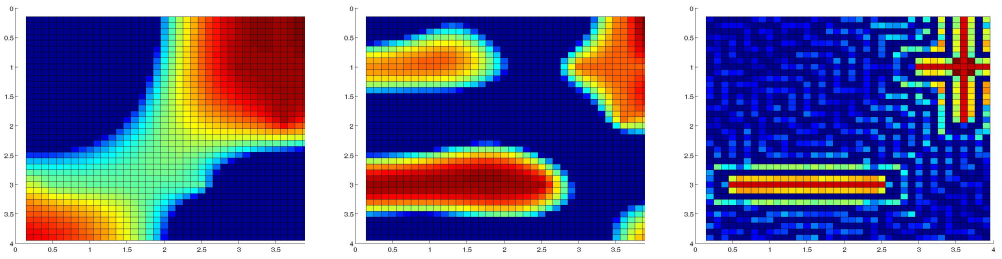

(A) $n = 4$ (B) $n = 16$ (C) $n = 800$

FIGURE 5.4: Filtering of permeability graph signal $\mathbf{K}$ based on transimissibility graph G_T of the fractured reservoir model with $N = 1600$ nodes, in spectral domain with a low pass filter given by Equation (5.10).

Figure 5.4 shows similar spectral domain filtering as in Figure 5.2, but the filter is chosen based on the eigenvalues of Laplacian $\mathcal{L}$ as:

$$\mathbf{K}_{out} = \mathbf{U} \begin{bmatrix} diag(\lambda)_{n\times n} & 0 \\ 0 & 0 \end{bmatrix}_{N\times N} \mathbf{U}^T \mathbf{K}_{in}, \tag{5.10}$$

where $diag(\lambda)_{n\times n} = diag(\lambda_1, \lambda_2, \ldots, \lambda_n)$.

Examples of low pass and high pass filtering are illustrated in Figures 5.3 and 5.4.

5.6 Lifting Based Wavelet Transform

Discrete Wavelet Transform (DWT) is based on Fourier Transform and is designed in frequency domain. In the early 1990's a so called *second generation wavelet transform* (SGWT) was introduced by [67], where the filters are not designed explicitly by translation and dilation, but are based on Lifting Scheme, which will be reviewed next.

The SGWT has a number of advantages over the classic wavelet transform in that it is quicker to compute (by a factor of 2) and it can be used for multiresolution analysis in either a structured or nonstructured grid graphs. Moreover, every lifting transform can be inverted perfectly and every perfect reconstruction filter bank can be decomposed into lifting steps and vice versa[2]. Another major advantage of lifting scheme is that convolution operation can be replaced by any nonlinear operation, and only the invertibility of the addition operation is relevant for perfect reconstruction.

5.6.1 Lifting Scheme

A generalized lifting scheme can be explained as follows; for a given signal $\mathbf{f}_0 \in \mathbb{R}^N$, one is interested in capturing the information in the signal in a lower dimension space, e.g., $\mathbf{f}_1 \in \mathbb{R}^{\frac{N}{2}}$. While the accuracy of the approximation in a lower subspace greatly depends on the type of the signal, it is desirable for the difference between $\mathbf{f}_0$ and $\mathbf{f}_1$ to be small. To this end, the first step is to split the signal into *even*, $\mathbf{f}_0^e$, and *odd*, $\mathbf{f}_0^o$, samples[3]. Assuming that one would like to keep the even samples, the next step is to *predict* the odd samples based on the even samples. Finally, the low frequency branch $\mathbf{f}_0^e$ is *updated* based on the energy/information removed by subsampling.

Figure 5.5 shows the block diagram of lifting scheme and its reconstruction. The above steps can be formally presented using matrix notation. By representing the lifting operations as a polyphase matrix $\mathbf{\Phi}_p(z)$, we have [68]:

$$\begin{bmatrix} \mathbf{f}_1^o \\ \mathbf{f}_1^e \end{bmatrix} = \begin{bmatrix} 1 & -\mathbf{P}(z) \\ \mathbf{U}(z) & 1 - \mathbf{U}(z)\mathbf{P}(z) \end{bmatrix} \begin{bmatrix} \mathbf{f}_0^o \\ \mathbf{f}_0^e \end{bmatrix} = \mathbf{\Phi}_p(z) \begin{bmatrix} \mathbf{f}_0^o \\ \mathbf{f}_0^e \end{bmatrix}, \tag{5.11}$$

where $\mathbf{P}(z)$ is the prediction and $\mathbf{U}(z)$ is the update operation. Note that $det(\mathbf{\Phi}_p(z)) = 1$ and therefore the inverse operation is

$$\mathbf{\Phi}_p(z)^{-1} = \begin{bmatrix} 1 - \mathbf{U}(z)\mathbf{P}(z) & \mathbf{P}(z) \\ -\mathbf{U}(z) & 1 \end{bmatrix}. \tag{5.12}$$

Note that $\mathbf{\Phi}_p(z)$ can also be factored into an upper and lower triangular matrix as:

[2]Note that although every reconstructable filter bank can be expressed in terms of lifting steps, a general description of the lifting steps is not obvious from a description of a wavelet family. However, for instance for simple cases of the Cohen-Daubechies-Feauveau wavelet, there is an explicit formula for their lifting steps.

[3]For a structured signal in classic signal processing, e.g. 1D audio signal or 2D image signal, this step is trivial and it boils down to subsampling the signal using a lazy wavelet filtering.

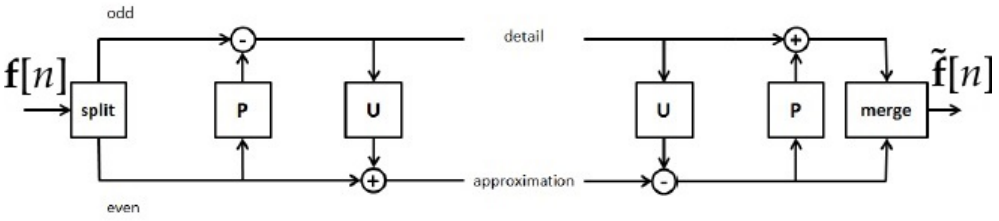

FIGURE 5.5: Block diagram of lifting scheme.

$$\mathbf{\Phi}_p(z) = \begin{bmatrix} 1 & -\mathbf{P}(z) \\ \mathbf{U}(z) & 1 - \mathbf{U}(z)\mathbf{P}(z) \end{bmatrix} = \begin{bmatrix} 1 & 0 \\ \mathbf{U}(z) & 1 \end{bmatrix} \begin{bmatrix} 1 & -\mathbf{P}(z) \\ 0 & 1 \end{bmatrix}, \tag{5.13}$$

where each of them represents a *lifting step*, and the whole operation can be inverted by changing the order of prediction and update. A *sequence* of lifting steps consists of alternating lifts as: first the low-pass is fixed and the high-pass is changed and then the high-pass is fixed and the low-pass is changed.

5.6.2 Lifting on Graph

Many multiscale transforms for signals on graphs require successively coarser versions of the original graph that preserve properties of the original graph such as the intrinsic geometric structure. To apply the lifting scheme on an arbitrary graph structure, one must have a solid definition of graph coarsening or downsampling, which as will be seen will involve a bipartition.

The graph downsampling problem is split into two steps: a) identifying the set of nodes to keep/remove, b) reconnecting the nodes in new graph. Authors have proposed various methods for these steps. [69] uses algebraic distance measure in a greedy seed selection algorithm to downsample the nodes. [70] minimizes the number of edges connecting two vertices in the same downsampled subset. Another generally applicable method which yields a natural downsampling on a graph is to partition the node set V into two subsets according to the polarity of the components of the graph Laplacian eigenvector $u_{\lambda_{max}}$ associated with the largest eigenvalue λ_{max} [71]. We will study this concept in more detail in the following section, but here we present the extension of lifting scheme on graphs for any given bipartition technique.

At scale j of transform, assume we have a bipartition method that divides the node set $\mathcal{V}_{j-1}$ into even set $\mathcal{U}_j$ and odd set $\mathcal{P}_j$. The values of the graph signal $\mathbf{f}_j$ for the samples belonging to odd set, i.e. $\{\mathbf{f}_j(m)|m \in \mathcal{P}_j\}$, are predicted from the samples belonging to even set $\{\mathbf{f}_j(n)|n \in \mathcal{U}_j\}$. Let us denote this set of coefficients with $d_{j,m}$. Then, the values

of the even samples are updated based on $d_{j,m}$, which we denote them by $s_{j,n}$. For the next level, same operation is repeated by replacing $\mathcal{V}_j = \mathcal{U}_j$. Note that this transform is invertible regardless of the bipartition technique.

For a graph $G = (\mathcal{V}, \mathcal{E})$ of size N nodes, with m odd and $N - m = l$ even labels, it is possible to rearrange the vertices with a proper permutation matrix to have:

$$\tilde{\mathcal{V}} = \begin{bmatrix} \mathcal{V}_{odd} \\ \mathcal{V}_{even} \end{bmatrix}, \quad \tilde{\mathbf{A}} = \begin{bmatrix} \mathbf{F}_{m\times m} & \mathbf{J}_{m\times l} \\ \mathbf{K}_{l\times m} & \mathbf{L}_{l\times l} \end{bmatrix}, \tag{5.14}$$

where $\tilde{\mathbf{A}}$ is the rearranged adjacency matrix. The submatrices $\mathbf{F}$ and $\mathbf{L}$ are now representing the adjacency matrix of the subgraph containing only odd and even nodes respectively. If the initial graph G is bipartite, these two matrices are trivially both zero, i.e. nodes of the same parity are not connected. See next section for more discussion about non-bipartite graphs.

For a given even-odd node assignment, the lifting wavelet transform to obtain coefficients s and d can be performed as follows:

$$\begin{aligned} \mathbf{D}_j^1 &= \mathbf{f}_j^{odd} - \mathbf{J}_P \mathbf{f}_j^{even} \\ \mathbf{S}_j^1 &= \mathbf{f}_j^{even} + \mathbf{K}_U \mathbf{D}_j^1 \end{aligned}, \tag{5.15}$$

where $\mathbf{J}_P$ and $\mathbf{K}_U$ are prediction and update matrix respectively that are obtained by proper weighting of submatrices $\mathbf{J}$ and $\mathbf{K}$ in Equation 5.14.

The inverse transform is also straightforward as follows:

$$\begin{aligned} \mathbf{f}_j^{even} &= \mathbf{S}_j^1 - \mathbf{K}_U \mathbf{D}_j^1 \\ \mathbf{f}_j^{odd} &= \mathbf{D}_j^1 + \mathbf{J}_P \mathbf{f}_j^{even} \end{aligned}. \tag{5.16}$$

Thus, in this implementation of lifting, first a weighted sum of even parity neighboring nodes is subtracted from the data on odd nodes to obtain detail coefficients. The values on even nodes are then updated by adding a weighted sum of detail values obtained in the previous step from their odd parity neighboring nodes.

5.7 Reservoir Upscaling Algorithm for Irregular Grid

As mentioned in the last section, the graph bipartition scheme directly influences the approximation of the coarsened graph signal that has a fewer number of nodes. Analyzing the distribution of the permeability represented by a graph signal using the LWT,

the idea is to determine a bipartition such that the detail coefficients D are all below a certain threshold. After identifying such a split (below and above the threshold), the even nodes are kept and odd nodes are removed. As a result, the volume (area in 2D) of the even nodes/cells that lose an odd neighbor must be increased to keep for the total reservoir volume (surface) constant. Since each node represents its cell's permeability and porosity, the equivalent permeability of the enlarged cell must also be calculated as well.

5.7.1 Bipartition Algorithm

A bipartite graph is a graph whose node set $\mathcal{V}$ can be divided into two disjoint sets, $\mathcal{V}_{even}$ and $\mathcal{V}_{odd}$, such that every edge in $\mathcal{E}$ only connects a node from $\mathcal{V}_{even}$ to $\mathcal{V}_{odd}$. In other words, the nodes of each set are not connected. Some graphs are inherently bipartite, like a tree graph or a grid graph with regular tiling. However, irregular and unstructured reservoir grid graphs are not necessarily bipartite but can be transformed into a bipartite graph by removing the edges that are connecting the nodes with similar parity. Partitioning $\mathcal{V}$ into two set of nodes very much depends on the application, e.g., a scheme that is suitable for traffic network graphs is not necessarily the best bipartition scheme for reservoir simulation.

We start by constructing the transmissibility graph G_T based on the GM. The first stage of the algorithm labels the nodes into even and odd, and removes the edges between the nodes of the same parity, such that the adjacency matrices $\mathbf{A}_{bp}$ of the bipartite graph and that of the initial graph $\mathbf{A}$, have minimum difference/conflict. First, the nodes are labeled odd or even randomly with a uniform distribution. Then, for a certain number of iterations (we typically used three times the number of the nodes) a randomly-selected node is activated and its parity is determined such that it minimizes the total edge loss. [70] showed that this method does converge and the partitioned graph is the closest bipartite graph to the initial graph.

The nodes corresponding to large detail coefficients, i.e., the high frequency nodes, are located in areas where the local cell permeability is less correlated. Since the even nodes are kept and the odd nodes are removed, such nodes must be labeled even. Otherwise, information at the locations with high flow velocity will be lost as a result of the coarsening. Therefore, in the second part of the algorithm, given the even and odd bipartition, the scale and detail coefficients are calculated based on adjacency matrix $\mathbf{A}_{bp}$, defined earlier, using Equation 5.15. If the detail coefficients corresponding to the odd nodes are larger than a certain threshold ϵ_D, then the node parity is changed to even. Our preliminary simulations indicated that repeating the procedure four or five times

and sweeping the graph captures all the nodes that are located in the high-frequency areas.

The threshold ϵ_D determines the trade-off between accuracy and number of coarsened or removed nodes. In our simulation, we chose ϵ_D based on a percent of the maximum normalized detail coefficients. We note that areas with high flow velocity may also be located around the injection or production wells. Naturally, to achieve a more accurate upscaling, the grid in such areas must be relatively resolved.

The algorithm is summarized as follows.

Algorithm 1 Graph Bipartition Algorithm

1: Calculate the grid graph weighted by transmissibility G_T
2: Calculate the adjacency matrix **A**
3: Randomly assign initial label (even or odd) to each node
4: **while** $k < k_{max}$ **do**
5: Activate a node randomly
6: Choose a parity that minimizes the total edge loss based on G_T
7: Inform the neighbors if parity changes
8: **end while**
9: **for** $n = 1 : 5$ **do**
10: Calculate the detail coefficient D_j for odd nodes
11: If $D_j > \epsilon_D$, assign node as *even*
12: **end for**

5.7.2 Calculating the Equivalent Permeability

After the graph is coarsened into one with fewer cells, it must be (re)discretized based on the location of the remaining nodes. Suppose that the original graph is embedded within a 2D rectangular area, bounded from all sides. Since the total area (volume in 3D) of the system should remain the same, the space is partitioned uniquely into the Voronoi polygons, given the spatial coordinates of the remaining nodes, which immediately yields the area (volume in 3D) of all the new blocks represented by their corresponding nodes.

We then compute the equivalent permeabilities of the coarsened (enlarged) blocks or cells. To do so, we use the effective-medium approximation (EMA) [72, 73]. The EMA is known to be accurate if the system is not near its connectivity threshold. According to the EMA, the equivalent permeability k of the new coarsened cell is the root of the following algebraic equation:

$$\sum_{i=1}^{n} \alpha_i \frac{k_i - k}{k_i + k} = 0 \tag{5.17}$$

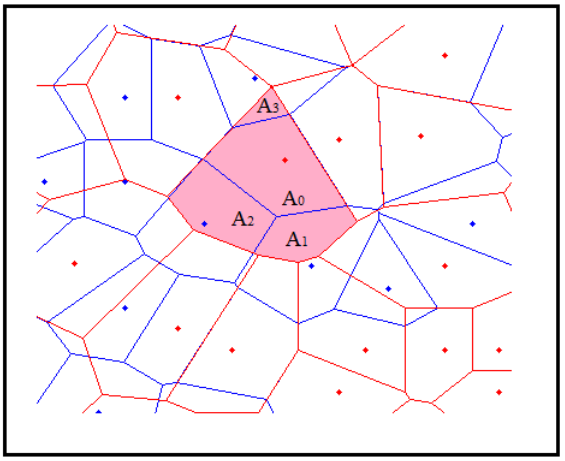

FIGURE 5.6: The areas of the cells or grid blocks increase during upscaling, and consist of the area of the cell from the initial graph (or the graph in the last coarsening level) and partial areas from the neighboring cells. Here we show an example of a cell v_0 with area A_0 that has been increased into $A_0 + A_1 + A_2 + A_3$ as a resulting of coarsening and merging of some of the cells.

where $\alpha_i = \frac{A_i}{A}$. A_0 is the area of the cell in initial graph and k_0 is its permeability. A_i , $i \geq 1$ is the partial area of the neighboring cell i that has been removed (added to the coarsened cell), k_i is its permeability, and A is the total area of the new cell in the coarsened graph. Thus, α_i represents the fraction of cell i contributing to the overall coarsened cell. The polynomial Equation 5.17 might have more than one root, but the real root that lies between the geometric and harmonic means of the permeabilities k_i is selected. If not, the geometric or harmonic mean that is closer to a real root is chosen for equivalent permeability.

The partial areas A_i can be calculated accurately. Note that it is inherent to the Voronoi tessellation that the area of the new (larger) cell consists of the area of the old (small) cell plus some parts of the areas of the cells around it that have been pruned in the graph upscaling. For example, see Figure 5.6, the polygon that creates partial area A_1 is made up of the corners of the common face that it has had with A_0 and the common corners of the polygons that used to be the neighbors of A_1.

5.8 Experimental Results

To test the proposed upscaling algorithm, we carried out a waterflooding simulation. A 2D GM model of size 512×512 was utilized that contained over 262,000 Voronoi cells. The cells' permeabilities were distributed according to a fractional Browning motion (FBM) with a Hurst exponent of $H = 0.3$, resulting in a permeability distribution that varies over nearly four orders of magnitude, between $75mD$ and $49,950$ mD. Isotropy

Reservoir Dimension (ft)	$256 \times 256 \times 50$
Approximate Initial Block Size(ft)	$0.5 \times 0.5 \times 50$
Depth (ft)	2000
Initial Oil Saturation (%)	100
Porosity (%)	30
Rock Compressibility (1/psi)	$1e-6$
Temperature (°F)	530
Oil Density (STD) (lb/ft^3)	56.388
Initial Reservoir Pressure (psi)	3000

TABLE 5.1: Rock and Fluid Properties of Reservoir Model SPE10.

was assumed, although it poses no difficulty to generate a stratified model of a reservoir, or assume distributed directional permeabilities. One injection point was inserted at one corner, and a producer at the opposite. The properties of the oil and the rock, presented in Table 5.1, and the expressions for the saturation-dependent relative permeabilities and capillary pressure were taken from the standard SPE-10 model [74].

The input to our proposed algorithm is a $N \times 3$ matrix in which the first two columns represent the Cartesian coordinates of the cells' centers, and the third column represents their permeability. It then generates the corresponding grid graph. We utilized Stanford University's General-Purpose Research Simulator [4] due to its compatibility with unstructured grid. Water is injected at constant BHP of $2,500 psi$ and the water break through happens after 51.5 days, when the water production rate of the producer passes $0.01 bbl/day$.

A snapshot of coarsened grid is presented in Figure 5.7, and Figure 5.8 shows how the number of nodes (blocks) is reduced each time the grid graph is swept. Because the permeability distribution is broad, the first few sweeps, or iterations, reduce the number of the cells drastically. After about five iterations, however, more than 80% of the original cells have been coarsened, and the decline in the number of the cells slows down. Thus, in terms of computing time, one must decide whether it is still efficient to continue sweeping the grid graph in order to reduce the number of the cells by a larger number. As Figure 5.8 indicates, after fifteen iterations the number of the cells has been reduced to $7,507$ and 992 for the two thresholds ϵ_D, respectively.

Figure 5.9 shows the normalized errors for the calculated water breakthrough times of the upscaled models compared to the water break through time in the initial GM of the reservoir, with two thresholds ϵ_D. One can see that the error is still less than 2% after more than 85% of the nodes have been removed.

[4] https://earth.stanford.edu/researchgroups/suprib/ research/research-areas/gprs

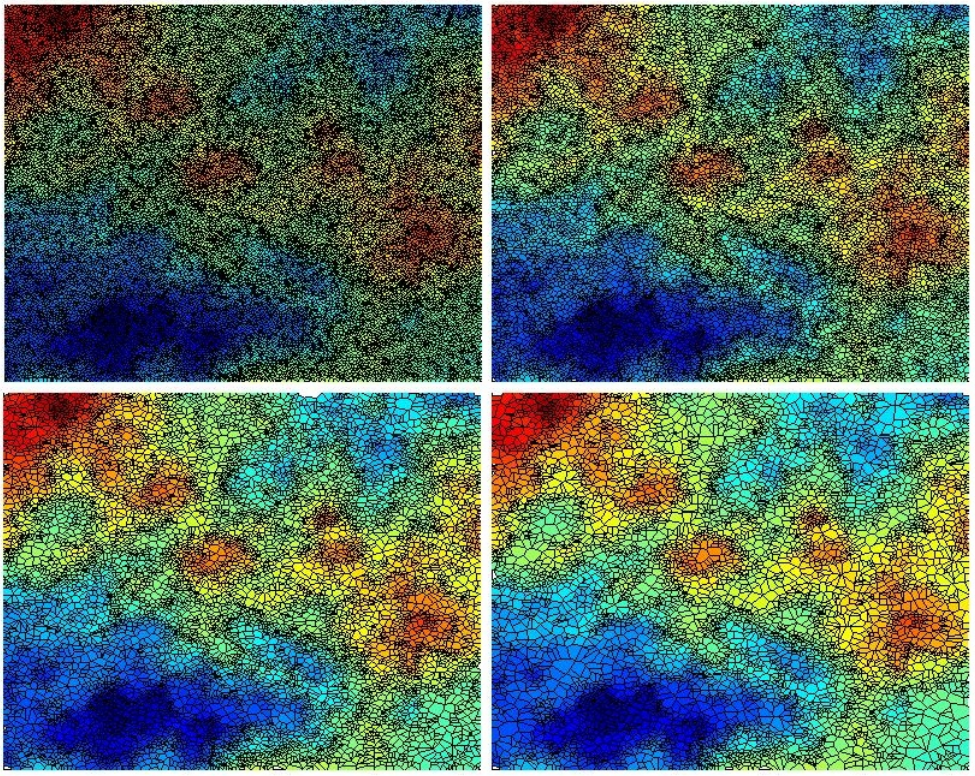

FIGURE 5.7: Snapshots of grid coarsening using graph wavelet transform.

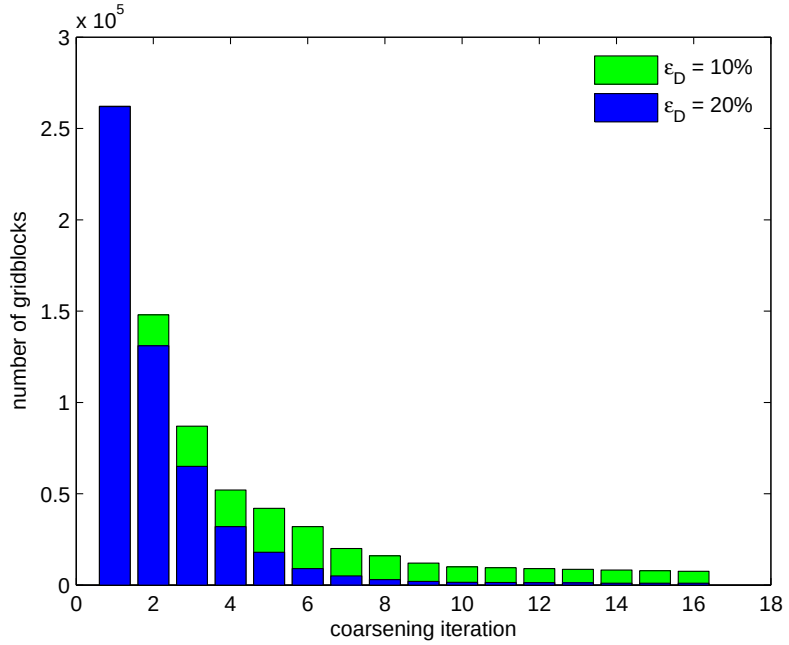

FIGURE 5.8: Reducing the number of cells by iterating the upscaling algorithm for two thresholds ϵ_D.

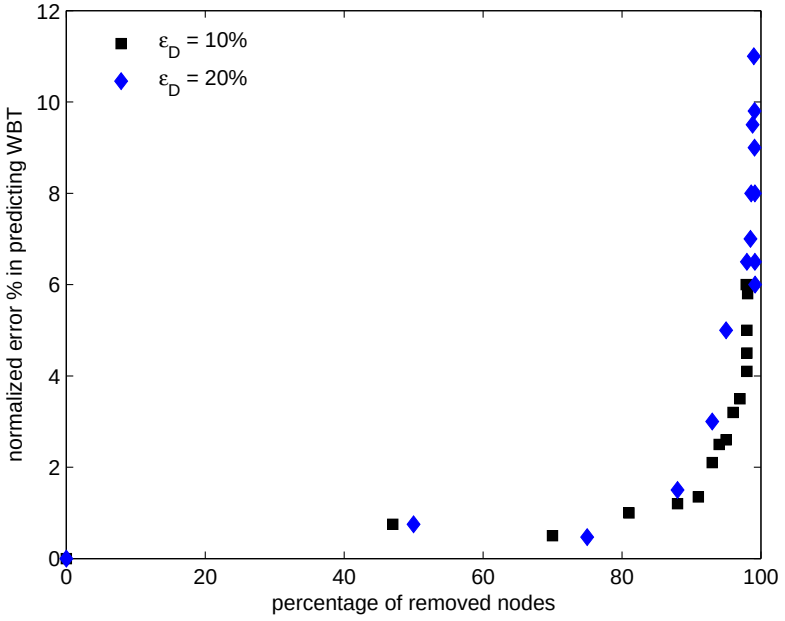

FIGURE 5.9: Percentage errors in predicting the water breakthrough time (WBT) by the upscaled models for two thresholds.

Next, we compare the estimated errors for the total oil production after 200 days, relative to that in the reservoir's GM, calculated with the upscaled models with two thresholds. The results are shown in Figure 5.10. The error is about 0.1% after more than 85% of the cells have been merged to form larger upscaled blocks. Note that the results are not very sensitive to the threshold ϵ_D.

The average pressure of a reservoir is another important quantity to study. Figure 5.11 compares the estimated errors for the average reservoir pressure, at various times, relative to corresponding pressure in the reservoir's GM at the same time, calculated with the upscaled model with two thresholds ϵ_D. The errors with $\epsilon_D = 10\%$ are completely negligible, while those with $\epsilon_D = 20\%$ are small, indicating the accuracy of the upscaling method.

Figure 5.12 presents the computation times at various levels of coarsening. The fine-scale model, or the GM, contained 262,144 cells, and it took 14,813 CPU seconds to complete the waterflooding simulation. After only one level of coarsening, the computation time was reduced by about 55%. After 5 levels of coarsening the computation time was reduced by a factor of 100, and when the coarsening stopped, the graph grid contained about 1000 cells and it took only 23 CPU seconds to complete the simulations. Thus, the proposed method achieves two principal goals of any upscaling method: high accuracy and high efficiency of its required computations.

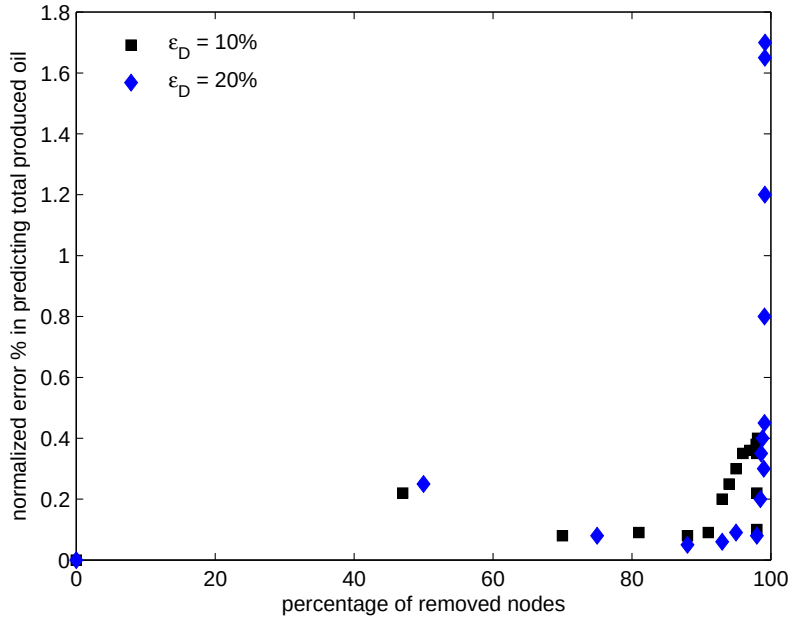

FIGURE 5.10: Percentage errors in predicting the total produced oil by the upscaled models for two thresholds.

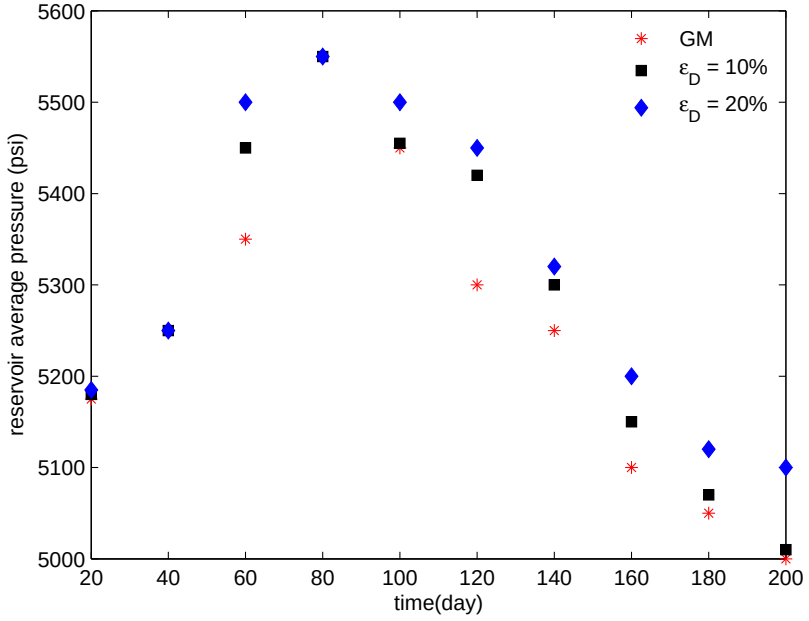

FIGURE 5.11: Comparison of the average reservoir pressure in the upscaled model with their corresponding values in the geological model (GM) of the reservoir.

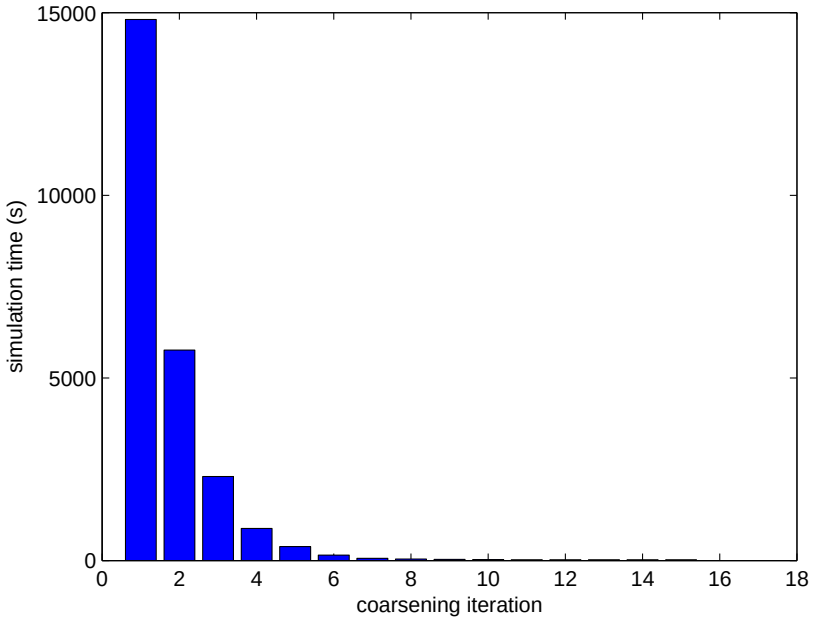

FIGURE 5.12: Simulation times (in CPU seconds) of the upscaled models with various iterations (levels) of coarsening.

5.9 Conclusion

A new method was proposed for upscaling of the geological models of oil reservoirs that are represented by completely irregular grid. The method is based on representation of a reservoir on graph networks, which makes it possible to use the wavelet transformations for constructing highly efficient unstructured grids and upscaling them. A computational grid representing a reservoir is defined as a graph and its adjacency matrix is set up. Then, the WT construction was introduced using the concept of lifting, used in classical signal processing and its extension to graph signal processing. The lifting-based graph WT is then described and its application to upscaling was developed. The result is an algorithm that can be applied to upscaling of any unstructured computational grid in which the multiresolution WT is applied directly to the spatial distribution of the permeabilities. Examples in which the geological model are represented by the Voronoi tessellations were described, and simulation of waterflooding with such graph networks were carried out in order to demonstrate the utility and efficiency of the new method.

Irregular grids are the ideal models for fractured reservoirs, as they allow the inclusion of fractures distribted in space at random or correlated orientations. Accurate and efficient upscaling of the geological models of fractured reservoirs in which the fractures are distributed in space according to a given orientation distribution and their length also follows a statistical distribution, is still an unsolved problem. The proposed upscaling

method based on representing the geological model by an irregular grid, can be used to address the problem.

Chapter 6

Conclusion and Future Work

As the outlook of the world energy consumption suggests, demand for hydrocarbon is rising constantly in the future. With 70% of the oil production coming from fields that are very old, the optimal management of a reservoir to maximize the recovery factor is becoming more important. Oil production can be improved not only by using modern equipment, but also by production optimization algorithms that are based on mathematical models. Advances in software technology is becoming as important as advances in hardware technology if not more. It is not just the efficiency in the computation anymore, as machine learning algorithms are redefining the world around us.

This study has two contributions in "experiment design for low order waterflood modeling" and "reservoir upscaling using graph wavelet transform". Although there is no direct connection between the two, in the bigger picture both lie under fluid flow modeling in porous media. Therefore, mass and momentum conservation principles were studied in Chapter 2. Although advanced reservoir simulators are capable of accurate flow modeling using numerical solvers, it is still possible to reduce the computational burden by upscaling the size of the reservoir grid. Alternatively, the injector-producer relationship can be approximated with a Linear Time Invariant (LTI) model. The idea is to use historical injection and production data, to estimate the parameters of a model, one that is able to predict the production rate for a given injection rate time series.

It was shown how the two states of the waterflood process, pressure and saturation, are coupled and are interacting nonlinearly. Reservoir rock and fluid properties are time varying and state dependent, which makes this interaction more complex. However, under mild assumptions the process can be approximated linearly over the periods of time. In order to accurately identify an LTI model between injectors and producers, the following assumptions must be met; a) neglecting the gas phase, b) negleting

gravity and capillary forces compared to pressure, c) negligible dependency of viscosity and permeability on pressure, d) neglecting compressible rock and fluid, e) bounded pressure around injectors, and f) low level of heterogeneity. Relative permeability K_r is a major source of nonlinearity that can greatly influence dynamical properties of the process and the amount of produced fluid. Even for changes that happen as slowly as in the order of weeks, the nonlinearities are so large that the LTI model must be updated as a result of changes in dynamics. Perhaps this is the main reason for undermodeling and underperforming of modeling approaches such as Capacitance Model (CM), Finite Impulse Response (FIR), AutoRegressive eXogenous (ARX) and Subspace models. In most oil fields, when producers start producing oil and water, i.e., when the reservoir is mature, these conditions are met.

For unstructured upscaling, it is important to have finer grid in areas where fluid has larger velocity, because it determines the flow direction and eventually the amount of produced oil. Neglecting gravity and capillary forces in the pores, the major driving force in the rock is the pressure gradient ∇P and mainly in the places with large permeability K. Areas near wells also have large ∇P, and permeability is very high near fractures.

Chapter 3 - In this chapter the statistical properties of parameter estimation is reviewed, and showed that the variance of the estimated parameters is reduced only if the input signal is "persistently exciting". It is suggested that a persistently exciting injection rate can be obtained by adding a sequence of predefined Random Binary Signal (RBS) on the reservoir's nominal injection rate. Adding such variations does not affect the total produced oil, and the obtained training data contains more information about the dynamical modes of the waterflooding process. We have investigated the effects of adding more variations with larger amplitude to a constant injection rate on the training and the validation of identified models. It can be concluded based on the results that it is not trivial to determine those variations, since adding larger and faster variations cause a more nonlinear behavior, and hence identified models will suffer from undermodeling.

Future Work: This chapter can be further extended on looking at the length of the experiment and how it influences the validation results. Moreover, the case where the true LTI model does not belong to the selected model set, i.e. $\mathcal{S} \notin \mathcal{M}$, can be investigated in more details.

Chapter 4 - A methodology is proposed in Chapter 4 about how to determine these variations. The characteristics of a sufficiently informative training data consists of; a) sampling time, b) frequency of variations, c) amplitude, and d) length of the sequence. A detail study of how to determine these parameters based on reservoir properties is

presented. A major source of information is history production data and well testing. The shape of the response of each producer to the increase in injection rate, and how fast this response settles, can be translated into a persistently exciting injection sequence, with variations that doesn't alter reservoir condition.

Future Work: This chapter can be extended by more simulation, and by more detailed investigation on the identified models, including topics such as model order sensitivity, and model predictability and prediction horizon. Ideally, one can show which parameters of the scheduled injection rate influence more on certain characteristics of the model.

Chapter 5 - In this chapter many successful upscaling methods such as upscaling using wavelet transform were reviewed, and it was discussed that they cannot be used for unstructured reservoir models. We showed how one can represent the reservoir grid on a graph and apply upscaling using graph wavelet transform. Since graph representation is very abstract, we demonstrate operations such as filtering and explain concepts such as frequency and downsampling by an example on how graph signal processing can be applied to analyze the graph signal that contains permeability values on the nodes.

Next, upscaling using graph signal processing is introduced, where we reviewed lifting based graph wavelet transform framework. What we propose is the multiresolution analysis of the permeability distribution on grid graph, where large permeability areas can be identified and located using graph wavelet transform. First, we introduced an algorithm to downsample reservoir graph, based on transmissibility, in order to reduce the number of cells. This algorithm partitions the cells into two groups: "even" nodes that represent the areas with large heterogeneity and high permeability, and "odd" nodes that represent the cells which pressure and saturation can be estimated from their neighbor even nodes. After removing the odd nodes, the reservoir is repartitioned using the location of even nodes as the centers of the Voronoi polygons to obtain a new unstructured grid. As a result, the volume (or area in 2D) of the cells will increase and their corresponding equivalent permeability is calculated based on effective medium approximation (EMA). A simulation example is presented that shows the effectiveness and efficiency of the proposed method.

Future Work: Further investigation is strongly suggested, such as comparison of our method with other upscaling techniques. While the accuracy and efficiency of various methods can be compared, one must note that our method has a fundamental advantage over other methods in that it can be used directly for any unstructured reservoir.

Appendix A

Relative Permeability

As was mentioned in Chapter 2, dependency of parameters to states of the system is a major source of the non-linearity. Permeability is a measure of ability of a porous medium to transmit fluid, and is addressed with field unit of *Darcy* or SI unit of m^2. Therefore, according to Darcy's law the fluid velocity (and also production rate) in a certain block is determined by permeability. In multi-phase flow through porous media the permeability to each phase is generally a nonlinear, path-dependent, function of the *phase saturation*. The gas, oil and water saturation, S_g, S_o and S_w, are defined as the fraction of the pore space occupied by the corresponding phase, such that, by definition, $S_g + S_o + S_w = 1$. In the case of three-phase gas-oil-water flow, Darcy's law is:

$$v_i = -k\frac{k_{ri}}{\mu_i}\nabla p_i, i \in \{g, o, w\}, \tag{A.1}$$

where k is the absolute permeability (also known as the homogeneous permeability) governed by rock properties only, while $0 < k_{rg} < 1$, $0 < k_{ro} < 1$ and $0 < k_{rw} < 1$ are the relative permeabilities which are nonlinear functions of the phase saturation and represent the reduction of permeability to one phase due to the presence of the other phases. The products $k_g = kk_{rg}$, $k_o = kk_{ro}$ and $k_w = kk_{rw}$ are known as the effective permeabilities to gas, oil and water respectively. More specifically there is a term called *mobility*, λ that is the quotient of viscosity and permeability, which plays a major role in movability of the fluid.

$$\lambda_i \triangleq \frac{kk_{ri}(S)}{\mu_i}, i \in \{g, o, w\}. \tag{A.2}$$

The physics of the relative permeability effect is related to the the interfacial tension between the phases (which gives rise to capillary pressure), the wettability of the rock, and the tortuosity of the pores [32]. Figure A.1 depicts a typical set of relative permeability curves for oil and water flow during the saturation of a block. After the formation of oil, it starts to migrate from bottom to the top and replaces the water that has already occupied the pore. At the end of this process some water will always be left in the pore space, known as *connate* water or *interstitial* water. The oil saturation process (called *imbibition* by production engineers) therefore starts from a situation with a water saturation S_{wc}, known as the connate water saturation. Because the water can not flow until the water saturation exceeds S_{wc}, it is also referred to as the *critical* water saturation or the *immobile* water saturation. At the end of the drainage process, a certain amount of oil remains trapped in the larger pores from which it cannot be displaced by water. This oil is known as residual oil, and the associated saturation S_{or} as the *residual* oil saturation. At the beginning and the end of the imbibition process, the presence of connate water and residual oil in the pores results in relative permeabilities below the theoretical maximum. These values, k^0_{row} and k^0_{rw}, are known as the *end-point relative permeabilities*. The subscripts *row* are used instead of *ro* to distinguish relative oil permeabilities in an oil-water system from those in an oil-gas system.

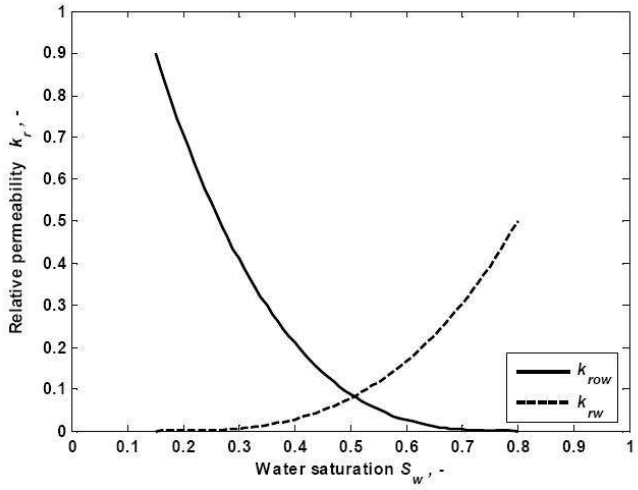

FIGURE A.1: Relative permeabilities to oil and water during imbibition (i.e. increasing water saturation)

Relations between saturation and permeabilities are often determined with laboratory experiments on core samples, called core flooding. In the absence of measured data, it may be necessary to revert to empirical relationships for the the relative permeabilities. For oil-water flow under imbibition conditions the relationship can be represented by

$$k_{row} = k^0_{row}(1 - S^*_w)^{n_{ow}}, k_{rw} = k^0_{rw}(S^*_w)^{n_w} \quad \text{with} S^* \triangleq \frac{S_w - S_{wc}}{1 - S_{or} - S_{wc}} \tag{A.3}$$

With n_{ow} and n_w are known as the Corey exponents. They are both larger than one with typical values between 2 and 4. Similar relations exist for gas-oil phase. In case of oil-water flow, the total relative permeability to liquid flow (the same for both phases) is given by $(k_r)_{ow} = k_{row} + k_{rw}$. In case of gas-oil flow the total relative permeability is given by $(k_r)_{go} = k_{rg} + k_{rog}$, and similarly, for three-phase flow $(k_r)_{gow} = k_{rg} + k_{ro} + k_{rw}$. To help illustrating the effect of relative permeability on production rates in the producer wells, refer to the section 3.4.3 of [32].

Appendix B

Discretization in Time and Space for Fluid Simulation in Porous Media

Because the reservoir properties are generally heterogeneous, the coupled PDE's cannot be solved analytically, and therefore the model must be discretized to be solved analytically. In this section we are presenting the basics of discretization, both in time and space, that represents the building blocks of reservoir simulation software packages. There are basically three discretization approaches in computational fluid dynamics; finite element (FE), finite difference (FD) and finite volume (FV)[75]. Here we focus on FV method because of its advantage of being independent of the grid shape. The advantage that makes FV the only possible method that can be applied for unstructured gridding. Please see [76] for more detail on FV derivation.

B.1 Spatial Discretization

Consider a 2D reservoir that has been discretized into several but finite number of grid blocks, each having a control volume Ω_i (see [19, 57, 77, 78]). For a given Ω_i, it is assumed that the physical properties of the reservoir and the fluid is averaged, and the total mass of each phase in the block can be obtained by integrating a similar mass conservation relation as Equations (2.1) and (2.2). A simplified form of it for single phase flow can be written as (note that saturation is no longer defined in single phase flow):

$$\int_{\Omega_i} (\nabla.(\rho v))dV + \int_{\Omega_i} (\frac{\partial}{\partial t}(\phi\rho))dV - \int_{\Omega_i} (\rho q)dV = 0, \tag{B.1}$$

where dV is the volume element. By using Darcy's relation for velocity, and under the assumption of low compressibility, one can obtain:

$$\sum_m \int_{\partial\Omega_{im}} (-\frac{1}{\mu}\vec{\mathbf{K}}.\nabla p).\vec{\mathbf{n}}_i dS + c_t \phi V_i \frac{\partial p}{\partial t} - q_i V_i = 0, \tag{B.2}$$

with dS representing surface element, $\vec{\mathbf{n}}_i$ unit outward normal vector on $\partial\Omega_{im}$, and $\partial\Omega_{im}$ being each of the m volumes that surrounds the control volume Ω_i. For a diagonal permeability tensor, the flux integral at each boundary can be approximated by a Two-Point Flux Approximation (TPFA) approach [79]: Between two gridblocks i and j, the flux in the boundary only depends on pressure (or more accurately the difference between the pressure) at the center of the cells and can be derived from the continuity of the pressure at the interface as:

$$q_{i-\frac{1}{2},j} = -T_{i-\frac{1}{2},j}(p_{i-1,j} - p_{i,j}), \tag{B.3}$$

where $T_{i-\frac{1}{2},j}$ is the transmissibility between two grid blocks defined as:

$$T_{i-\frac{1}{2},j} \triangleq \frac{1}{\mu} \frac{2k_{i-1,j}k_{i,j}}{\Delta x_i k_{i-1,j} + \Delta x_{i-1} k_{i,j}} \Delta y \Delta z. \tag{B.4}$$

By the analogy to the resistors in an electric circuit and according to the definition of the transmissibility, one can see that the equivalent resistance against the flux is in fact the distance weighted harmonic average of the x-component of the permeability tensor.

For two phase flow, T can be defined for each phase, while the geometric transmissibility is the same for all the phases and can be denoted by $T_{i,j}$ [66]. The concept of geometric transmissibility can be generalized for any arbitrary shape grid block and is defined as in Equation 5.3.

B.2 Time Discretization

The most common way to perform the discretization in time is to use first-order Euler scheme [80]. The pressure derivative term in Equation (B.2) can be replaced by:

$$\frac{\partial p(t)}{\partial t} = \frac{p_{n+1} - p_n}{\Delta t}, \tag{B.5}$$

where Δt is the discretization time step and $p_n = p(n\Delta t)$. The corresponding PDE is called explicit if all other terms are evaluated at time t as opposed to implicit if they are

defined at time $t + \Delta t$. The choice of Δt is not trivial as it can cause numerical instability or non-physical interpretation of the solution. More discussion on this can be found in Chapter 3.

B.3 Simulation

For a system of N grid blocks, the above equations can be solved for each block and for each time step for a given boundary condition. The simplest boundary condition is to assume no flow across all boundaries of the reservoir except for source and sink terms (the wells). Given that, one can assume the flow is controlled either by prescribing the flow (e.g. in the injector) or the bottom hole pressure (BHP), and numerically solve the equations. As a result, the pressure and saturation of each gridblock can be obtained for a given time.

Appendix C

Capacitance Model for Waterflooding

Based on the total mass balance for a given drainage pore volume, the so called Capacitance Model (CM) was introduced by [12]. For a single injector and single producer in the pore volume V_p the material balance can be written as:

$$c_t V_p \frac{d\bar{p}}{dt} = u(t) - y(t), \tag{C.1}$$

where $\bar{p}$ is the average pressure in the pore volume, or as some literature calls it reservoir pressure [32], and $u(t)$ and $y(t)$ are injection and production liquid rate. Pressure and rate in the well can also be related by an empirical well model as:

$$y(t) = J(\bar{p} - p_{wf}), \tag{C.2}$$

where p_{wf} is the flowing Bottom Hole Pressure (BHP) and J is the productivity index of the well, which is only valid for stabilized flow.

By eliminating the pressure from Equation (C.1) and (C.2), one can solve the ordinary differential equation and derive a time domain relationship between the injection rates (input) and production rate (output) as in:

$$\begin{aligned} y(t) =& y(t_0)e^{-(t-t_0)/\tau} + \frac{e^{-t/\tau}}{\tau}\int_{\xi=t_0}^{\xi=t} e^{\xi/\tau}u(\xi)d\xi + \\ & J\Big(p_{wf}(t_0)e^{-(t-t_0)/\tau} - p_{wf}(t) + \frac{e^{-t/\tau}}{\tau}\int_{\xi=t_0}^{\xi=t} e^{\xi/\tau}p_{wf}(\xi)d\xi\Big), \end{aligned} \tag{C.3}$$

where t_0 is the initial time, ξ is a variable of integration and τ is defined as $\tau \triangleq \frac{c_t V_p}{J}$. Equation (C.3) intuitively means that the production rate at a given time can be divided into three components [81], corresponding to the three terms in Equation (C.3). The first term is the response of the initial (pre-injection) production rate, or the cumulative produced fluid up to the time t_0. The second is the contribution from the input signal or injection rate. And the last term is caused by change of producer's BHP.

Equation (C.3) can be simplified by assuming the BHP remains constant and by setting the initial production to zero, thus first term becomes zero. Therefore, the discretized equivalent of Equation (C.3) can be derived as:

$$y[n] = \frac{\Delta t}{\tau} \sum_{m=0}^{n} e^{(m-n)/\tau} u[m]. \tag{C.4}$$

This equation simply implies that, for a production scenario that involves constant BHP, the output for a given moment can be computed from previous input values, with the knowledge of a single parameter τ (see [82] for varying BHP). This model can be represented in z-domain as:

$$Y(z) = \frac{\beta}{1 - \alpha z^{-1}} U(z), \tag{C.5}$$

where $\alpha \triangleq e^{-1/\tau}$ and $\beta \triangleq \Delta t/\tau$ [1]. As one can see, it has only one pole that determines the shape of the response and therefore is called a single pole transfer function in system identification literature, which is commonly used for representing simple LTI dynamics.

The generalization of CM for MIMO systems is straightforward by introducing a new parameter γ_{ij} called inter-well connectivity [37]. In this case, the transfer function $G_{ij}(z)$ according to Equation (2.15) becomes:

$$G_{ij}(z) = \gamma_{ij} \frac{\beta_{ij}}{1 - \alpha_{ij} z^{-1}}. \tag{C.6}$$

One should specifically note that, for each pair of such system, the parameter τ_{ij} defines the individual response from input i to output j, or in other words the measure of the dissipation of the pressure between injector i and producer j, and another parameterγ_{ij} determines the contribution of the same injector and that producer.

[1] For further discussion about Δt see Chapter 3, but for now assume that discretization time-step is normalized to 1.

Symbols

A	interface area
$\mathbf{A}$	state matrix, adjacency matrix
$\mathbf{B}$	input matrix
$c_{o,w,r,t}$	compressibility
D	distance
$\vec{\mathbf{f}}$	distance vector
$e[n]$	random iid noise
$f_{o,w}$	fractional flow
g	gravity acceleration
G	transfer function, Graph
h	depth
$H(z)$	disturbance model
J	well productivity index
$k_{ro,rw}$	relative permeability
$\vec{\mathbf{K}}$	permeability tensor
k	permeability
M	number of system inputs
$\tilde{\mathbf{n}}$	normal vector
N	length of data
N	number of nodes in graph
N	number of system outputs
o	index oil
p	pressure
p_c	capillary pressure
p_{wf}	well pressure BHP
$q_{o,w,t}$	flow
$S_{o,w}$	saturation
S	surface
t	index total

T	transmissibility
$\mathbf{u}$	input vector
U	input of a system
$\vec{v}_{o,w,t}$	phase velocity
V	volume
V_p	pore volume
w	index water
x	system state
x	Cartesian x-direction
$\mathbf{y}$	output vector
Y	output of a system
z	depth of the reservoir
z	z-transform operator

α	system pole
β	system DC gain
γ	interwell connectivity
δ	system parameter
Δt	time step
θ	parameter vector
$\lambda_{o,w,t}$	mobility
$\mathcal{L}$	graph Laplacian
$\mu_{o,w}$	viscosity
ϕ	porosity
$\rho_{o,w}$	density
Ω	control volume
τ	transfer function time constant

Bibliography

[1] G. van Essen, A. Rezapour, P. M. Van den Hof, and J. D. Jansen, "Integrated dynamic optimization and control in reservoir engineering using locally identified linear models," in 49th IEEE Conference on Decision and Control (CDC), pp. 7643–7648, IEEE, dec 2010.

[2] J. D. Jansen, O. H. Bosgra, and P. M. Van den Hof, "Model-based control of multiphase flow in subsurface oil reservoirs," Journal of Process Control, vol. 18, pp. 846–855, oct 2008.

[3] A. Rezapour, Improved Waterflooding Performance Using Model Predictive Control. Master thesis, Delft University of Technology, 2009.

[4] M. Zandvliet, M. Handels, G. van Essen, R. Brouwer, and J. D. Jansen, "Adjoint-Based Well-Placement Optimization Under Production Constraints" , SPE Journal, vol. 13, pp. 392 -399, dec 2008.

[5] M. Zandvliet, O. Bosgra, J. Jansen, P. Van den Hof, and J. Kraaijevanger, "Bang-bang control and singular arcs in reservoir flooding," Journal of Petroleum Science and Engineering, vol. 58, pp. 186 -200, aug 2007.

[6] G. van Essen, M. Zandvliet, P. Van den Hof, O. Bosgra, and J. D. Jansen, "Robust Waterflooding Optimization of Multiple Geological Scenarios," SPE Journal, vol. 14, pp. 202 -210, mar 2009.

[7] G. van Essen, P. Van den Hof, and J. D. Jansen, "Hierarchical Long-Term and Short-Term Production Optimization," SPE Journal, vol. 16, pp. 191 -199, mar 2011.

[8] M. Christie, "Upscaling for Reservoir Simulation," Journal of Petroleum Technology, vol. 48, pp. 1,004 -1,010, nov 1996.

[9] A. Castellini, Flow based grids for reservoir simulation. PhD thesis, Stanfurd University, 2001.

[10] B. Bundy and H. Hales, "A Streamline Reservoir Simulator With Dynamic Gridding," Journal of Canadian Petroleum Technology, vol. 47, mar 2008.

[11] J. F. M. Doren, R. Markovinović, and J. D. Jansen, "Reduced-order optimal control of water flooding using proper orthogonal decomposition," Computational Geosciences, vol. 10, pp. 137 -158, may 2006.

[12] A. Yousef, P. Gentil, J. Jensen, and L. Lake, "A Capacitance Model To Infer Interwell Connectivity From Production and Injection Rate Fluctuations," in Proceedings of SPE Annual Technical Conference and Exhibition, Society of Petroleum Engineers, oct 2005.

[13] F. Liu, J. M. Mendel, and A. M. Nejad, "Forecasting Injector / Producer Relationships From Production and Injection Rates Using an Extended Kalman Filter," SPE Journal, vol. 1, no. December, 2009.

[14] G. Naevdal, L. Johnsen, S. Aanonsen, and E. Vefring, "Reservoir Monitoring and Continuous Model Updating Using Ensemble Kalman Filter," SPE Journal, vol. 10, pp. 66 -74, mar 2005.

[15] R. Markovinovi and J. Jansen, "Subspace identification of low-order reservoir models," in XIV International Conference on Computational Methods in Water Resources, (Delft, The Netherlands), p. 8, 2002.

[16] K. H. Lee, A. Ortega, N. Jafroodi, and I. Ershaghi, "A Multivariate Autoregressive Model for Characterizing Producer-producer Relationships in Waterfloods from Injection/Production Rate Fluctuations," in Proceedings of SPE Western Regional Meeting, Society of Petroleum Engineers, may 2010.

[17] P. Renard and G. de Marsily, "Calculating equivalent permeability: a review," Advances in Water Resources, vol. 20, pp. 253 -278, oct 1997.

[18] Y. Guéguen, M. L. Ravalec, and L. Ricard, "Upscaling: Effective Medium Theory, Numerical Methods and the Fractal Dream," Pure and Applied Geophysics, vol. 163, pp. 1175 -1192, may 2006.

[19] S. A. Vakili-Ghahani, Control-Relevant Upscaling. Phd dissertation, Delft University of Technology, jun 2010.

[20] A. Saez, C. Otero, and I. Rusinek, "The effective homogeneous behavior of heterogeneous porous media," Transport in Porous Media, 1989.

[21] L. Durlofsky, "Coarse scale models of two phase flow in heterogeneous reservoirs: Volume averaged equations and their relationship to existing upscaling techniques," Computational Geosciences, 1998.

[22] J. Barker and S. Thibeau, "A Critical Review of the Use of Pseudorelative Permeabilities for Upscaling," SPE Reservoir Engineering, vol. 12, pp. 138 -143, may 1997.

[23] N. Darman, G. Pickup, and K. Sorbie, "A Comparison of Two-Phase Dynamic Upscaling Methods Based on Fluid Potentials," Computational Geosciences, vol. 6, pp. 5 -27, mar 2002.

[24] S. Ekrann and J. O. Aasen, "Steady-State Upscaling," Transport in Porous Media, vol. 41, pp. 245 -262, dec 2000.

[25] G. A. Virnovsky, H. A. Friis, and A. Lohne, "A Steady-State Upscaling Approach for Immiscible Two-Phase Flow," Transport in Porous Media, vol. 54, pp. 167 -192, feb 2004.

[26] M. G. Gerritsen and L. J. Durlofsky, "Modeling Fluid Flow in Oil Reservoirs," Annual Review of Fluid Mechanics, vol. 37, pp. 211 -238, jan 2005.

[27] M. Sahimi, R. Darvishi, M. Haghighi, and M. R. Rasaei, "Upscaled Unstructured Computational Grids for Efficient Simulation of Flow in Fractured Porous Media," Transport in Porous Media, vol. 83, pp. 195–218, dec 2009.

[28] M. Cardoso and L. Durlofsky, "Use of reduced-order modeling procedures for production optimization," SPE Journal, 2010.

[29] D. I. Shuman, S. K. Narang, P. Frossard, A. Ortega, and P. Vandergheynst, "The emerging field of signal processing on graphs: Extending high-dimensional data analysis to networks and other irregular domains," IEEE Signal Processing Magazine, vol. 30, pp. 83–98, may 2013.

[30] A. Sandryhaila and J. M. F. Moura, "Discrete Signal Processing on Graphs," IEEE Transactions on Signal Processing, vol. 61, pp. 1644–1656, apr 2013.

[31] K. Aziz and A. Settari, Petroleum reservoir simulation. Applied Science Publishers, 1979.

[32] J. D. Jansen, Systems Theory for Reservoir Management. No. November, Delft University of Technology, 2008.

[33] G. Chierici, "Economically improving oil recovery by advanced reservoir management," Journal of Petroleum Science and Engineering, 1992.

[34] T. Heijn, R. Markovinović, and J. D. Jansen, "Generation of Low-Order Reservoir Models Using System-Theoretical Concepts," SPE Journal, vol. 9, pp. 202–218, jun 2004.

[35] L. Ljung, System Identification: Theory for the User. Prentice Hall; 2 edition, 1999.

[36] T. Kailath, Linear Systems. Prentice-Hall, Inc., 1 ed., 1980.

[37] K. H. Lee, Investigating Statistical Modeling Approaches For Reservoir Characterization in Waterfloods From Rates Fluctuations. Phd dissertation, University of Southern California, 2010.

[38] K. H. Lee, I. Ershaghi, A. Ortega, and A. Ghareloo, "A Method for Characterization of Flow Units Between Injection-Production Wells Using Performance Data," in Proceedings of SPE Western Regional and Pacific Section AAPG Joint Meeting, Society of Petroleum Engineers, mar 2008.

[39] P. M. J. V. D. Hof, System Identification. No. January, Delft, The Netherlands: Delft University of Technology, 2006.

[40] P. Van Overschee and B. De Moore, Subspace Identification for Linear Systems: Theory - Implementation - Applications. Springer; 1 edition, 1996.

[41] R. Mehra, "Optimal input signals for parameter estimation in dynamic systems-Survey and new results," IEEE Transactions on Automatic Control, vol. 19, pp. 753–768, dec 1974.

[42] K. H. Lee, A. Ortega, A. Ghareloo, and I. Ershaghi, "An Active Method for Characterization of Flow Units Between Injection/Production Wells by Injection-Rate Design," SPE Reservoir Evaluation & Engineering, vol. 14, pp. 433–445, aug 2011.

[43] J. D. Jansen and P. K. Currie, Modelling and Optimisation of Oil and Gas Production Systems. No. April, Delft University of Technology, 2008.

[44] J. L. Jensen, Statistics for Petroleum Engineers and Geoscientists. Gulf Professional Publishing, 2000.

[45] D. Peaceman, Fundamentals of Numerical Reservoir Simulation. Elsevier, 2000.

[46] G. W. Thomas, Principles of hydrocarbon reservoir simulation. International Human Resources Development Corporation, 1982.

[47] M. Sahimi, Flow and Transport in Porous Media and Fractured Rock: From Classical Methods to Modern Approaches, vol. 0. John Wiley & Sons, 2011.

[48] M. Sahimi, M. Rasaei, F. Ebrahimi, and M. Haghighi, "Upscaling of Unstable Miscible Displacements and Multiphase Flows Using Multiresolution Wavelet Transformation," in SPE Reservoir Simulation Symposium, Society of Petroleum Engineers, apr 2013.

[49] L. J. Durlofsky, R. C. Jones, and W. J. Milliken, "A nonuniform coarsening approach for the scale-up of displacement processes in heterogeneous porous media," Advances in Water Resources, vol. 20, pp. 335–347, oct 1997.

[50] J. Chappelear and G. Hirasaki, "A Model of Oil-Water Coning for Two-Dimensional, Areal Reservoir Simulation," Society of Petroleum Engineers Journal, vol. 16, pp. 65–72, apr 2013.

[51] G. King, D. Snyder, T. Obut, and R. Perkins, "A Case Study of the Full-Field Simulation of a Reservoir Containing Bottomwater," in SPE Symposium on Reservoir Simulation, Society of Petroleum Engineers, apr 2013.

[52] L. Durlofsky, W. Milliken, and A. Bernath, "Scaleup in the Near-Well Region," SPE Journal, vol. 5, pp. 110–117, apr 2013.

[53] M. Garcia, A. G. Journel, and K. Aziz, "Automatic Grid Generation for Modeling Reservoir Heterogeneities," SPE Reservoir Engineering, vol. 7, pp. 278–284, apr 2013.

[54] D. Li and B. Beckner, "Optimal Uplayering for Scaleup of Multimillion-Cell Geologic Models," in SPE Annual Technical Conference and Exhibition, Society of Petroleum Engineers, apr 2013.

[55] R. Younis and J. Caers, "A method for static-based upgridding," Proc. of the 8th European Conference on the . . . , 2002.

[56] S. Verma and K. Aziz, "Two and three dimensional flexible grids for reservoir simulation - Google Search," in Proceedings of the Fifth European Conference on the Mathematics of Oil Recovery, (Leoben, Austria), 1996.

[57] M. G. Edwards and C. F. Rogers, "Finite volume discretization with imposed flux continuity for the general tensor pressure equation," Computational Geosciences, vol. 2, pp. 259–290, dec 1998.

[58] R. C. Portella and T. A. Hewett, "Upscaling, Gridding, and Simulation Using Streamtubes," in SPE Annual Technical Conference and Exhibition, Society of Petroleum Engineers, apr 2013.

[59] A. Castellini, M. Edwards, and L. Durlofsky, "Flow based modules for grid generation in two and three dimensions," 7th European Conference on . . . , 2000.

[60] M. G. Edwards, "A higher-order Godunov scheme coupled with dynamic local grid refinement for flow in a porous medium," Computer Methods in Applied Mechanics and Engineering, vol. 131, pp. 287–308, may 1996.

[61] Z. E. Heinemann and C. W. Brand, "Modeling reservoir geometry with irregular grids," SPE Reservoir Engineering, vol. 6, no. 2, pp. 225 – 232, 1991.

[62] C. L. Palagi, Generation and Application of Voronoi Grid to Model Flow in Heterogeneous Reservoirs. Stanford University, 1992.

[63] M. Vetterli and J. Kovacevic, Wavelets and Subband Coding. Prentice Hall PTR, 1995.

[64] P. R. King, "The use of renormalization for calculating effective permeability," Transport in Porous Media, vol. 4, feb 1989.

[65] D. Peaceman, "Effective Transmissibilities of a Gridblock by Upscaling - Comparison of Direct Methods with Renormalization," SPE Journal, vol. 2, pp. 338–349, sep 1997.

[66] M. Karimi-Fard, L. Durlofsky, and K. Aziz, "An Efficient Discrete-Fracture Model Applicable for General-Purpose Reservoir Simulators," SPE Journal, vol. 9, pp. 227–236, jun 2004.

[67] I. Daubechies and W. Sweldens, "Factoring wavelet transforms into lifting steps," The Journal of Fourier Analysis and Applications, vol. 4, pp. 247–269, may 1998.

[68] A. T. Gjika, Multi-Resolution Analysis for Lifting Transform on General Graphs. Master's thesis, Politecnico di Torino, 2012.

[69] D. Ron, I. Safro, and A. Brandt, "Relaxation-Based Coarsening and Multiscale Graph Organization," Multiscale Modeling & Simulation, vol. 9, pp. 407–423, jan 2011.

[70] S. K. Narang and A. Ortega, "Lifting Based Wavelet Transforms on Graphs," in APSIPA, 2009.

[71] T. Biyikoglu, J. Leydold, and P. F. Stadler, Laplacian Eigenvectors of Graphs - Perron-Frobenius and Faber-Krahn Type Theorems. Springer, 2007.

[72] R. Landauer, "The Electrical Resistance of Binary Metallic Mixtures," Journal of Applied Physics, vol. 23, p. 779, jun 1952.

[73] M. Sahimi, Heterogeneous Materials I: Linear transport and optical properties. 2003.

[74] M. Christie and M. Blunt, "Tenth SPE Comparative Solution Project: A Comparison of Upscaling Techniques," in SPE Reservoir Simulation Symposium, Society of Petroleum Engineers, apr 2013.

[75] H. Zhou, "Algebraic multiscale finite-volume methods for reservoir simulation," 2010.

[76] L. K. Fung, A. Hiebert, and L. Nghiem, "Reservoir Simulation With a Control-Volume Finite-Element Method," SPE Reservoir Engineering, vol. 7, pp. 349–357, aug 1992.

[77] S. Vakili-Ghahani and J. D. Jansen, "Control-Relevant Upscaling," SPE Journal, vol. 15, pp. 471–479, jun 2010.

[78] M. Pal, M. Edwards, and A. Lamb, "Convergence study of a family of flux continuous, finite volume schemes for the general tensor pressure equation," International journal for numerical methods in fluids, 2006.

[79] I. Aavatsmark, "An Introduction to Multipoint Flux Approximations for Quadrilateral Grids," Computational Geosciences, vol. 6, pp. 405–432, sep 2002.

[80] M. J. Zandvliet, Model-based Lifecycle Optimization of Well Locations and Production Settings in Petroleum Reservoirs. Phd dissertation, Delft University of Technology, 2008.

[81] L. W. Lake and U. Texas, "A Capacitance Model To Infer Interwell Connectivity From Production- and Injection-Rate Fluctuations," in SPE Annual Technical Conference and Exhibition, no. December, (Dallas), Society of Petroleum Engineers, 2006.

[82] D. Kaviani, J. Jensen, L. Lake, and M. Fahes, "Estimation of Interwell Connectivity in the Case of Fluctuating Bottomhole Pressures," in Proceedings of Abu Dhabi International Petroleum Exhibition and Conference, Society of Petroleum Engineers, nov 2008.